UNIVERSITY OF CALIFORNIA,
IRVINE

Aerial Vehicle Navigation with Terrestrial Signals of Opportunity: Performance Analysis and Transmitter Selection

THESIS

submitted in partial satisfaction of the requirements
for the degree of

MASTER OF SCIENCE

in Mechanical and Aerospace Engineering

by

Alexander A. Nguyen

Thesis Committee:
Professor Zaher (Zak) M. Kassas, Chair
Professor Tryphon T. Georgiou
Professor Solmaz S. Kia

2022

DEDICATION

To my parents, Anne and Andrew.

TABLE OF CONTENTS

Page

LIST OF FIGURES **v**

LIST OF TABLES **vii**

LIST OF ALGORITHMS **viii**

ACKNOWLEDGMENTS **ix**

ABSTRACT OF THE THESIS **x**

1 Introduction **1**
1.1 Background 1
1.2 Relevant Work and Contributions 2
1.3 Thesis Outline 7

2 Observability Analysis and A Lower Bound on the Error Covariance for Radio SLAM with Terrestrial SOPs **9**
2.1 Model Description 10
2.1.1 Receiver Dynamics Model 10
2.1.2 SOP Dynamics Model 11
2.1.3 Modified Clock Error States 12
2.1.4 EKF Model 13
2.2 Base Case Observability Analysis 13
2.2.1 Theoretical Background: Observability of Linear and Nonlinear Systems 14
2.2.2 Observability Analysis Results 15
2.3 Radio SLAM Performance Analysis 17
2.3.1 Motivating Scenario 17
2.3.2 Boundedness of EKF Estimation Error Covariance 18
2.3.3 Lower Bound on the EKF Estimation Error Covariance 18
2.3.4 Simulation Results 21
2.4 Experimental Results 24
2.4.1 Hardware and Software Setup 25
2.4.2 Radio SLAM Base Case Results 27

3 Efficient Transmitter Selection Strategies for Improved Information Gathering with Terrestrial SOPs **30**
3.1 Model Description and Problem Description 31
3.1.1 Overview: Aerial Vehicle Model for SOP-Based Navigation 31
3.1.2 Fisher Information Matrix 32
3.1.3 Static Estimation Framework 33
3.1.4 Problem Description 34
3.2 Terrestrial SOP Selection Framework 37
3.3 Transmitter Selection Strategy Analysis 40
3.3.1 Terrestrial SOP Selection Subset Comparison: 1–D Case 40
3.3.2 Terrestrial SOP Selection Subset Comparison: 2–D Case 44
3.3.3 Upper Bound on the Fisher Information Matrix 48
3.4 Simulation Results 49
3.4.1 Simulation Settings 49
3.4.2 Generating the Terrestrial SOP Locations 51
3.4.3 Optimal Selection, OGS, and OSS Strategy Comparison 51
3.4.4 Effect of Timing on the Optimal Transmitter Selection 55
3.4.5 Computational Cost 57
3.5 Experimental Results 58
3.5.1 Hardware and Software Setup 58
3.5.2 Flight A: Transmitter Selection in Rural Region $\binom{57}{15}$ 60
3.5.3 Flight B: Transmitter Selection in Semi-Urban Region $\binom{18}{9}$ 62

4 Conclusions **66**

Appendix A Relationship Between the Weighted HDOP Matrix and Information Content **68**

Appendix B Fisher Information Matrix Structure: Pseudorange and Range-Only Observations **70**

Appendix C Sandia National Laboratories Funding Statement **72**

Bibliography **73**

LIST OF FIGURES

Page

2.1 Uniform estimation performance as a function of unknown SOPs using the A-optimality criteria, i.e., $\text{Tr}[\mathbf{P}_{\text{LB}}]$. 23
2.2 Simulation results for 10^3 MC realizations. (a) 1σ bounds for the EKF estimation error covariance matrix compared with theoretical lower bound. (b) Minimum eigenvalue point cloud verifying $\mathbf{P}(k|k) \succeq \mathbf{P}_{\text{LB}}$. 24
2.3 Experiment hardware setup. 25
2.4 Radio SLAM base case experimental results showing the estimation error trajectories and corresponding $\pm 1\sigma$ bounds. 28
2.5 (a) Experiment layout containing the true locations of each SOP tower and the two UAV navigation solutions. (b) UAV trajectory comparison between the RTK-IMU navigation solution (red) and radio SLAM (blue). (c) Initial and final position estimates with their associated north-east uncertainty ellipse for SOP tower 3. Map data: Google Earth. 29

3.1 Problem description. An aerial vehicle is navigating in an unknown environment by exploiting the available GNSS signals. During its flight, the aerial vehicle experiences a GNSS outage (e.g., spoofing or jamming) which causes the available GNSS signals to become unreliable. Luckily, a nearby uplink station is able to send SOP map data to the aerial vehicle containing an exhaustive list of the available cellular tower locations in the area. 35
3.2 Motivating scenario. Terrestrial SOP towers (white) in the environment with respect to the aerial vehicle's selection point (black cross). Using all 57 SOP towers to navigate the aerial vehicle would violate SWaP-C constraints. As such, it is desired to choose the "best" subset of SOPs to use to navigate the aerial vehicle. 36
3.3 A receiver estimating one of its states in an environment comprised of M terrestrial SOPs. 40
3.4 A receiver estimating its two position states in an environment comprised of M terrestrial SOPs. 44
3.5 (a) BPP realization with $M = 30$ SOPs. (b) Parameterization of the i^{th} SOP's position. 51
3.6 Selection strategy comparison. (a) M choose K. (b) Opportunistic greedy selection. (c) One shot selection. 53

3.7 Cost function point cloud with 10^3 MC realizations for the optimal selection (green), opportunistic greedy selection (red), and one shot selection (blue) strategies. The averaged cost function value over all MC realizations is represented as a large dot, whereas each selection strategy's cost function value for each MC realization is represented as a small dot. 54
3.8 Optimal transmitter selection's performance using the A-optimality criterion averaged over 250 MC realizations. Comparison between psuedorange observations, i.e., considering timing, (black) and range-only observations, neglecting timing, (red). 56
3.9 Each selection strategy's time to run. (a) M choose K. (b) OGS. (c) OSS. . 57
3.10 Hardware setup equipped to the C-12 aircraft. 59
3.11 Experimental layout and results using the OGS and OSS strategies for transmitter selection during the aircraft's flight. Map data: Google Earth. 61
3.12 Histogram pdf of the position and velocity RMSEs for 10^5 different randomized transmitter selections versus the OGS strategy's RMSEs (red) versus the OSS strategy's RMSEs (green). 62
3.13 Experimental layout and results using the optimal selection, OGS, and OSS strategies for transmitter selection during the aircraft's flight. Map Data: Google Earth. 64

LIST OF TABLES

Page

2.1 Radio SLAM Simulation Settings for the Receiver and each SOP 22
2.2 eNodeBs' characteristics 26

3.1 Transmitter Selection Environment Simulation Settings 50
3.2 Performance Metric Comparison for Selection strategies 52
3.3 Transmitter Selection Strategy's Average Cost Function Values for $K = 6 - 10$ 55
3.4 Transmitter Selection Strategy's Average Cost Function Values for $K = 11 - 14$ 55
3.5 Experiment 1: Navigation Solution Performance 62
3.6 Experiment 1: Navigation Solution Performance 62
3.7 Experiment 2: Navigation Solution Performance 64
3.8 Experiment 2: Navigation Solution Performance 65

LIST OF ALGORITHMS

		Page
1	Transmitter Selection Strategies	39

ACKNOWLEDGMENTS

I would like to thank my advisor, Prof. Zak Kassas, for all his time, guidance, and support over the past two years. I am especially grateful for all our discussions pertaining to research and sports. Under his advisorship, I was able to develop as a researcher and mature as an individual.

I would like to thank my Master's committee members, Prof. Tryphon Georgiou and Prof. Solmaz Kia, for taking time out of their busy schedules to serve in the committee.

I appreciate the generous funding from the Office of Naval Research (ONR), the National Science Foundation (NSF), and the Sandia National Laboratories for supporting my research. Specifically, I am very grateful to Mr. Tucker Haydon and Dr. Anh Luong for their helpful discussions and insight related to my research after each quarterly update with Sandia National Laboratories.

I am extremely grateful to my friends at the ASPIN Lab; Nadim Khairallah and Mu Jia for our always exhilarating tennis matches and all our lively conversations related to research, coursework, or life; Mohammad Neinavaie and Ali Abdallah for their helpful discussions; Mohamad Orabi, Jamil Haidar-Ahmad, Sharbel Kozhaya, and Ralph Sabbagh for their friendships. I am also very appreciative to Dr. Joe Khalife and Dr. Zeinab Shadram for their advice and suggestions which helped me to improve my research.

I would also like to express my appreciation to my friends and family members who helped to shape me into the person I am today. Especially, I would like to give a very heartfelt thanks to my girlfriend, Helene Levy, for her encouragement to do my best, unwavering support during difficult times, and helping me to become a better person.

Finally, I would like to thank parents, Anne McDonald and Andrew Nguyen, for their unconditional love and support throughout my life. No matter how busy they were, they always found time in the day to enable me to attend academic events and pursue my extracurricular hobbies. Their wholehearted support is what motivates me to do my best every day. I am beyond grateful to have them both in my life, and none of my success would have been possible without both of them.

ABSTRACT OF THE THESIS

Aerial Vehicle Navigation with Terrestrial Signals of Opportunity:
Performance Analysis and Transmitter Selection

By

Alexander A. Nguyen

Master of Science in Mechanical and Aerospace Engineering

University of California, Irvine, 2022

Professor Zaher (Zak) M. Kassas, Chair

The performance analysis and transmitter selection for an aerial vehicle navigating with terrestrial signals of opportunity (SOPs) is studied. The following problem is considered. An aerial vehicle is navigating in an environment where global navigation satellite system (GNSS) signals are unavailable. The aerial vehicle is assumed to be equipped with an onboard receiver capable of extracting psuedorange observations from an abundant number of terrestrial SOP towers. Each SOP tower contains dynamic, stochastic clock error states (bias and drift) which are estimated as the difference between the receiver's and each SOP's clock bias and clock drift terms. A dynamic estimator (e.g., an extended Kalman filter (EKF)) is employed to fuse the psuedorange observations to simultaneously localize the aerial vehicle and SOP towers. A lower bound on the error covariance of radio simultaneous localization and mapping (SLAM) with terrestrial SOPs is derived. In addition, it is shown that the so-called radio SLAM base case is observable, in which an aerial vehicle with imperfect knowledge about its initial states is navigating in an environment containing one unknown SOP tower and two partially known SOP towers (i.e., towers whose position are known, but clock error states are unknown). Furthermore, the computationally efficient transmitter selection strategies, termed opportunistic greedy selection (OGS) and one shot selection (OSS), for selecting the most informative terrestrial SOPs subset is developed. These transmitter selec-

tion strategies will exploit the additive, iterative properties of the Fisher Information Matrix (FIM) to minimize the aerial vehicle's average position error variance (i.e., A-optimality criterion). Simulation results demonstrate the derived lower bound on the error covariance numerically via Monte Carlo (MC) runs and analyzes the performance of different transmitter selection strategies. Experimental results are presented in two different scenarios: (i) unmanned aerial vehicle (UAV) with an initial estimate of its position making pseudorange observations on two partially known and one unknown cellular SOP, and (ii) U.S. Air Force high altitude aircraft navigating with pseudorange observations from terrestrial SOPs in a rural environment tasked with selecting $K = 15$ out of $M = 57$ total SOPs and in a semi-urban environment tasked with selecting $K = 9$ out of $M = 18$ total SOPs.

Chapter 1

Introduction

1.1 Background

Many modern aerial vehicle navigation systems, whether low altitude unmanned aerial vehicles (UAVs) or high altitude aircraft, rely heavily on global navigation satellite system (GNSS) signals [1, 2]. However, relying on GNSS alone does not yield a continuous flow of resilient and precise aerial vehicle position, speed, and time estimates [3]. In recent years, GNSS radio frequency interference (RFI) events have increased dramatically, threatening the safety of flight operations [4] and calling for a reliable alternative to GNSS signals in the event that these signals become unusable [5]. GNSS-challenged environments, e.g., those experiencing spoofing [6] or jamming [7], require an alternative to GNSS for safe and reliable navigation. These alternative approaches can include the use of sensors with complementary sensing modalities (e.g., lasers [8], ultrasonic [9], cameras [10], and inertial measurement units [11]).

Another approach is radio navigation-based, which utilize signals of opportunity (SOPs) [12, 13, 14] whenever GNSS signals become unusable [15]. SOPs can be terrestrial-based

(e.g., AM/FM radio [16, 17], cellular [18, 19, 20, 21, 22, 23, 24, 25, 26, 27, 28, 29, 30, 31, 32, 33, 34, 35, 36], and digital television [37, 38, 39],) or space-based (e.g., low Earth orbit (LEO) satellites [40, 41, 42, 43, 44, 45, 46, 47, 48, 49, 50]). These signals were not intended for navigation purposes, but the literature has shown that they can be exploited for such purposes. SOPs are abundant, transmitted in a wide range of frequencies, more powerful than GNSS signals, and geometrically diverse. These inherent attributes of SOPs compensate for the limitations of GNSS signals. Among the different SOP types, cellular signals have shown tremendous promise, with meter-level accurate navigation demonstrated on ground and aerial vehicles [51, 52, 53, 54, 55, 56, 57, 58, 59, 60, 61, 62, 63, 64, 65, 66]. However, unlike the states of a GNSS space vehicle, SOP states are typically unknown during navigation which requires them to be estimated on the fly [67]. This is similar to the simultaneous localization and navigation (SLAM) estimation problem in robotics [68]. In traditional SLAM, an agent constructs a map of the environment while simultaneously localizing itself within this map. Typically, an environment is composed of static landmarks, e.g., walls, posts, and corners. However, unlike traditional SLAM, SOPs are mapped as spatio-temporal landmarks composed of dynamic, stochastic states (i.e., clock error terms). The problem of simultaneously mapping ambient SOPs while localizing an aerial vehicle-mounted receiver using PNT information is referred to as radio SLAM [69, 70].

1.2 Relevant Work and Contributions

This thesis considers the performance analysis and transmitter selection for an aerial vehicle navigating with terrestrial SOPs. Specifically, pertaining to the following problem. An aerial vehicle is flying in an environment where GNSS signals are unavailable. The environment contains an abundant number of M terrestrial SOPs with known locations (e.g., from satellite images, databases, or radio mapping [71]) but unknown dynamic, stochastic clock error

states (bias and drift). The aerial vehicle is assumed to be equipped with an onboard receiver capable of extracting pseudorange observations from the ambient SOPs' signals. An extended Kalman filter (EKF) is then employed to fuse these pseudorange observations to estimate the aerial vehicle's states (position and velocity) and the difference between the aerial vehicle-mounted receiver's and all terrestrial SOP's clock bias and clock drift states, respectively.

Assessing terrestrial SOPs on aerial vehicles, both low altitude unmanned aerial vehicles (UAVs) and high altitude aircrafts, has been considered in the context of channel modeling, communication, and navigation [72, 73, 74, 75, 76, 77, 78, 79]. Of particular note is the recent study that demonstrated the tremendous potential of cellular SOPs for high altitude aircraft navigation, showing that terrestrial cellular SOPs can be acquired and tracked at altitudes reaching 23,000 feet above ground level and at horizontal distances of nearly 100 kilometers and could yield meter-level accurate navigation solutions without GNSS [80, 81]. In fact, at high altitudes, it was also discovered that dozens of terrestrial SOPs are hearable. Tracking all such SOPs simultaneously could be formidable on platforms with limited size, weight, power, and cost (SWaP-C) or unnecessary, since tracking a subset of the SOPs could yield a comparable performance. Therefore, the transmitter selection (or more broadly, sensor selection) problem is posed to mitigate the receiver's computational strain from the overwhelming number of ambient signals. The aerial vehicle is tasked to select a subset of the K available terrestrial SOPs to use for navigation. In addition, the problem of determining the minimum number of terrestrial SOPs needed for aerial vehicle navigation while performing radio SLAM and finding a lower bound on the error covariance associated with an aerial vehicle navigating in an unknown, or a partially known, SOP environment is posed as well.

These problems have been built upon the answers to fundamental questions discussed in the literature; such as deterministic linearized and nonlinear observability of collaborative opportunistic navigation [82, 83], stochastic observability of radio SLAM [84], radio SLAM

filter boundedness [30], radio SLAM performance [85], motion planning in radio SLAM environments [86, 87], and communication and information fusion strategies for collaborative radio SLAM [88, 89, 90, 91]. Nevertheless, lower bounds for the radio SLAM problem have not been established yet. These bounds are of considerable importance as they establish the bounds on the achievable performance in an unknown or a partially known SOP environment. Previous work has derived expressions for calculating uniform bounds of the estimation error covariance by ensuring uniform controllability and uniform observability are satisfied simultaneously [92]. Furthermore, other work established performance bounds for the traditional SLAM problem [93, 94, 95, 96, 97, 98]. However, these bounds do not apply to the problem considered in this thesis, since radio SLAM utilizes a different observation model and the state space contains dynamic, stochastic landmark states.

Similar problems have been studied from the context of sensor and satellite selection which are crucial in many applications such as source localization, tracking, and navigation [99, 100, 101]. The sensor selection problem can be cast as a convex optimization problem [102, 103, 104] or piece-wise convex optimization problem [71, 105], which propose methods to select the optimal sensors with respect to a specific criterion. Although, sometimes it is difficult to formulate the sensor selection problem as a convex problem so non-convex formulations have been developed instead [106, 107, 108]. Alternatively, this problem has been considered as a greedy sensor selection leveraging the notion of submodularity [109, 110, 111], as well as methods utilizing the Fisher information matrix (FIM) which is related to the Cramér-Rao Lower Bound (CRLB) [112, 113, 114, 115]. It is important to point out that, typically, the sensor selection problem discussed in the literature assumes vehicle navigation using linear measurements for sensor fusion occurring over limited regions (on the order of one to several hundred meters) whereas this work focuses on vehicle navigation using nonlinear measurements for signal fusion over a large region (on the order of one to several kilometers). Alternatively, the satellite selection problem typically formulates optimal GNSS satellite selection algorithms focused on the geometric dilution of precision (GDOP) metric

[116, 117, 118, 119, 120]. These algorithms were developed to select the satellites with the most favorable spatial distribution via optimizing the GDOP metric, whereas this thesis aims to maximize the information content (which, in turn, minimizes the estimation error uncertainty) from SOP pseudoranges by utilizing the FIM.

The contributions of this thesis are as follows. First, the thesis demonstrates observability for the so-called radio SLAM base case, in which an aerial vehicle with imperfect knowledge about its initial states is navigating in an environment containing one unknwown SOP tower and two partially known SOP towers (i.e., towers whose positions are known, but clock error states are unknown) and derives a lower bound for the estimation error covariance of an extended Kalman filter (EKF)-based radio SLAM framework. Second, the thesis develops sub-optimal, yet computationally efficient, transmitter selection strategies termed opportunistic greedy selection (OGS) and one shot selection (OSS) for selecting the most informative transmitter subset by exploiting the additive, iterative properties of the FIM instead of explicitly solving the rather involved optimal transmitter selection problem. The OGS algorithm selects the most informative transmitters in multiple iterations (i.e., recursive selection), whereas the OSS algorithm selects the most informative transmitters in one iteration (i.e., batch selection), to minimize the aerial vehicle's average position error variance (i.e., A-optimality criterion). Third, this thesis provides an analysis of the developed transmitter selection strategies via a selection subset comparison (1–D and 2–D) and an upper bound on the FIM (or, lower bound on the estimation error covariance) for the selected SOP observations.

The contributions are demonstrated in both simulation and experiment for a variety of scenarios. Numerical simulations are presented for the lower bound on the aerial vehicle's error covariance while navigating via Monte Carlo (MC) runs, as well as a performance analysis on the different transmitter selection strategies. Furthermore, the computational cost (i.e., run-time) of the different transmitter selection strategies is shown to illustrate the

efficiency of the OGS and OSS strategies versus the optimal selection strategy. Furthermore, experimental results are presented for two different scenarios with real data: (i) UAV with an initial estimate of its position making pseudorange observations to two partially known and one unknown cellular SOPs while performing radio SLAM without GNSS signals and (ii) U.S. Air Force high altitude aircraft navigating without GNSS signals in a rural environment comprised of $M = 57$ total cellular SOPs tasked with selecting $K = 15$ cellular SOPs and in a semi-urban environment comprised of $M = 18$ total cellular SOPs tasked with selecting $K = 9$ cellular SOPs. It is important to note, the observability analysis remains valid for the radio SLAM base case such that a navigation solution can be obtained for (i) and each transmitter selection strategy was found to be valid for several kilometers of the aerial vehicle's flight trajectory since the aerial vehicle-to-SOP geometry is approximately stationary for sufficiently faraway SOP towers for (ii).

The contributions in this thesis have resulted in the referreed conference publications: [C1] and [C2], and a journal publication [J1] (in preparation), which are highlighted below.

[C1] Nguyen, Z. Shadram, and Z. Kassas. (2021, September). A lower bound for the error covariance of radio SLAM with terrestrial signals of opportunity. *In Proceedings of ION Global Navigation Satellite Systems Conference*, pp. 2294–2306.

[C2] A. Nguyen and Z. Kassas. (2022, January). Transmitter selection for improved information gathering in aerial vehicle navigation with terrestrial signals of opportunity. *In Proceedings of ION International Technical Meeting*, pp. 723–734.

[J1] A. Nguyen and Z. Kassas. (2022). Efficient Transmitter Selection Strategies for Improved Information Gathering of Aerial Vehicle Navigation in GNSS-Denied Environments. *IEEE Aerospace and Electronic Systems Magazine*. (In preparation)

1.3 Thesis Outline

The thesis is organized by contributions, which are as follows:

Chapter 2: Observability Analysis and A Lower Bound on the Error Covariance for Radio SLAM with Terrestrial SOPs

This chapter provides an observability analysis and derives a lower bound for the error covariance of the radio simultaneous localization and mapping (SLAM) framework with terrestrial signals of opportunity (SOPs) using pseudorange observations from cellular SOPs for navigation. First, the receiver and SOP dynamics model, modified clock error states, and the EKF model adopted for this chapter are provided. Next, an observability analysis pertaining to the radio SLAM base case (i.e., UAV with imperfect knowledge of its initial states using signals from two partially known cellular SOPs and an unknown cellular SOP) is performed. Then, a lower bound for the radio SLAM problem is derived as a function of time and number of partially known and unknown SOPs, which is subsequently demonstrated numerically with simulation results. Finally, experimental results conducted on a UAV performing radio SLAM without GNSS signals is provided.

Chapter 3: Efficient Transmitter Selection Strategies for Improved Information Gathering with Terrestrial SOPs

This chapter develops computationally efficient, yet sub-optimal, transmitter selection strategies for choosing the most informative subset of terrestrial signals of opportunity (SOPs) and provides a performance analysis on the proposed selection strategies. First, the models employed in this chapter and a problem description is provided. Subsequently, followed by the terrestrial SOP selection framework. Next, an analysis comparing each transmitter selection strategy's selection subset for the 1–D and 2–D FIM cases is performed and an upper bound on the FIM for the selected SOP observations is derived. Then, numerical results are shown for comparing the performance of the different transmitter selection strategies, the effect of

considering timing (pseudorange observations) versus neglecting timing (range-only observations) using the optimal selection strategy, and computational cost of each transmitter selection strategy. Finally, experimental results for a U.S. Air Force high altitude aircraft using the proposed selection frameworks over a valid selection region in a rural environment and a semi-urban environment is provided.

Chapter 4: Conclusions

This chapter summarizes the contributions of this thesis.

Chapter 2

Observability Analysis and A Lower Bound on the Error Covariance for Radio SLAM with Terrestrial SOPs

This chapter is organized as follows. Section 2.1 describes the receiver and SOP dynamics models, modified clock error states, and the EKF model. Section 2.2 contains a brief observability analysis pertaining to the radio SLAM base case (i.e., UAV with imperfect knowledge of its initial states using signals from two partially known cellular SOPs and an unknown cellular SOP). Section 2.3 derives a lower bound for the radio SLAM problem as a function of time and number of partially known and unknown SOPs, which is subsequently demonstrated with simulation results. Section 2.4 presents experimental results conducted on a UAV performing radio SLAM without GNSS signals.

2.1 Model Description

This section presents the dynamics model for a UAV-mounted receiver and a terrestrial SOP tower, the modified clock error states, and the EKF model. Only the UAV's two-dimensional (2–D) position is considered, as an altimeter or barometric pressure sensor can be used to estimate the UAV's altitude.

2.1.1 Receiver Dynamics Model

The UAV-mounted receiver states consist of the 2-D positions $\boldsymbol{r}_r = [x_r,\ y_r]^{\mathsf{T}}$, 2-D velocities $\dot{\boldsymbol{r}}_r = [\dot{x}_r,\ \dot{y}_r]^{\mathsf{T}}$, and clock error states $\boldsymbol{x}_{\text{clk},r} = [c\delta t_r,\ c\dot{\delta t}_r]^{\mathsf{T}}$ where $\delta t_r(k)$ and $\dot{\delta t}_r(k)$ are the receiver's clock bias and drift, respectively, and c is the speed of light. The receiver's position and velocity states are assumed to adhere to a velocity random walk model [121]. Therefore, the UAV-mounted receiver can be modeled as the following discrete-time model

$$\boldsymbol{x}_{\text{r}}\left(k+1\right) = \mathbf{F}_r\, \boldsymbol{x}_{\text{r}}(k) + \boldsymbol{w}_r(k), \quad k = 0, 1, 2, ...,$$

where

$$\boldsymbol{x}_{\text{r}} = [\boldsymbol{r}_r^{\mathsf{T}},\ \dot{\boldsymbol{r}}_r^{\mathsf{T}},\ \boldsymbol{x}_{\text{clk},r}^{\mathsf{T}}]^{\mathsf{T}},$$

$$\mathbf{F}_r = \begin{bmatrix} \mathbf{I}_{2\times 2} & T\mathbf{I}_{2\times 2} & \mathbf{0}_{2\times 2} \\ \mathbf{0}_{2\times 2} & \mathbf{I}_{2\times 2} & \mathbf{0}_{2\times 2} \\ \mathbf{0}_{2\times 2} & \mathbf{0}_{2\times 2} & \mathbf{F}_{\text{clk}} \end{bmatrix}, \quad \mathbf{F}_{\text{clk}} = \begin{bmatrix} 1 & T \\ 0 & 1 \end{bmatrix},$$

where $\boldsymbol{w}_{\mathrm{r}}$ is the receiver's process noise, which is modeled as a discrete-time zero-mean white noise sequence with covariance $\mathbf{Q}_r = \mathrm{diag}[\mathbf{Q}_{\mathrm{pv}},\ \mathbf{Q}_{\mathrm{clk},r}]$, with

$$\mathbf{Q}_{\mathrm{pv}} = \begin{bmatrix} \tilde{q}_x \frac{T^3}{3} & 0 & \tilde{q}_x \frac{T^2}{2} & 0 \\ 0 & \tilde{q}_y \frac{T^3}{3} & 0 & \tilde{q}_y \frac{T^2}{2} \\ \tilde{q}_x \frac{T^2}{2} & 0 & \tilde{q}_x T & 0 \\ 0 & \tilde{q}_y \frac{T^2}{2} & 0 & \tilde{q}_y T \end{bmatrix}, \quad \mathbf{Q}_{\mathrm{clk},r} = c^2 \begin{bmatrix} S_{\tilde{w}_{\delta t_r}} T + S_{\tilde{w}_{\dot{\delta t}_r}} \frac{T^3}{3} & S_{\tilde{w}_{\dot{\delta t}_r}} \frac{T^2}{2} \\ S_{\tilde{w}_{\dot{\delta t}_r}} \frac{T^2}{2} & S_{\tilde{w}_{\dot{\delta t}_r}} T \end{bmatrix},$$

where T is the sampling time and $\tilde{q}_x$ and $\tilde{q}_y$ are the continuous-time x and y acceleration noise power spectral densities. The terms $S_{\tilde{w}_{\delta t_r}}$ and $S_{\tilde{w}_{\dot{\delta t}_r}}$ are the clock bias and drift process noise power spectra, which can be related to the power-law coefficients, $\left\{h_{\alpha,s_i}\right\}_{\alpha=-2}^{2}$. Laboratory experiments have shown that the power spectral density of the fractional frequency deviation of an oscillator from nominal frequency to be appropriately approximated by $S_{\tilde{w}_{\delta t_r}} \approx \frac{h_{0,r}}{2}$ and $S_{\tilde{w}_{\dot{\delta t}_r}} \approx 2\pi^2 h_{-2,r}$ [122].

2.1.2 SOP Dynamics Model

Each SOP is assumed to emanate from a spatially-stationary terrestrial transmitter. The states will consist of 2-D positions $\boldsymbol{r}_{s_i} = [x_{s_i},\ y_{s_i}]^{\mathsf{T}}$ and clock error states $\boldsymbol{x}_{\mathrm{clk},s_i} = [c\delta t_{s_i},\ c\dot{\delta t}_{s_i}]^{\mathsf{T}}$, where $\delta t_{s_i}(k)$ and $\dot{\delta t}_{s_i}(k)$ are the i^{th} SOP's clock bias and drift, respectively, with $i = 1, \ldots, M$, where $M \triangleq n + m$ is the total number of SOPs in the environment with n being the number of partially known SOPs and m being the number of unknown SOPs. The i^{th} terrestrial SOP's discretized state-space model can be described by

$$\boldsymbol{x}_{s_i}(k+1) = \mathbf{F}_s\, \boldsymbol{x}_{s_i}(k) + \boldsymbol{w}_{s_i}(k), \quad k = 0, 1, 2, ...,$$

where

$$\boldsymbol{x}_{s_i} = [\boldsymbol{r}_{s_i}^{\mathsf{T}},\ \boldsymbol{x}_{\text{clk},s_i}^{\mathsf{T}}]^{\mathsf{T}},$$
$$\mathbf{F}_s = \text{diag}[\mathbf{I}_{2\times 2}, \mathbf{F}_{\text{clk}}],$$

where $\boldsymbol{w}_{s_i}$ is the i^{th} terrestrial SOP's process noise, modeled as a discrete-time zero-mean white noise sequence with covariance $\mathbf{Q}_{s_i} = \text{diag}[\mathbf{0}_{2\times 2},\ \mathbf{Q}_{\text{clk},s_i}]$. The $\mathbf{Q}_{\text{clk},s_i}$ covariance matrix is identical to $\mathbf{Q}_{\text{clk},r}$, except that $S_{\tilde{w}_{\delta t_r}}$ and $S_{\tilde{w}_{\dot{\delta} t_r}}$ are replaced with SOP-specific spectra $S_{\tilde{w}_{\delta t,s,i}}$ and $S_{\tilde{w}_{\dot{\delta} t,s,i}}$. These spectra terms are modeled similarly to the receiver spectra but with SOP-specific values h_{0,s_i} and h_{-2,s_i}.

2.1.3 Modified Clock Error States

Estimating the individual clock error terms for the receiver and each respective SOP could yield a stochastically unobservable system with diverging estimation error variances [84]. Thus, the modified clock bias and clock drift states are redefined to be the difference between the receiver's and SOPs' clock error terms, according to

$$c\delta t_i \triangleq c\delta t_r - c\delta t_{s_i}, \quad i = 1, \ldots, M.$$
$$c\dot{\delta} t_i \triangleq c\dot{\delta} t_r - c\dot{\delta} t_{s_i}.$$

Now, the clock states are given as $\boldsymbol{x}_{\text{clk},i} \triangleq \left[c\delta t_i,\ c\dot{\delta} t_i\right]^{\mathsf{T}}$, where the SOP state vector is redefined as $\boldsymbol{x}_{s_i} = \left[\boldsymbol{r}_{s_i}^{\mathsf{T}},\ \boldsymbol{x}_{\text{clk},i}^{\mathsf{T}}\right]^{\mathsf{T}}$. The new clock dynamics are given by

$$\boldsymbol{x}_{\text{clk},i}(k+1) = \mathbf{F}_{\text{clk}}\boldsymbol{x}_{\text{clk},i}(k) + \boldsymbol{w}_{\text{clk},i}(k), \quad k = 0, 1, 2, \ldots,$$

where $\boldsymbol{w}_{\text{clk},i}$ is the modified clock error state's process noise, which is modeled as a discrete-time zero-mean white noise sequence with covariance $\mathbf{Q}_{\text{clk},i} = \mathbf{Q}_{\text{clk},r} + \mathbf{Q}_{\text{clk},s_i}$.

2.1.4 EKF Model

The EKF estimates the UAV-mounted receiver's position and velocity, n SOP tower's modified clock error states, and m SOP tower's position and modified clock error states, namely

$$\boldsymbol{x} \triangleq [\boldsymbol{r}_r^{\mathsf{T}},\ \dot{\boldsymbol{r}}_r^{\mathsf{T}},\ \boldsymbol{x}_{\text{clk},1}^{\mathsf{T}}, \ldots, \boldsymbol{x}_{\text{clk},n}^{\mathsf{T}},\ \boldsymbol{x}_{s_{n+1}}^{\mathsf{T}}, \ldots,\ \boldsymbol{x}_{s_M}^{\mathsf{T}}]^{\mathsf{T}}.$$

Note that $\boldsymbol{x}$ may be expressed as $\boldsymbol{x} = \mathbf{T}\boldsymbol{x}'$, where $\boldsymbol{x}'$ is the non-modified EKF state vector and $\mathbf{T}$ is some permutation matrix which can be readily calculated for state transformation. The pseudorange observations made by the receiver on the i^{th} SOP tower is related to the receiver's and SOPs' states by

$$z_{s_i}(k) = \underbrace{\left\|\boldsymbol{r}_r(k) - \boldsymbol{r}_{s_i}\right\|_2 + c\delta t_i(k)}_{h_i[\boldsymbol{x}(k)]} + v_{s_i}(k), \quad i = 1, \ldots, M, \tag{2.1}$$

where $\|\cdot\|_2$ is the Euclidean norm and v_{s_i} is the measurement noise, which is modeled as a zero-mean white Gaussian sequence with variance $\sigma_{s_i}^2$. It is assumed that the measurement noise is uncorrelated across the different SOPs.

2.2 Base Case Observability Analysis

This section shows that the radio SLAM base case, defined as a UAV with imperfect knowledge of its initial states in an environment with $n = 2$ partially known (mapped) and $m = 1$ unknown SOP towers, to guarantee observability. Moreover, this analysis shows the minimum number of SOP towers needed to guarantee observability in an arbitrary environment. This is achieved by studying the rank of the l-step observability matrix. The following assumptions are necessary to ensure the l-step observability matrix does not lose rank due to receiver trajectory or singular geometry.

A1. The terrestrial SOPs are not colocated

A2. The receiver is not stationary and does not move along a trajectory collinear to any terrestrial SOP line-of-sight vectors.

A3. The receiver's distance to each SOP is bounded at all time, i.e., $d_{\min} < \|\boldsymbol{r}_r(k) - \boldsymbol{r}_{s_i}\|_2 < d_{\max}$, $\forall\ k > 0$, and $\forall\ i = 1, \cdots, M$, where $d_{\min}$ is the minimum distance to the SOP (to ensure the UAV does not "exactly" fly over the SOP) and $d_{\max}$ is the maximum distance to the SOP (to ensure the UAV does not fly very far from the SOPs, making their geometry in the "far-field," which appears as if they are collocated).

2.2.1 Theoretical Background: Observability of Linear and Nonlinear Systems

Consider the discrete-time linear time-varying (LTV) system

$$\begin{aligned} \boldsymbol{x}(k+1) &= \mathbf{F}(k)\boldsymbol{x}(k) + \boldsymbol{\Gamma}(k)\boldsymbol{u}(k) \\ \boldsymbol{y}(k) &= \mathbf{H}(k)\boldsymbol{x}(k) \end{aligned} \tag{2.2}$$

where $\boldsymbol{x} \in \mathbb{R}^{\mathrm{n_x}}$ is the system's state vector, $\boldsymbol{u} \in \mathbb{R}^{\mathrm{n_u}}$ is the system's input vector, and $\boldsymbol{y} \in \mathbb{R}^{\mathrm{n_y}}$ is the system's measurement vector. The observability of a LTV system is typically determined by studying the rank of the observability Grammian or the observability matrix. The following theorem states a necessary and sufficient condition for LTV observability through the l-step observability matrix [123].

THEOREM III.1: The discrete-time LTV system is l-step observable if and only if the l-step

observability matrix, defined as

$$\boldsymbol{\mathcal{O}}(k, k+l) \triangleq \begin{bmatrix} \mathbf{H}(k) \\ \mathbf{H}(k+1)\boldsymbol{\Phi}(k+1,k) \\ \mathbf{H}(k+2)\boldsymbol{\Phi}(k+2,k) \\ \vdots \\ \mathbf{H}(k+l-1)\boldsymbol{\Phi}(k+l-1,k) \end{bmatrix} \tag{2.3}$$

is full rank, i.e., $\text{rank}\big[\boldsymbol{\mathcal{O}}(k, k+l)\big] = \text{n}_\text{x}$. The matrix function $\boldsymbol{\Phi}(k, j)$ is the discrete-time transition matrix, which is defined as

$$\boldsymbol{\Phi}(k, j) \triangleq \begin{cases} \mathbf{F}(k-1)\mathbf{F}(k-2)\cdots\mathbf{F}(j), & k \geq j+1 \\ \mathbf{I}, & k = j \end{cases}$$

This observability analysis can be extended to nonlinear systems by linearizing the state transition and observation models to obtain $\mathbf{F}(\text{k})$, $\boldsymbol{\Gamma}(\text{k})$, and $\mathbf{H}(\text{k})$, which establishes observability results only valid locally. More generally, a nonlinear system may be characterized as observable, locally observable, weakly observable, or locally weakly observable [124].

2.2.2 Observability Analysis Results

This analysis looks to classify observability for a discrete-time LTV system by studying the rank of the l-step observability matrix. The state vector and dynamics matrix for the base case is defined as

$$\boldsymbol{x} \triangleq [\boldsymbol{r}_r^\mathsf{T},\ \dot{\boldsymbol{r}}_r^\mathsf{T},\ \boldsymbol{x}_{\text{clk},1}^\mathsf{T},\ \boldsymbol{x}_{\text{clk},2}^\mathsf{T},\ \boldsymbol{x}_{s_3}^\mathsf{T}]^\mathsf{T}, \tag{2.4}$$

$$\mathbf{F} = \begin{bmatrix} \mathbf{I}_{2\times2} & T\mathbf{I}_{2\times2} & \mathbf{0}_{2\times2} & \mathbf{0}_{2\times2} & \mathbf{0}_{2\times4} \\ \mathbf{0}_{2\times2} & \mathbf{I}_{2\times2} & \mathbf{0}_{2\times2} & \mathbf{0}_{2\times2} & \mathbf{0}_{2\times4} \\ \mathbf{0}_{2\times2} & \mathbf{0}_{2\times2} & \mathbf{F}_{\text{clk}} & \mathbf{0}_{2\times2} & \mathbf{0}_{2\times4} \\ \mathbf{0}_{2\times2} & \mathbf{0}_{2\times2} & \mathbf{0}_{2\times2} & \mathbf{F}_{\text{clk}} & \mathbf{0}_{2\times4} \\ \mathbf{0}_{4\times2} & \mathbf{0}_{4\times2} & \mathbf{0}_{4\times2} & \mathbf{0}_{4\times2} & \mathbf{F}_{s_3} \end{bmatrix}. \tag{2.5}$$

The linearized measurement model yields the following observation Jacobian matrix

$$\begin{aligned} \boldsymbol{\xi}_i(k) &\triangleq \frac{\boldsymbol{r}_r(k) - \boldsymbol{r}_{s_i}}{\|\boldsymbol{r}_r(k) - \boldsymbol{r}_{s_i}\|_2}, \quad \forall i = 1,2,3 \\ \mathbf{H}_{r_i}(k) &= [\boldsymbol{\xi}_i^{\mathsf{T}}(k),\ \mathbf{0}_{1\times2}],\ \mathbf{H}_{s_i}(k) = [-\boldsymbol{\xi}_i^{\mathsf{T}}(k),\ \boldsymbol{h}_{\text{clk}}]^{\mathsf{T}},\ \boldsymbol{h}_{\text{clk}} = [1,\ 0], \\ \mathbf{H}(k) &= \begin{bmatrix} \mathbf{H}_{r_1}(k) & \boldsymbol{h}_{\text{clk}} & \mathbf{0}_{1\times2} & \mathbf{0}_{1\times4} \\ \mathbf{H}_{r_2}(k) & \mathbf{0}_{1\times2} & \boldsymbol{h}_{\text{clk}} & \mathbf{0}_{1\times4} \\ \mathbf{H}_{r_3}(k) & \mathbf{0}_{1\times2} & \mathbf{0}_{1\times2} & \mathbf{H}_{s_3}(k) \end{bmatrix}. \end{aligned} \tag{2.6}$$

The l-step observability matrix $\boldsymbol{\mathcal{O}}(k, k+l)$ is of dimension $l \cdot (n+m) \times 4 + 2n + 4m$. One necessary condition for the observability matrix to be full rank is that $l \cdot (n+m) \geq 4+2n+4m$, i.e., the UAV makes observations at l epochs to the M terrestrial SOP towers. Symbolic computations done in software found the l-step observability matrix to achieve full rank when $l \geq 4$ for the radio SLAM base case. Further generalized, a given system will always be l-step observable with $n \geq 2$ and $m \geq 1$ for $l \geq 4$. Note, this result is the same as the l-step criteria found in the observability analysis for a UAV performing opportunistic navigation [30]. The results of this study are valid only locally and deterministically, i.e., no process or measurement noise and no initial uncertainty. However, these result can be extended to stochastic systems by introducing noise to the position unit vectors $\boldsymbol{\xi}_i'(k) = \boldsymbol{\xi}_i(k) + \boldsymbol{w}_{\xi_i}(k)$. By invoking the stated assumptions A1 - A3, the addition of process noise will not change the structure nor the rank of $\mathbf{H}(k)$. Thus, the deterministic observability analysis still holds for a system with noise [125].

2.3 Radio SLAM Performance Analysis

This section derives a lower bound for the radio SLAM performance as a function of time and partially known and unknown SOP towers in the environment. The m unknown SOPs means that one has no knowledge of the location or clock error states. The n partially known SOPs means that one has knowledge of the location but the clock error states are unknown. The radio SLAM performance bound yields a lower bound on the uncertainty with which a UAV can localize itself and map the environment while estimating the clock error terms over a finite-time horizon. The following assumptions are necessary to ensure that uniform controllability and observabililty conditions are satisfied simultaneously.

A4. The environment contains a UAV-mounted receiver with imperfect knowledge of its initial states with $n \geq 2$ partially known SOP towers and $m \geq 1$ unknown SOP towers, i.e., the necessary observability condition $l \geq \frac{4+2n+4m}{n+m}$ is satisfied.

A5. The $m \geq 1$ unknown SOP spatial states' process noise terms contain a small non-zero value ($\epsilon \ll 1$) to ensure the process covariance is positive-definite.

2.3.1 Motivating Scenario

The following motivating scenario is considered. A UAV-mounted receiver is flying in a environment with initial access to GNSS signals from which an imperfect initial state estimate is calculated. GNSS signals became unavailable. Subsequently, the receiver produces pseudorange observations from ambient terrestrial SOPs. The pseudorange observations are fused through an EKF to estimate the states of both the (partially known and unknown) SOPs and UAV.

2.3.2 Boundedness of EKF Estimation Error Covariance

A uniform lower bound on the state covariance for a LTV stochastic system is valid when both uniform controllability and observability are satisfied simultaneously [92, 126]. Put another way, both the controllability and observability Grammians must be full rank (e.g., positive definite). These EKF estimation error covariance bounds have the following form

$$\left(\boldsymbol{\mathcal{O}}_{k,k-l} + \boldsymbol{\mathcal{C}}_{k,k-l}^{-1}\right)^{-1} \preceq \mathbf{P}_k, \tag{2.7}$$

where

$$\boldsymbol{\mathcal{C}}_{k,k-l} = \sum_{i=k-l}^{k-1} \boldsymbol{\Phi}(k, i+1)\mathbf{Q}\boldsymbol{\Phi}(k, i+1)^{\mathsf{T}}, \tag{2.8}$$

$$\boldsymbol{\mathcal{O}}_{k,k-l} = \sum_{i=k-l}^{k-1} \boldsymbol{\Phi}(i, k)^{\mathsf{T}}\mathbf{H}(i)^{\mathsf{T}}\bar{\mathbf{R}}^{-1}\mathbf{H}(i)\boldsymbol{\Phi}(i, k), \tag{2.9}$$

are the controllability Grammian (2.8) and observability Grammian (2.9), respectively. To simplify the upcoming derivation, the measurement noise covariance is assumed to be $\bar{\mathbf{R}} \triangleq \sigma^2\mathbf{I}_{M\times M}$, where $\sigma^2 \triangleq \max\{\sigma_{s_1}^2, \ldots, \sigma_{s_M}^2\}$.

2.3.3 Lower Bound on the EKF Estimation Error Covariance

The controllability and observability Grammians will be constructed at $l = 4$ epochs to the M terrestrial SOP towers based on the observability analysis in Section III. The Grammians matrices were computed to be

$$\boldsymbol{\mathcal{C}}_{k,k-4} = \sum_{i=k-4}^{k-1} \boldsymbol{\Phi}(k, i+1)\mathbf{Q}\boldsymbol{\Phi}(k, i+1)^{\mathsf{T}} = \sum_{i=1}^{4} \mathbf{F}^{i-1}\mathbf{Q}\left(\mathbf{F}^{i-1}\right)^{\mathsf{T}}$$

$$\boldsymbol{\mathcal{O}}_{k,k-4} = \frac{1}{\sigma^2}\sum_{i=k-4}^{k-1} \boldsymbol{\Phi}(i,k)^{\mathsf{T}}\mathbf{H}(i)^{\mathsf{T}}\mathbf{H}(i)\boldsymbol{\Phi}(i,k) = \frac{1}{\sigma^2}\sum_{i=1}^{4}\left(\mathbf{F}^{-i}\right)^{\mathsf{T}}\mathbf{H}(k-i)^{\mathsf{T}}\mathbf{H}(k-i)\mathbf{F}^{-i}$$

The controllability Grammian is constructed with linear-time invariant (LTI) matrices $\mathbf{Q}$ and $\mathbf{F}$. Thus, the controllability Grammian $\boldsymbol{\mathcal{C}}_{k,k-4}$ is a constant matrix which is a function of the covariance $\mathbf{Q}$. The observability Grammian matrix is constructed with LTI matrix $\mathbf{F}$ and LTV matrix $\mathbf{H}(k)^{\mathsf{T}}\mathbf{H}(k)$. Thus, the observabililty Grammian is a function of the observation Jacobian $\mathbf{H}(k)^{\mathsf{T}}\mathbf{H}(k)$. Therefore, the EKF estimation error bound defined in (2.7) is dependent on finding a real number $\bar{\alpha} > 0$ such that $\boldsymbol{\mathcal{O}}_{k,k-4} \preceq \bar{\alpha}\mathbf{I}$. The $\bar{\alpha}$ constant can be defined as the trace of the observability Grammian. A tighter upper-bound on the observability Grammian can be established by finding the maximum eigenvalue, but this is a difficult task since the observability Grammian is a LTV matrix. Therefore, the "looser" upper-bound is considered by defining $\bar{\alpha}$ to be the trace, rather than the maximum eigenvalue, of the observability Grammian. The trace is defined as the sum of all eigenvalues, i.e., $\text{Tr}[\boldsymbol{\mathcal{O}}_{k,k-4}] = \sum_{j=1}^{n_x}\lambda_j$ where n_x is the number of estimated states. Alternatively, the trace is defined to be the sum of the elements along the main diagonal of a matrix.

$$\boldsymbol{\mathcal{O}}_{k,k-4} \preceq \underbrace{\text{Tr}(\boldsymbol{\mathcal{O}}_{k,k-4})}_{\bar{\alpha}}\mathbf{I}, \qquad \text{where } \text{Tr}(\boldsymbol{\mathcal{O}}_{k,k-4}) = \frac{1}{\sigma^2}\sum_{i=1}^{n_x}\left[\boldsymbol{\mathcal{O}}_{k,k-4}\right]_{i,i} \tag{2.10}$$

$$(\bar{\alpha}\mathbf{I} + \boldsymbol{\mathcal{C}}_{k,k-4}^{-1}) \succeq (\boldsymbol{\mathcal{O}}_{k,k-4} + \boldsymbol{\mathcal{C}}_{k,k-4}^{-1})$$

$$\Rightarrow (\bar{\alpha}\mathbf{I} + \boldsymbol{\mathcal{C}}_{k,k-4}^{-1})^{-1} \preceq (\boldsymbol{\mathcal{O}}_{k,k-4} + \boldsymbol{\mathcal{C}}_{k,k-4}^{-1})^{-1} \preceq \mathbf{P}_k \tag{2.11}$$

Furthermore, the observability Grammian's trace, i.e., $\bar{\alpha} = \text{Tr}(\boldsymbol{\mathcal{O}}_{k,k-4})$, is calculated for the radio SLAM base case with $l \geq \frac{4+2n+4m}{n+m} = \frac{4+2(2)+4(1)}{3} = 4$. The considered scenario makes pseudorange observations at $l = 4$ epochs to the $M = 3$ terrestrial SOP towers in the environment. Defining matrix $B_i = \mathbf{H}(k-i)\mathbf{F}^{-i}$,

$$\text{Tr}(\boldsymbol{\mathcal{O}}_{k,k-4}) = \frac{1}{\sigma^2}\sum_{i=1}^{4}\text{Tr}(B_i^{\mathsf{T}}B_i) = \frac{1}{\sigma^2}\sum_{i=1}^{4}\sum_{j=1}^{n_x}||b_j||_2^2 \tag{2.12}$$

where b_j $\forall j = 1, \ldots, n_x$ are the columns of matrix B_i. The dynamics matrix has a Jordan form. Thus, it can be written as the summation of an identity matrix and an upper triangle hollow matrix which is only a function of the clock sampling time T, i.e, $\mathbf{F} = \mathbf{I} + \mathbf{F}_T$. It can be shown that $\mathbf{F}_T$ is a nilpotent matrix such that $\mathbf{F}_T^i = 0$, for $i \geq 2$. Therefore, the inverse of the dynamic propagation matrix can be calculated as $\mathbf{F}^{-1} = \mathbf{I} - \mathbf{F}_T$. Similarly, it can be shown that $\mathbf{F}^{\pm i} = \mathbf{I} \pm i\mathbf{F}_T$. These dynamics matrix properties are useful in characterizing the trace of the observability Grammian, as discussed in the following

$$
\begin{aligned}
B_i &= \mathbf{H}(k-i)\mathbf{F}^{-i} \\
&= \mathbf{H}(k-i) - i\mathbf{H}(k-i)\mathbf{F}_T \\
&= \begin{bmatrix}
\boldsymbol{\xi}_1^{\mathsf{T}}(k-i) & -iT\boldsymbol{\xi}_1^{\mathsf{T}}(k-i) & [1, -iT] & \mathbf{0}_{1\times 2} & \mathbf{0}_{1\times 2} & \mathbf{0}_{1\times 2} \\
\boldsymbol{\xi}_2^{\mathsf{T}}(k-i) & -iT\boldsymbol{\xi}_2^{\mathsf{T}}(k-i) & \mathbf{0}_{1\times 2} & [1, -iT] & \mathbf{0}_{1\times 2} & \mathbf{0}_{1\times 2} \\
\boldsymbol{\xi}_3^{\mathsf{T}}(k-i) & -iT\boldsymbol{\xi}_3^{\mathsf{T}}(k-i) & \mathbf{0}_{1\times 2} & \mathbf{0}_{1\times 2} & -\boldsymbol{\xi}_3^{\mathsf{T}}(k-i) & [1, -iT]
\end{bmatrix}, \\
\Rightarrow \mathrm{Tr}(B_i^{\mathsf{T}} B_i) &= \sum_{j=1}^{n_x} ||b_j||_2^2 = (1 + i^2T^2) \sum_{j=1}^{M} (1 + ||\boldsymbol{\xi}_j||_2^2) + ||\boldsymbol{\xi}_3||_2^2
\end{aligned}
$$

The above results can be generalized for M SOP towers where m of them are unknown and n of them are partially known. It should be noted that $||\boldsymbol{\xi}_j||_2 = 1$ for each SOP tower; as it is defined as the normalized distance between the receiver and each SOP tower. This result can be generalized to the following with m unknown SOPs and n partially known SOPs

$$
\mathrm{Tr}(B_i^{\mathsf{T}} B_i) = \sum_{j=1}^{n_x} ||b_j||_2^2 = (1 + i^2T^2) \sum_{j=1}^{M} (1 + ||\boldsymbol{\xi}_j||_2^2) + \sum_{j=1}^{m} ||\boldsymbol{\xi}_j||_2^2 = 2M(1 + i^2T^2) + m
$$

Finally, the trace of the observability Grammian for the l epochs that have been taken into account can be calculated.

$$\begin{aligned}\mathrm{Tr}(\boldsymbol{\mathcal{O}}_{k,k-l}) &= \frac{1}{\sigma^2}\sum_{i=1}^{l}\mathrm{Tr}(B_i^{\mathsf{T}}B_i) \\ &= \frac{l}{\sigma^2}\big[(2M+m)+MT^2\frac{(l+1)(2l+1)}{3}\big] \triangleq \bar{\alpha}(n,m,\sigma^2,T,l) \end{aligned} \tag{2.13}$$

The constant value $\bar{\alpha}$ calculated in (2.13) upper-bounds the observability Grammian where $\bar{\alpha}$ is a function of sampling time, partially known and unknown SOP towers, measurement noise, and l-step. Now, the $\bar{\alpha}$ constant is used to construct the linear time-invariant estimation error covariance with minimal uncertainty based on (2.11).

$$\mathbf{P}_{\mathrm{LB}} = \left(\bar{\alpha}\mathbf{I} + \boldsymbol{C}_{k,k-l}^{-1}\right)^{-1}$$

This uniform lower bound on $\mathbf{P}_k$ is valid with assumptions A1$-$A5 to simultaneously guarantee the necessary uniform controllability and uniform observability conditions for estimation error covariance matrix boundedness.

2.3.4 Simulation Results

This subsection presents simulation results demonstrating the derived theoretical lower bound for the radio SLAM base case. The UAV is flying at a fixed altitude with velocity random walk dynamics. During the flight, the UAV will draw and fuse pseudorange observations obtained from $M = 3$ SOP towers detected within a local neighborhood of the UAV. The simulation settings are summarized in Table 2.1.

Table 2.1: Radio SLAM Simulation Settings for the Receiver and each SOP

Parameter	Value
$\{n, m\}$	$\{2, 1\}$
$\boldsymbol{x}_r(0\|0)$	$[0, 50, 15, -1, 100, 10]^\mathsf{T}$
$\mathbf{P}_r(0\|0)$	$\text{diag}[25, 25, 9, 9, 30 \times 10^3, 3 \times 10^3]$
$\hat{\boldsymbol{x}}_r(0\|0)$	$\sim \mathcal{N}\left[\boldsymbol{x}_r(0\|0), \mathbf{P}_r(0\|0)\right]$
$\boldsymbol{r}_{s_i}(0)$	$\sim [\mathcal{U}[-100, 1000],\ \mathcal{U}[-300, 300]]^\mathsf{T}$
$\{\boldsymbol{x}_{s_i}(0)\}_{i=1}^3$	$\left[\boldsymbol{r}_{s_i}^\mathsf{T}, 1, 0.1\right]^\mathsf{T}$
$\mathbf{P}_s(0\|0)$	$(10^3) \cdot \text{diag}[1, 1, 30, 3]$
$\{\hat{\boldsymbol{x}}_{s_i}(0\|0)\}_{i=1}^3$	$\sim \mathcal{N}\left[\boldsymbol{x}_{s_i}(0), \mathbf{P}_s(0\|0)\right]$
$\{\mathbf{P}_{\text{clk},i}(0\|0)\}_{i=1}^3$	$(10^3) \cdot \text{diag}[30, 3]$
$\{h_{0,\text{r}},\ h_{-2,\text{r}}\}$	$\{9.4 \times 10^{-20},\ 3.8 \times 10^{-21}\}$
$\{h_{0,\text{s}_i},\ h_{-2,\text{s}_i}\}_{i=1}^3$	$\{8.0 \times 10^{-20},\ 4.0 \times 10^{-23}\}$
$\tilde{q}_x, \tilde{q}_y$	$0.1\ \text{m}^2/\text{s}^3$
$\left\{\sigma_{s_i}^2\right\}_{i=1}^3$	$25\ \text{m}^2$
T	$0.1\ \text{s}$

First, results highlighting the uniform estimation performance as a function of unknown SOPs are shown in Fig. 2.1. To ensure observability, $n = 2$ partially known SOPs are assumed to be known while the m unknown SOPs are varied from 1 to 50 in increments of two. The performance metric used is the A-optimality criteria, which is proportional to the average variance of the estimates [127], given by the trace of the estimation error covariance. It is important to note how the average variance increases as more unknown SOPs are included into the environment. Knowledge of this performance plot can motivate performance-based design or transmitter selection when there is uncertainty about the environment.

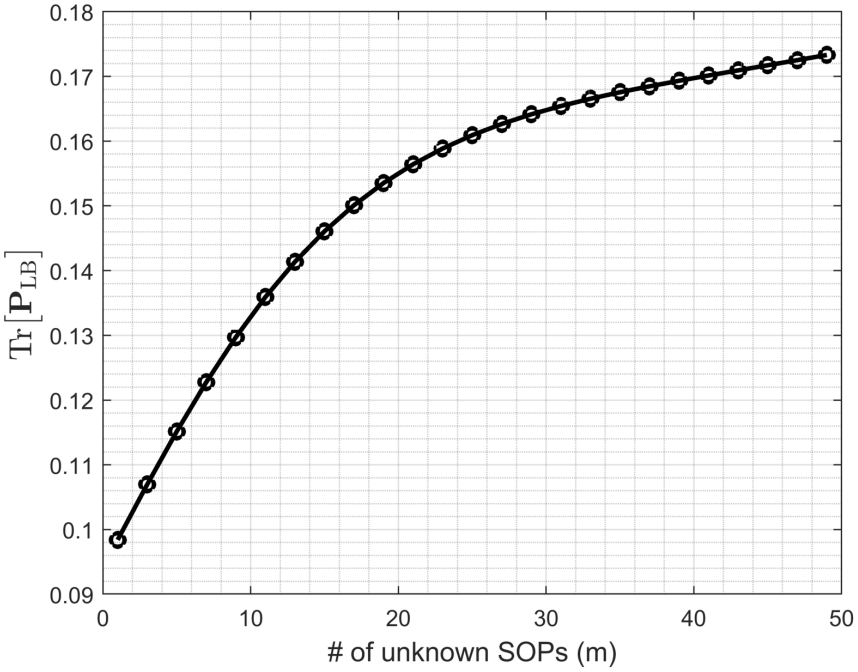

Figure 2.1: Uniform estimation performance as a function of unknown SOPs using the A-optimality criteria, i.e., $\mathrm{Tr}[\mathbf{P}_{\mathrm{LB}}]$.

Next, Monte Carlo (MC) simulations with 10^3 realizations were conducted to demonstrate the uniform lower bound on the EKF estimation error covariance. The process and measurement noise, initial state estimates, and the SOP tower locations were randomized for each MC realization. Fig. 2.2(a) displays the 1σ bounds of $\mathbf{P}(k|k)$ for the UAV and unknown SOP compared to the derived uniform lower bound. Fig. 2.2(b) displays an eigenvalue point cloud verifying $\mathbf{P}\left(k|k\right) \succeq \mathbf{P}_{\mathrm{LB}}$. It can be seen that, the minimum eigenvalue of the covariance's difference, i.e., $\lambda_{\min}[\mathbf{P}(k|k) - \mathbf{P}_{\mathrm{LB}}]$ will always be greater than or equal to zero at each time step for every MC realization.

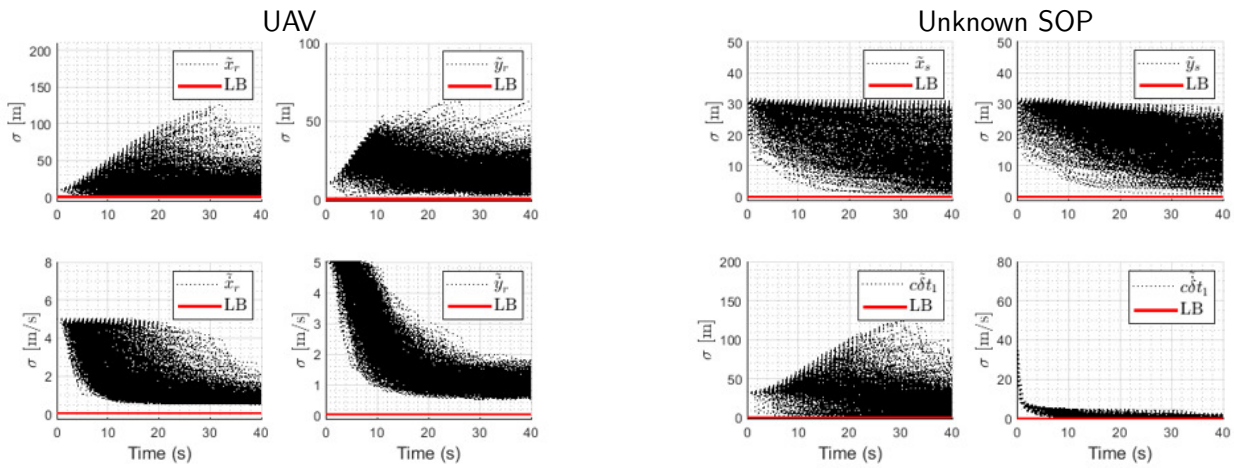

(a) 1σ bounds for localized UAV and unknown SOP

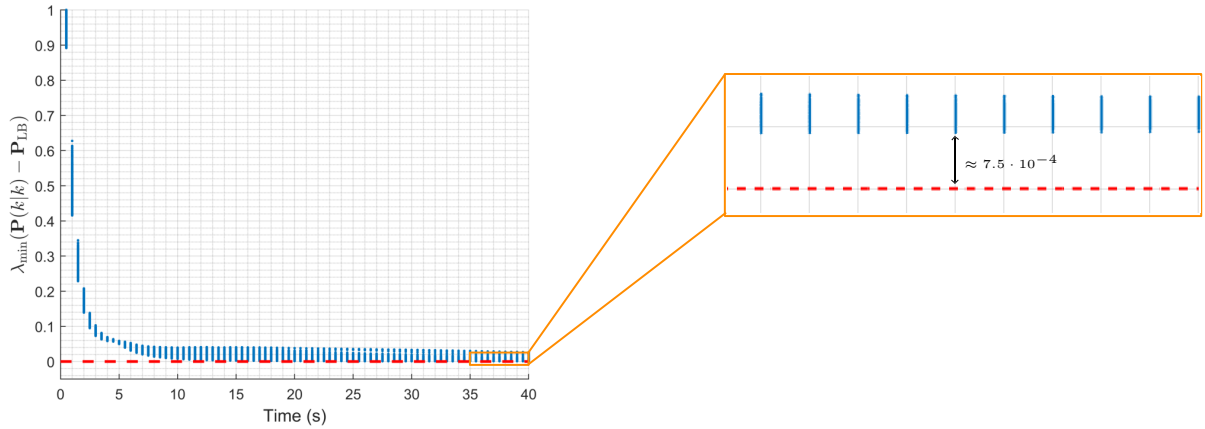

(b) Minimum eigenvalue point-cloud

Figure 2.2: Simulation results for 10^3 MC realizations. (a) 1σ bounds for the EKF estimation error covariance matrix compared with theoretical lower bound. (b) Minimum eigenvalue point cloud verifying $\mathbf{P}\left(k|k\right) \succeq \mathbf{P}_{\mathrm{LB}}$.

2.4 Experimental Results

A UAV field experiment was conducted in Mission Viejo, CA, USA, to demonstrate the estimation error trajectories and performance for the radio SLAM base case. This section presents the experimental hardware and software setup as well as the radio SLAM results using *only* pseudorange observations from $M = 3$ SOP towers in the environment.

2.4.1 Hardware and Software Setup

The hardware setup for the conducted experiment is shown in Fig. 2.3. A DJI Matrice 600 drone was equipped with a National Instrument (NI) universal software radio peripheral (USRP)-2955 to sample cellular long-term evolution (LTE) signals at four different carrier frequencies. LTE carrier frequencies 1955, 2145, 2125, and 739 MHz were used for this experiment which are allocated to USA operators AT&T, T-Mobile, and Verizon. The sampling rate was set to 10 MSps and the sampled LTE signals were recorded on a laptop. A Septentrio AsteRx-i V was used to estimate the position and orientation of the drone which was used as the ground truth. Furthermore, the Spetentrio was equipped with a dual antenna multi-frequency GNSS receiver with RTK and a Vectornav VN-100 micro electromechanical systems (MEMS) inertial measurement unit (IMU).

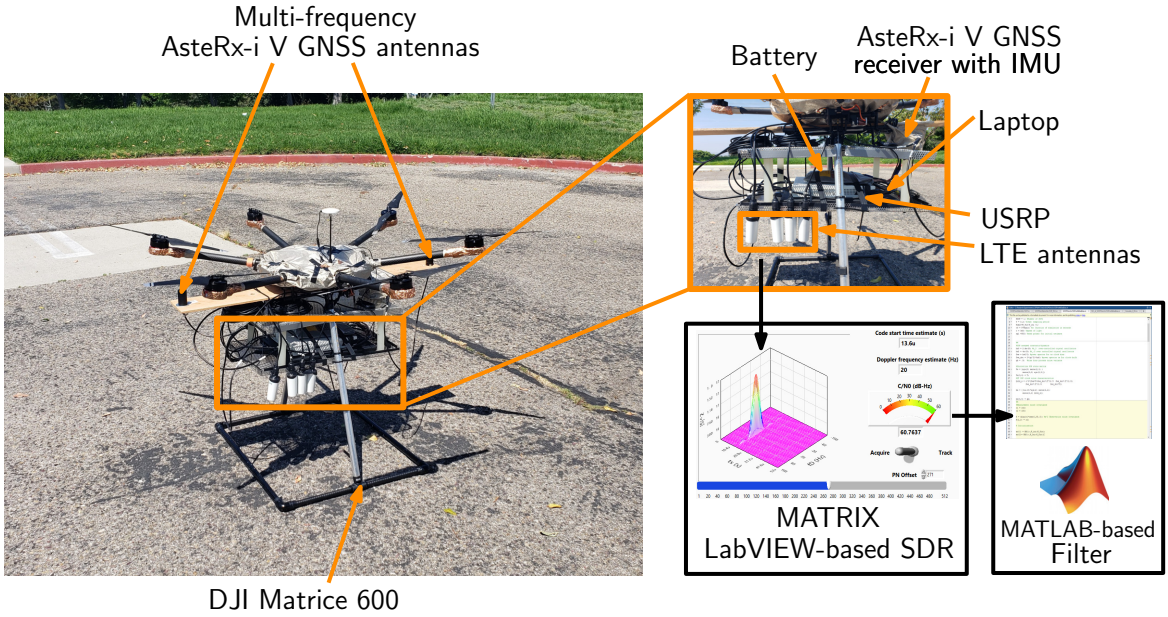

Figure 2.3: Experiment hardware setup.

The terrestrial SOP towers' cell IDs and their corresponding carrier frequencies are presented in Table 2.2. The sampled LTE signals were processed offline using the LTE software-defined radio (SDR) proposed in [128]. The resulting observations were used to simultaneously

localize the UAV-mounted receiver and unknown SOP tower while estimating all unknown clock error terms via the radio SLAM framework.

Table 2.2: eNodeBs' characteristics

Cell ID	**Carrier frequency (MHz)**
78	2145
104, 352	1955
308, 358, 224, 58, 354	2125
492, 5, 27	739

The UAV's and SOP towers' heights were assumed to be known for the entire duration of the experiment. Therefore, this is a 2-D radio SLAM problem consistent with the observability analysis and performance analysis conducted in Section III and Section IV, respectively. The EKF-based radio SLAM filter was initialized with state estimates and corresponding estimation error covariance given by the following

$$\begin{aligned}
\hat{\boldsymbol{x}}(0|0) =&[0,\ 0,\ 3.42,\ 0.81,\ -539.32,\ 0.16,\ -2237.52,\ 0.55,\ -150.71,\ 91.32,\ \ldots \\
&-143.11,\ 0.07]^{\mathsf{T}} \\
\mathbf{P}_r(0|0) =&\text{diag}\left[4,\ 4,\ 1, 1, 30\times10^6, 3\times10^3\right], \\
\mathbf{P}_{\text{clk},n}(0|0) =&\text{diag}\left[30\times10^6,\ 3\times10^3\right], \quad n=1,2 \\
\mathbf{P}_{s_3}(0|0) =&\text{diag}\left[7\times10^4,\ 7\times10^4, 30\times10^6,\ 3\times10^3\right]
\end{aligned}$$

where $\mathbf{P}(0|0)$ was initialized with the initial EKF estimation error covariance matrices listed above. The initial modified clock error terms were solved for by using the initial set of

cellular transmitter pseudoranges according to

$$c\delta t_i(0) = z_{s_i}(0) - \|\boldsymbol{r}_r(0) - \boldsymbol{r}_{s_i}\|_2, \quad i = 1, 2, 3$$
$$c\dot{\delta t}_i(0) = \frac{c\big(\delta t_i(1) - \delta t_i(0)\big)}{T},$$

where $\delta t_i(1) = z_{s_i}(1) - \|\boldsymbol{r}_r(1) - \boldsymbol{r}_{s_i}\|_2$ is the modified clock bias at time step $k = 1$. The receiver's clock covariance $\mathbf{Q}_{\text{clk},r}$ was set to correspond to a typical temperature-compensated crystal oscillator (TCXO) with $h_{0,r} = 9.4 \times 10^{-20}$ and $h_{-2,r} = 3.8 \times 10^{-21}$. The i^{th} SOP tower's clock covariance $\mathbf{Q}_{\text{clk},s_i}$ was set to correspond to a typical oven-controlled crystal oscillator (OCXO) with $h_{0,s_i} = 8 \times 10^{-20}$ and $h_{-2,s_i} = 4 \times 10^{-23}$, which is typical for cellular towers [129, 130]. The UAV's position and velocity states were assumed to evolve according to velocity random walk dynamics where $T = 0.01$ s is the sampling time and $\tilde{q}_x = 1$ m^2/s^3 and $\tilde{q}_y = 20$ m^2/s^3 is the x and y continuous-time acceleration noise spectra whose values were found empirically. The measurement noise was assumed to have a covariance $\mathbf{R} = \sigma^2 \cdot \mathbf{I}_{3\times 3}$, where $\sigma^2 = 30$ m^2 was found empirically.

2.4.2 Radio SLAM Base Case Results

The UAV traversed a trajectory of 600 m over 175 seconds, while listening to 11 terrestrial SOP towers in the surrounding environment which were mapped prior to conducting the experiment. Although, for the purposes of the radio SLAM case study, only $M = 3$ SOP towers were considered with $n = 2$ partially known SOPs and $m = 1$ unknown SOP. The UAV-mounted receiver's estimate errors were computed with respect to the RTK-IMU trajectory where the resulting estimation error trajectories and corresponding $\pm 1\sigma$ of the UAV's and the unknown SOP tower's states are shown in Fig. 2.4. Note, only the $\pm 1\sigma$ bounds are shown to highlight the radio SLAM base case estimation performance.

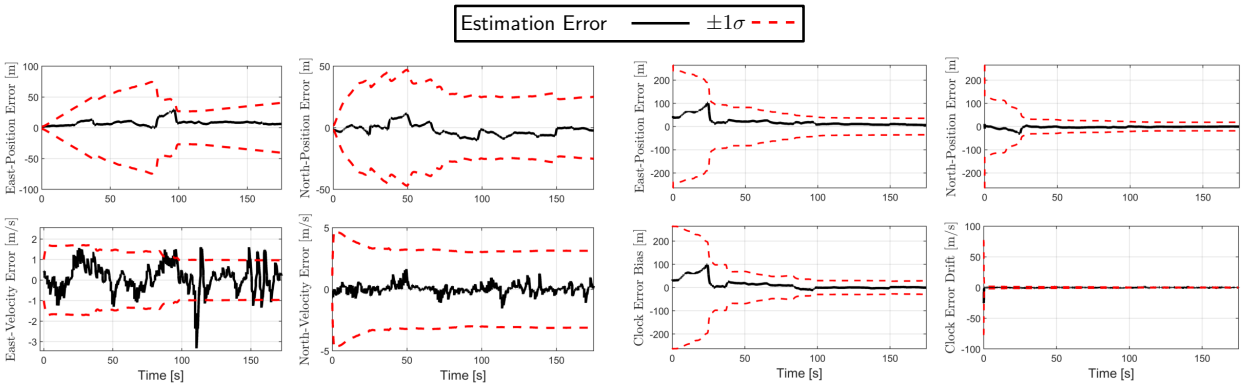

Figure 2.4: Radio SLAM base case experimental results showing the estimation error trajectories and corresponding $\pm 1\sigma$ bounds.

The experiment layout contains three cellular SOP tower locations and the true and estimated UAV trajectories as shown in Fig. 2.5(a). A comparison between the estimated UAV trajectory and the RTK-IMU solution trajectory is shown in Fig. 2.5(b). The UAV achieved a position root-mean squared error (RMSE) of 10.76 m after traversing the full trajectory. The north-east 95^{th}-percentile initial and final uncertainty ellipses corresponding to SOP tower 3 have a noticeable reduction in size by the end of the experiment. Moreover, the initial 2-D SOP tower position error was 41.57 m, but was eventually reduced to a final 2-D SOP tower position error of 6.62 m, as shown in Fig. 2.5(c). Furthermore, it should be noted that the radio SLAM error trajectories and performance results were all consistent with the theory and simulation results presented in Section IV.

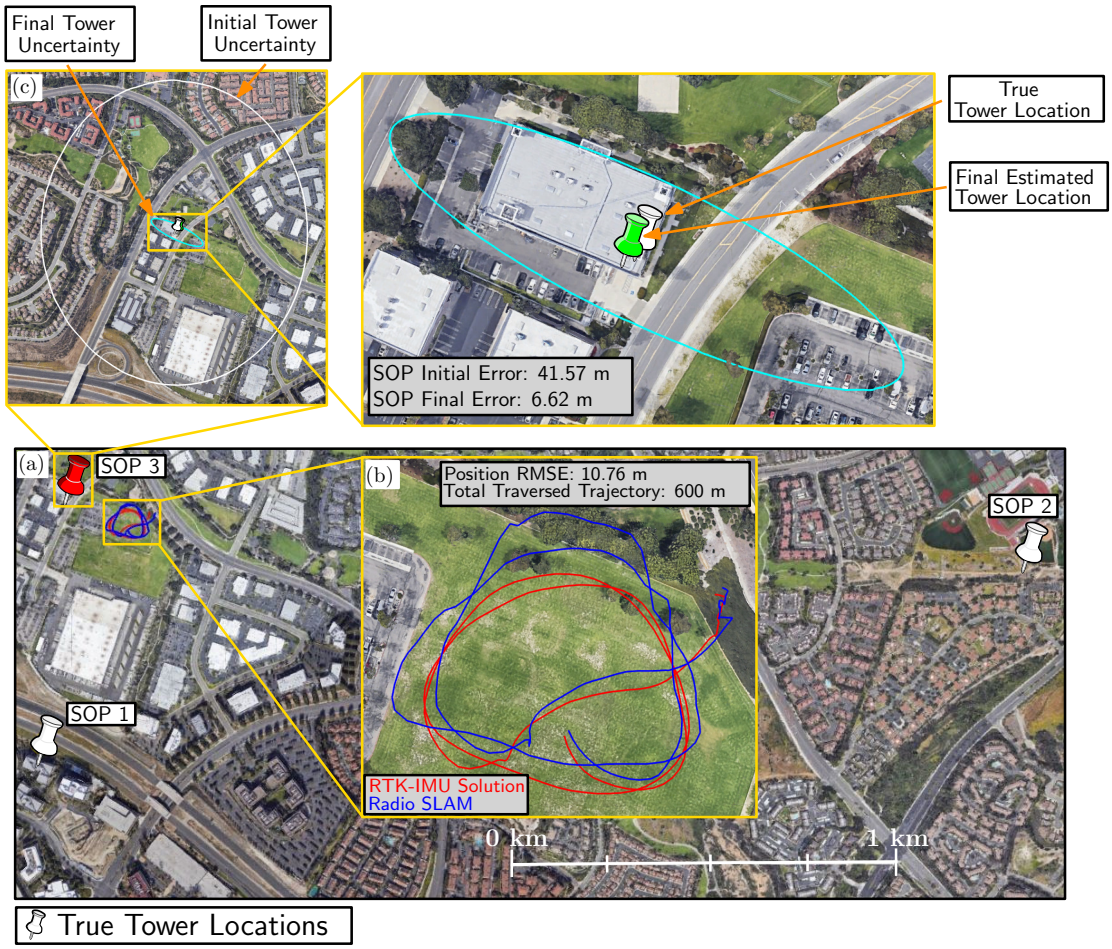

Figure 2.5: (a) Experiment layout containing the true locations of each SOP tower and the two UAV navigation solutions. (b) UAV trajectory comparison between the RTK-IMU navigation solution (red) and radio SLAM (blue). (c) Initial and final position estimates with their associated north-east uncertainty ellipse for SOP tower 3. Map data: Google Earth.

Chapter 3

Efficient Transmitter Selection Strategies for Improved Information Gathering with Terrestrial SOPs

Next, this chapter will present sub-optimal, yet computationally efficient, transmitter selection strategies for improved information gathering using the radio navigation, rather than the radio SLAM, framework. Furthermore, a performance analysis on the proposed transmitter selection strategies is conducted. This chapter is organized as follows. Section 3.1 describes the models employed and the problem description. Section 3.2 describes the proposed terrestrial SOP selection framework. Section 3.3 provides a comparison analysis of the different selection strategies for the one-dimensional (1–D) and two-dimensional (2–D) FIM cases and derives an upper bound on the FIM for the selected range-only observations. Section 3.4 presents simulation results comparing the performance of the different selection schemes, the effect of timing on the optimal transmitter selection, and computational complexity of the different selection strategies. Section 3.5 presents experimental results for a U.S. Air Force high altitude aircraft using the proposed selection frameworks in two different

emulated GNSS-denied environments over a valid selection region: (i) rural region and (ii) semi-urban region.

3.1 Model Description and Problem Description

In this section, the models adopted in this chapter are described and the transmitter selection problem is subsequently described.

3.1.1 Overview: Aerial Vehicle Model for SOP-Based Navigation

Consider an aerial vehicle equipped with an onboard receiver capable of listening to the ambient terrestrial SOPs (i.e., transmitters) in the environment.

These terrestrial SOPs are assumed to be spatially-stationary, and each SOP's state vector will consist of its three-dimensional (3–D) position vector $\boldsymbol{r}_{s_i} = [x_{s_i},\ y_{s_i}, z_{s_i}]^{\mathsf{T}}$ and the difference between the receiver's and SOP's clock error states $\boldsymbol{x}_{\text{clk},i} = c\left[\delta t_i,\ \delta \dot{t}_i\right]^{\mathsf{T}}$, where c is the speed of light, δt_i is the relative clock bias, and $\delta \dot{t}_i$ is the relative clock drift. Furthermore, the receiver's state vector will consist of the 3–D position vector and 3–D velocity vector given by $\boldsymbol{r}_r = [x_r,\ y_r,\ z_r]^{\mathsf{T}}$ and $\dot{\boldsymbol{r}}_r = [\dot{x}_r,\ \dot{y}_r,\ \dot{z}_r]^{\mathsf{T}}$, respectively.

The state vector will include the receiver's position, receiver's velocity, and each SOP tower's relative clock error states, defined as

$$\boldsymbol{x} \triangleq \left[\boldsymbol{r}_r^{\mathsf{T}},\ \dot{\boldsymbol{r}}_r^{\mathsf{T}},\ \boldsymbol{x}_{\text{clk},1}^{\mathsf{T}},\ \ldots,\ \boldsymbol{x}_{\text{clk},M}^{\mathsf{T}}\right]^{\mathsf{T}}.$$

The pseudorange observation made by the receiver to each SOP tower, after discretization

and mild approximations [82], is modeled as follows

$$z_{s_i}(k) = \underbrace{\left\|\boldsymbol{r}_r(k) - \boldsymbol{r}_{s_i}\right\|_2 + c\delta t_i(k)}_{h_i[\boldsymbol{x}(k)]} + v_{s_i}(k), \tag{3.1}$$

where M is the total number of SOPs in the environment and v_{s_i} is the i$^{\text{th}}$ SOP's measurement noise which is modeled as a zero-mean white Gaussian sequence with variance $\sigma^2_{s_i}$. Moreover, it is assumed that the measurement noise is independent across all the different terrestrial SOP towers.

For high altitudes, there is poor geometric diversity of terrestrial SOPs in the vertical direction. Therefore, allowing the aerial vehicle to rely exclusively on SOPs for 3–D navigation would lead to a large vertical dilution of precision (VDOP) [131, 132, 133]. Hence, it is assumed that the aerial vehicle is equipped with an altimeter to determine its altitude. As such, in what follows, the problem formulation will only consider the planar aerial vehicle states.

3.1.2 Fisher Information Matrix

The proposed transmitter selection strategies desire to choose the most informative observations. This motivates the adoption of the Fisher Information Matrix (FIM) [134, 135] which is given as

$$\begin{aligned}
\mathbf{I}(\boldsymbol{x}) &= \mathbb{E}\left[\left(\frac{\partial \ln\, p(\boldsymbol{z}|\boldsymbol{x})}{\partial \boldsymbol{x}}\right)\left(\frac{\partial \ln\, p(\boldsymbol{z}|\boldsymbol{x})}{\partial \boldsymbol{x}}\right)^{\mathsf{T}}\right] \\
&= \mathbf{I}_0(\boldsymbol{x}) + \sum_{i=1}^{M} \frac{1}{\sigma^2_{s_i}}\left(\frac{\partial h_i(\boldsymbol{x})}{\partial \boldsymbol{x}}\right)\left(\frac{\partial h_i(\boldsymbol{x})}{\partial \boldsymbol{x}}\right)^{\mathsf{T}}, \\
&= \mathbf{I}_0(\boldsymbol{x}) + \sum_{i=1}^{M} \mathbf{I}_i(\boldsymbol{x})
\end{aligned} \tag{3.2}$$

where $p(\boldsymbol{z}|\boldsymbol{x})$ is the likelihood function of the observations $\boldsymbol{z}$ parameterized by the states $\boldsymbol{x}$. Furthermore, the FIM can be simplified since the observation model in (3.1) is assumed to have additive Gaussian noise and the observation sequence $\{z_{s_i}\}_{i=1}^{M}$ is assumed to be independent across all SOP towers. These assumptions allow the FIM to simplify into (3.2), which is represented as the prior FIM plus a summation of the information content associated with each observation. Note, this is similar to the notion of the information matrix associated with observations (IMAO) discussed in the robotics literature [136, 137].

The additive property of information from different sources [138] will be utilized in the transmitter selection strategies. Denoting the (prior) information content associated with a subset of SOPs as $\mathbf{I}_0(\boldsymbol{x})$ and the information associated with the i$^{\text{th}}$ SOP as $\mathbf{I}_i(\boldsymbol{x})$, then the (posterior) information content associated with updating the SOP subset to include the i$^{\text{th}}$ SOP is defined as $\mathbf{I}_{\text{posterior},i}(\boldsymbol{x}) = \mathbf{I}_0(\boldsymbol{x}) + \mathbf{I}_i(\boldsymbol{x})$.

3.1.3 Static Estimation Framework

The transmitter selection estimation framework is formulated as a static system (i.e., no dynamics) with range-only observations. Note, the forthcoming simulation results will justify why using range-only observations, rather than psuedorange observations, is valid.

A static, weighted nonlinear least-squares (WNLS) estimator is employed on a redefined state vector $\boldsymbol{x}'$ and observation model $\boldsymbol{z}'_{s_i}$. Moreover, this batch estimation formulation will minimize a cost function subject to a constraint on the number of selected transmitters. The (static) states considered for estimation are the receiver's position states, defined as

$$\boldsymbol{x}' \triangleq \boldsymbol{r}_r.$$

The observation model is then redefined for range-only, rather than pseudorange, observa-

tions expressed as

$$z'_{s_i} = \|\boldsymbol{r}_r - \boldsymbol{r}_{s_i}\|_2 + v'_{s_i},$$

where $\boldsymbol{v} = [v'_{s_1},\ \ldots,\ v'_{s_M}]^{\mathsf{T}}$ is the measurement noise vector and v'_{s_i} is assumed to be a zero-mean white Gaussian sequence with variance $\sigma^2_{s'_i}$. As before, the measurement noise is assumed independent across all different terrestrial SOP towers.

The associated Jacobian matrix $\mathbf{H}$ of the (redefined) observation vector $\boldsymbol{z}' \triangleq [z'_{s_1},\ \ldots,\ z'_{s_M}]^{\mathsf{T}}$ is given by

$$\mathbf{H} = \frac{\boldsymbol{r}_r^{\mathsf{T}} - \boldsymbol{r}_{s_i}^{\mathsf{T}}}{\|\boldsymbol{r}_r - \boldsymbol{r}_{s_i}\|_2} \tag{3.3}$$

Subsequently, the estimation error covariance matrix of the WNLS estimator with M transmitters (terrestrial SOPs), denoted by $\mathbf{P}$, is given by

$$\mathbf{P} \triangleq \left[\mathbf{P}_0^{-1} + \mathbf{H}^{\mathsf{T}}\mathbf{R}^{-1}\mathbf{H}\right]^{-1}, \tag{3.4}$$

where a prior for $\boldsymbol{x}'$ may be given, denoted by $\hat{\boldsymbol{x}}'$, with an associated initial covariance $\mathbf{P}_0 (\triangleq \mathbf{I}_0^{-1}) \succ \mathbf{0}$, $\mathbf{H}$ is the Jacobian matrix of the (redefined) observation model, and $\mathbf{R} = \text{diag}[\sigma^2_{s'_1},\ \ldots,\ \sigma^2_{s'_M}]$ is the measurement covariance associated with the observations.

3.1.4 Problem Description

The problem addressed in this chapter is the sub-optimal, yet computationally efficient, selection of a transmitter subset. Furthermore, it is assumed this selection subset will remain valid over a segment of the aerial vehicle's current trajectory. Now, consider the following transmitter selection motivating problem scenario.

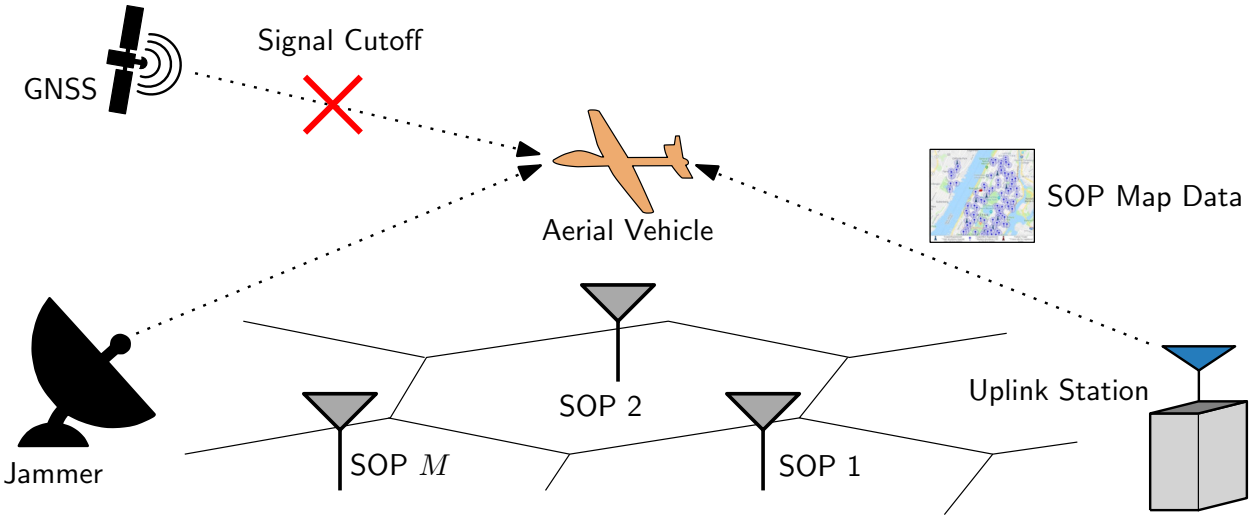

Figure 3.1: Problem description. An aerial vehicle is navigating in an unknown environment by exploiting the available GNSS signals. During its flight, the aerial vehicle experiences a GNSS outage (e.g., spoofing or jamming) which causes the available GNSS signals to become unreliable. Luckily, a nearby uplink station is able to send SOP map data to the aerial vehicle containing an exhaustive list of the available cellular tower locations in the area.

In Figure 3.1, an aerial vehicle is navigating in an unknown environment by exploiting the available GNSS signals. During its flight, the aerial vehicle experiences a GNSS outage (e.g., spoofing or jamming) which causes the available GNSS signals to become unreliable. Fortunately, a nearby uplink station is able to provide SOP map data containing an exhaustive list of the available cellular tower locations in the area. Now, the aerial vehicle is tasked to navigate by utilizing signals from the ambient terrestrial SOPs with *known* transmitter locations, but *unknown* clock error states, exclusively.

The aerial vehicle is assumed to be equipped with an onboard receiver capable of extracting pseudorange observations, modeled as (3.1), from the abundant number of ambient SOPs' signals. The aerial vehicle, then, fuses these observations through a dynamic estimator (e.g., EKF) but, due to size, weight, power, and cost (SWaP-C) limitations, or fusing all these signals is unnecessary since tracking a subset of the SOPs could yield a comparable performance, the aerial vehicle-mounted receiver is constrained to using a subset ($K < M$) of the total number of terrestrial SOPs in the environment. This prompts the question of

what is the "best" SOP subset to use? Fig. 3.2 illustrates a real-world environment in which this selection problem was encountered in Southern California, USA, where the white pins denote $M = 57$ cellular SOPs, which the aerial vehicle-mounted receiver was simultaneously tracking before it selected a SOP subset at the selection point (black cross).

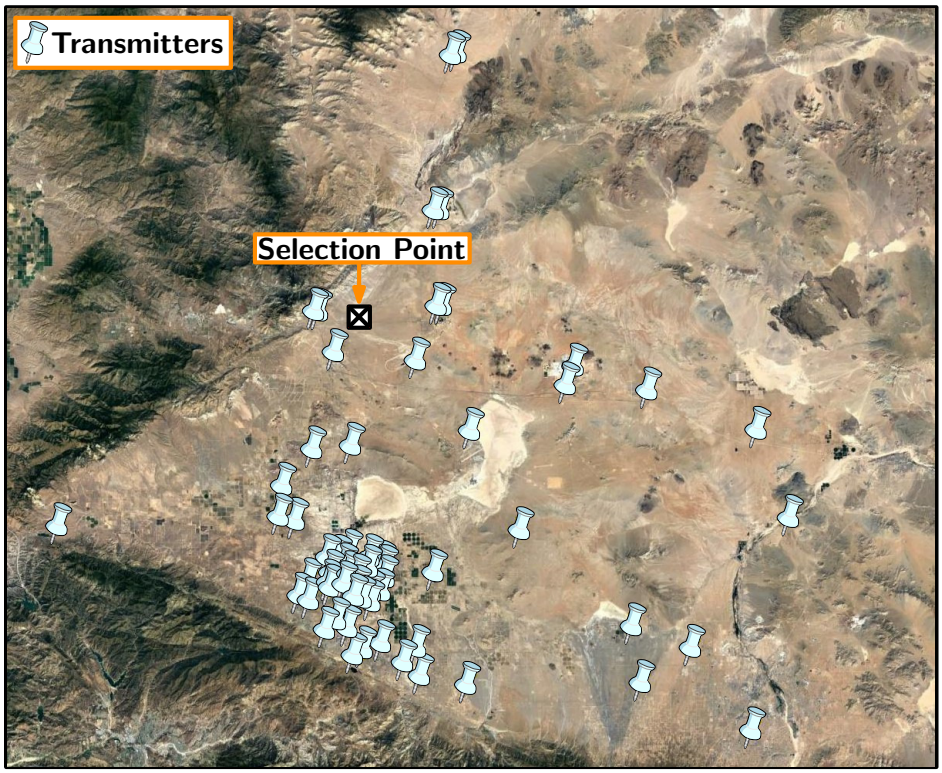

Figure 3.2: Motivating scenario. Terrestrial SOP towers (white) in the environment with respect to the aerial vehicle's selection point (black cross). Using all 57 SOP towers to navigate the aerial vehicle would violate SWaP-C constraints. As such, it is desired to choose the "best" subset of SOPs to use to navigate the aerial vehicle.

The transmitter selection problem can be cast as the following optimization problem

$$\begin{aligned} \underset{w}{\text{minimize}} \quad & \mathcal{J}(\boldsymbol{w}) \\ \text{subject to} \quad & \mathbf{1}_M^{\mathsf{T}} \boldsymbol{w} = K \\ & w_i \in \{0, 1\}, \quad i = 1, \ \ldots, M \end{aligned}$$

where $\mathcal{J}(\boldsymbol{w})$ denotes a desired cost function (e.g., A-optimality, D-optimality, E-optimality,

GDOP, ect.) [127, 139], w_i is a binary decision variable (determines whether to accept or reject the i$^{\text{th}}$ observation), $\boldsymbol{w} = [w_1, \ \ldots, \ w_M]^{\mathsf{T}}$ is a vector of the binary decision variables, $\mathbf{1}_M$ is a vector with M one entries, and K is the cardinality of the selection subset. This optimization problem is computationally involved to solve in real-time due to the integer constraints. Instead of directly solving the above optimization problem, two transmitter selection strategies are proposed. These selection strategies are discussed and analyzed in the forthcoming sections.

3.2 Terrestrial SOP Selection Framework

The proposed framework for transmitter selection is based on choosing the SOP subset that would minimize the aerial vehicle-mounted receiver's position error uncertainty, by maximizing information content. These selection strategies will leverage the additive property of information from different sources for determining the most informative observations via the FIM. Moreover, the 2×2 FIM corresponding to the i$^{\text{th}}$ SOP's range-only observation information content $\mathbf{I}_{\boldsymbol{r}_r,i}$, is used to evaluate the cost function $\mathcal{J}[\boldsymbol{w}]$. Ergo, this cost function is defined to be the A-optimality criterion [86]: the trace of the posterior estimation error covariance (equivalently, the trace of the inverse of the FIM), namely

$$\begin{aligned} \mathcal{J}\left[\boldsymbol{w}\right] &\triangleq \operatorname{tr}\left[\mathbf{I}_0' + \mathbf{H}'^{\mathsf{T}} \operatorname{diag}(\boldsymbol{w}) \mathbf{H}'\right]^{-1} \\ &= \operatorname{tr}\left[\mathbf{I}_0' + \sum_{i=1}^{M} w_i \mathbf{I}_{\boldsymbol{r}_r,i}\right]^{-1}, \end{aligned} \tag{3.5}$$

where $\mathbf{H}' \triangleq (\mathbf{R}_a^{-1})^{\mathsf{T}}\mathbf{H}$ is the modified Jacobian matrix, $\mathbf{R}_a$ is the upper triangular Cholesky factorized measurement covariance (i.e., $\mathbf{R} = \mathbf{R}_a^{\mathsf{T}}\mathbf{R}_a$), and $\mathbf{I}_0'$ is defined as the 2×2 prior FIM corresponding to the receiver's position states. Furthermore, the cost function can be redefined as the summation of the prior FIM $\mathbf{I}_0'$ and the FIM associated with the K

selected (out of the M total) SOP observations $\mathbf{I}_{\boldsymbol{r}_r,i}$ (decided by the binary decision variable $w_i \in \{0,\ 1\}$) as seen in (3.5).

Additionally if pseudorange observations were considered, rather than range-only observations, it is worth noting that the equivalent Fisher Information Matrix (EFIM) [140, 141] could also be employed. The EFIM will consider the information associated with the receiver's position states as well as the non-position states (i.e., clock bias states).

Opportunistic Greedy Selection

The opportunistic greedy selection (OGS) strategy, further described in [142], is a recursive selection strategy which proceeds as follows. First, an exhaustive search is performed to select the two SOPs which contain the largest information content associated with the receiver's position states $\mathbf{I}_{\boldsymbol{r}_r,i}$, according to the A-optimality criterion. This exhaustive search is necessary to ensure that the system is observable before implementing the OGS strategy. In [143], it was shown that at least two SOPs with known emitter locations are necessary to guarantee observability. Next, the information associated with each of the remaining SOP towers' position states is calculated (i.e., excluding the two already selected), then the one SOP with the highest information (as evaluated by the A-optimality criterion) is added into the selection subset. The prior FIM is updated accordingly (i.e., (old) prior FIM plus selected SOP's FIM). Then, the process of evaluating the information content for each of the remaining SOPs is repeated ($K-2$ iterations) until the selection subset contains the desired number of SOPs. Algorithm 1 details the proposed OGS steps.

One Shot Selection

The one shot selection (OSS) strategy is a batch selection strategy which proceeds as follows. First, as with the OGS strategy, an exhaustive search is performed to select the two SOPs

containing the largest information content associated with the receiver's position states $\mathbf{I}_{\boldsymbol{r}_{r,i}}$, according to the A-optimality criterion. As before, an exhaustive search is necessary to guarantee observability before implementing the OSS strategy. Next, the information associated with each of the remaining SOP towers' position states is calculated (i.e., excluding the two already selected). The $K-2$ SOP towers with the highest information (as evaluated by the A-optimality criterion) is added to the selection subset, and the FIM for selected SOPs is computed (i.e., prior FIM plus the selected SOPs' FIM). Note, this selection is performed in a single iteration to obtain a selection subset containing the desired number of SOPs. Algorithm 1 details the proposed OSS steps.

Algorithm 1 Transmitter Selection Strategies

Input: Prior FIM, FIM associated with each observation, indicator for each SOP, and number of selected SOPs

Output: SOP selection subset and FIM for selected SOPs

1: Define an empty set for SOP selection

2: Perform an exhaustive search to select the two SOPs with the largest information content

3: Update the prior FIM and SOP selection subset

Opportunistic Greedy Selection (OGS)

4: **for** $K-2$ **iterations**

5: Compute the posterior FIM for all SOPs, excluding those already selected

6: Choose one SOP which minimizes the receiver's average position uncertainty

7: Redefine the prior FIM (i.e., (old) prior FIM plus selected SOP's FIM) and update SOP selection subset

8: **end for**

9: **Return** the SOP selection subset and FIM for selected SOPs

One Shot Selection (OSS)

4: Compute the posterior FIM for all SOPs, excluding those already selected

5: Choose the $K-2$ SOPs which minimize the receiver's average position uncertainty

6: Compute the FIM for selected SOPs (i.e., prior FIM plus the selected SOPs' FIM) and SOP selection subset

7: **Return** the SOP selection subset and FIM for selected SOPs

---

3.3 Transmitter Selection Strategy Analysis

This section will compare the selection subsets for the proposed transmitter selection strategies and provide an upper bound on the FIM for the selected range-only observations.

3.3.1 Terrestrial SOP Selection Subset Comparison: 1–D Case

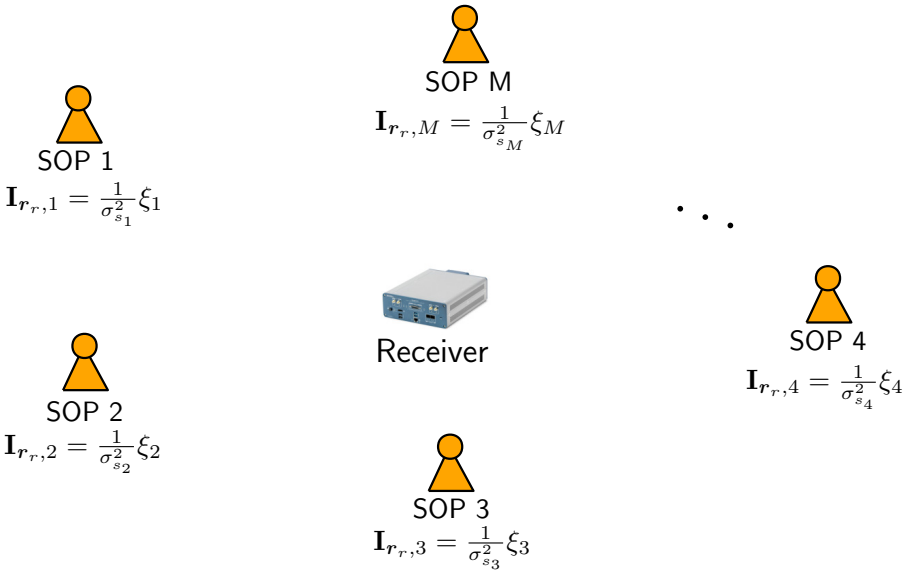

i-th SOP's Information Content $\equiv \mathbf{I}_{\boldsymbol{r}_r,i} \geq 0,\ \mathbf{I}_{\boldsymbol{r}_r,i} \in \mathbb{R} \quad \forall i = 1,\ \ldots,\ M$
Prior Information Content $\equiv \mathbf{I}_0 > 0,\ \mathbf{I}_0 \in \mathbb{R}$

Figure 3.3: A receiver estimating one of its states in an environment comprised of M terrestrial SOPs.

Consider the i$^{\text{th}}$ SOP's information content $\mathbf{I}_{\boldsymbol{r}_r,i}$ being represented by a scalar value associated with an estimated state, as shown in Figure 3.4. For simplicity, assume the cost function values from evaluating the posterior FIM $\mathbf{I}_{\text{posterior},i}$ are ranked (prior to selection) from smallest to largest such that $\mathcal{J}\left(\mathbf{I}_{\text{posterior},1}\right) \leq \mathcal{J}\left(\mathbf{I}_{\text{posterior},2}\right) \leq \ldots \leq \mathcal{J}\left(\mathbf{I}_{\text{posterior},K}\right) \leq \ldots \leq \mathcal{J}\left(\mathbf{I}_{\text{posterior},M}\right)$ where $\mathbf{I}_{\text{posterior},i} = \mathbf{I}_0 + \mathbf{I}_{\boldsymbol{r}_r,i}$.

Define the empty SOP selection subset as $S = \varnothing$. Furthermore, consider an arbitrary prior

FIM and information associated with the i$^{\text{th}}$ SOP are given as follows

$$\mathbf{I}_0 = \delta_0, \quad \mathbf{I}_{\boldsymbol{r}_r,i} = \frac{1}{\sigma^2_{s_i}}\xi_i$$

where $\mathbf{I}_0 = \delta_0 > 0$ and $\mathbf{I}_{\boldsymbol{r}_r,i} = \frac{1}{\sigma^2_{s_i}}\xi_i$ represents the information content associated with the i$^{\text{th}}$ SOP for the estimated state.

First, both the OSS and OGS strategies will perform an exhaustive search to determine the two most informative observations, as specified by the A-optimality criteria.

Exhaustive Search,

$$\begin{aligned}
&j_1^*, j_2^* = \underset{j_1,j_2}{\text{argmin}} \quad \text{tr}\left[\delta_0 \; + \; \sum_{\ell=1}^{2} \frac{\xi_{j_\ell}}{\sigma^2_{s_{j_\ell}}}\right]^{-1}, \\
&\Rightarrow j_1^* \equiv 1, \; j_2^* \equiv 2, \\
&\quad \text{since } \mathcal{J}\left[\delta_0 + \frac{\xi_1}{\sigma^2_{s_1}} + \frac{\xi_2}{\sigma^2_{s_2}}\right] \leq \mathcal{J}\left[\delta_0 + \frac{\xi_{j_1}}{\sigma^2_{s_{j_1}}} + \frac{\xi_{j_2}}{\sigma^2_{s_{j_2}}}\right], \quad \forall j_1, \; j_2 = 1, \ldots, M.
\end{aligned}$$

Update the prior information content to $\mathbf{I}_0' \triangleq \delta_0 + \frac{\xi_1}{\sigma^2_{s_1}} + \frac{\xi_2}{\sigma^2_{s_2}}$ and transmitter selection subset $S = \{1, 2\}$. Now, compute the posterior FIM as

$$\mathbf{I}_{\text{posterior},i} = \underbrace{\delta_0 + \sum_{j \in S} \frac{\xi_j}{\sigma^2_{s_j}}}_{\mathbf{I}_0' \triangleq \gamma_0 > 0} + \underbrace{\frac{\xi_i}{\sigma^2_{s_i}}}_{\mathbf{I}_{\boldsymbol{r}_r,i} \geq 0}$$

OSS strategy

The OSS strategy attempts to select the $K - 2$ most informative observations in a single iteration (i.e., batch selection) after performing the exhaustive search step.

Single Iteration Selection,

Select the transmitters which minimize the cost function defined as the average position uncertainty.

$$
\begin{aligned}
i_3^*, \ldots, i_K^* &= \underset{i_3,\ldots,i_K}{\operatorname{argmin}} \quad \operatorname{tr}\left[\gamma_0 + \sum_{i_\ell \notin S} \frac{\xi_{i_\ell}}{\sigma^2_{s_{i_\ell}}}\right]^{-1}, \quad \forall i_\ell = 1, \ldots, M \setminus \{S\} \\
&= \underset{i_3,\ldots,i_K}{\operatorname{argmin}} \quad \frac{1}{\gamma_0 + \sum_{i_\ell \notin S} \frac{\xi_{i_\ell}}{\sigma^2_{s_{i_\ell}}}} \\
\Rightarrow \quad \mathbf{I}_{i_3^*} &= \frac{\xi_3}{\sigma^2_{s_3}},\ \mathbf{I}_{i_4^*} = \frac{\xi_4}{\sigma^2_{s_4}},\ \ldots,\ \mathbf{I}_{i_K^*} = \frac{\xi_K}{\sigma^2_{s_K}}
\end{aligned}
$$

This optimization problem can invoke the simplifying assumption that $\mathbf{I}_{\text{posterior},i}$ is ranked from smallest to largest (i.e., $\mathcal{J}(\mathbf{I}'_0 + \mathbf{I}_{\boldsymbol{r}_r,3}) \leq \mathcal{J}(\mathbf{I}'_0 + \mathbf{I}_{\boldsymbol{r}_r,4}) \leq \ldots \leq \mathcal{J}(\mathbf{I}'_0 + \mathbf{I}_{\boldsymbol{r}_r,K})$). Therefore, the transmitter selection subset will be defined as $S = \{1, 2, \ldots, K\} = \{j \in \mathbb{N} \mid j = 1, 2, \ldots, K\}$. Furthermore, the information content associated with the selected transmitters is computed as $\mathbf{I} = \delta_0 + \frac{\xi_1}{\sigma^2_{s_1}} + \ldots + \frac{\xi_K}{\sigma^2_{s_K}}$.

OGS strategy

The OGS strategy attempts to select the $K-2$ most informative observations in $K-2$ iterations (i.e., recursive selection) after performing the exhaustive search step.

Iteration 1,

Recursively select one transmitter which minimizes the cost function defined as the average position uncertainty.

$$
\begin{aligned}
i^* &= \underset{i}{\operatorname{argmin}} \quad \operatorname{tr}\left[\gamma_0 + \frac{\xi_i}{\sigma^2_{s_i}}\right]^{-1}, \quad \forall i = 1, \ldots, M \setminus \{S\} \\
&= \underset{i}{\operatorname{argmin}} \quad \frac{1}{\gamma_0 + \frac{\xi_i}{\sigma^2_{s_i}}} \\
\Rightarrow \mathbf{I}_{i^*} &= \frac{\xi_3}{\sigma^2_{s_3}}
\end{aligned}
$$

The prior information content can be updated to $\mathbf{I}_0' = \gamma_0 + \frac{\xi_3}{\sigma_{s_3}^2}$ and the selection subset is updated accordingly $S = \{1,\ 2,\ 3\}$.

Iterations $2 \rightarrow K-2$,

Select one transmitter which minimizes the cost function defined as the average position uncertainty.

$$\begin{aligned} i^* &= \underset{i}{\text{argmin}} \quad \text{tr}\left[\gamma_0 + \frac{\xi_3}{\sigma_{s_3}^2} + \frac{\xi_i}{\sigma_{s_i}^2}\right]^{-1}, \quad \forall i = 1, \ldots, M \setminus \{S\} \\ &= \underset{i}{\text{argmin}} \quad \frac{1}{\gamma_0 + \frac{\xi_3}{\sigma_{s_3}^2} + \frac{\xi_i}{\sigma_{s_i}^2}} \\ \Rightarrow \mathbf{I}_{i^*} &= \frac{\xi_4}{\sigma_{s_4}^2} \end{aligned}$$

Continue this recursive selection process at each iteration. By virtue of the simplifying assumption, the minimum argument will be the next smallest ranked cost function and will be selected in ascending order as $i^* = 4$ (i.e., $\mathcal{J}(\mathbf{I}_0' + \mathbf{I}_{\boldsymbol{r}_r,4}) \leq \mathcal{J}(\mathbf{I}_0' + \mathbf{I}_{\boldsymbol{r}_r,i}) \quad \forall i \setminus \{S\})$, $i^* = 5$ (i.e., $\mathcal{J}(\mathbf{I}_0' + \mathbf{I}_{\boldsymbol{r}_r,5}) \leq \mathcal{J}(\mathbf{I}_0' + \mathbf{I}_{\boldsymbol{r}_r,i}) \quad \forall i \setminus \{S\})$, $\ldots$, $i^* = K$ (i.e., $\mathcal{J}(\mathbf{I}_0' + \mathbf{I}_{\boldsymbol{r}_r,K}) \leq \mathcal{J}(\mathbf{I}_0' + \mathbf{I}_{\boldsymbol{r}_r,i}) \quad \forall i \setminus \{S\})$. Therefore, the transmitter selection subset will be defined as $S = \{1, 2, \ldots, K\} = \{j \in \mathbb{N} \mid j = 1, 2, \ldots, K\}$. Furthermore, the information content associated with the selected transmitters is computed as $\mathbf{I} = \delta_0 + \frac{\xi_1}{\sigma_{s_1}^2} + \ldots + \frac{\xi_K}{\sigma_{s_K}^2}$.

Remark: If the information content is scalar valued (i.e., $\hat{x} \in \mathbb{R}$), the selection subset for the OGS and OSS strategies are equivalent. Moreover, it was found numerically that the selection subsets associated with the OGS and OSS strategies are equal to the optimal selection's subset for the scalar case.

3.3.2 Terrestrial SOP Selection Subset Comparison: 2–D Case

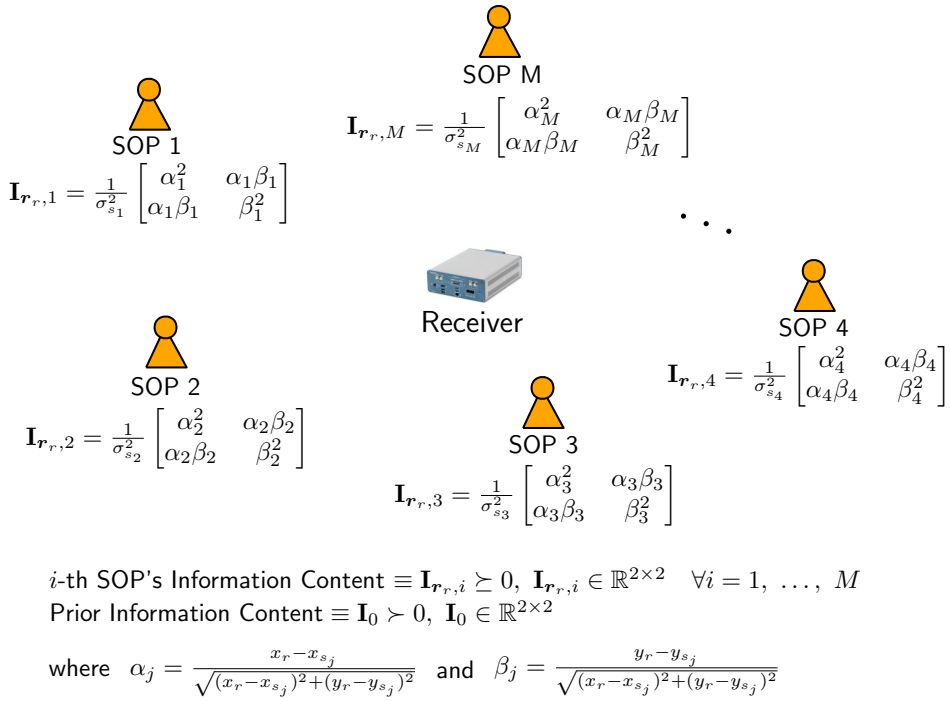

Figure 3.4: A receiver estimating its two position states in an environment comprised of M terrestrial SOPs.

Consider the i$^{\text{th}}$ SOP's information content being represented by the 2×2 FIM associated with the receiver's position states $\mathbf{I}_{\boldsymbol{r}_r,i}$, as shown in Figure 3.4. For simplicity, assume the cost function values from evaluating the posterior FIM $\mathbf{I}_{\text{posterior},i}$ are ranked (prior to selection) from smallest to largest such that $\mathcal{J}\left(\mathbf{I}_{\text{posterior},1}\right) \leq \mathcal{J}\left(\mathbf{I}_{\text{posterior},2}\right) \leq \ldots \leq \mathcal{J}\left(\mathbf{I}_{\text{posterior},K}\right) \leq \ldots \leq \mathcal{J}\left(\mathbf{I}_{\text{posterior},M}\right)$ where $\mathbf{I}_{\text{posterior},i} = \mathbf{I}_0 + \mathbf{I}_{\boldsymbol{r}_r}$.

Define the empty SOP selection subset $S = \varnothing$. Furthermore, consider an arbitrary prior FIM and information associated with the i$^{\text{th}}$ SOP are given as follows

$$\mathbf{I}_0 = \begin{bmatrix} \delta_{11} & \delta_{12} \\ \delta_{12} & \delta_{22} \end{bmatrix}, \quad \mathbf{I}_{\boldsymbol{r}_r,i} = \frac{1}{\sigma^2_{s_i}} \begin{bmatrix} \alpha_i^2 & \alpha_i\beta_i \\ \alpha_i\beta_i & \beta_i^2 \end{bmatrix}$$

where $\alpha_i = \frac{x_r - x_{s_i}}{\sqrt{(x_r-x_{s_i})^2+(y_r-y_{s_i})^2}}$ and $\beta_i = \frac{y_r - y_{s_i}}{\sqrt{(x_r-x_{s_i})^2+(y_r-y_{s_i})^2}}$ are variables which define the

position unit vectors (i.e., $[\alpha_i,\ \beta_i]^{\mathsf{T}} = \frac{\boldsymbol{r}_r - \boldsymbol{r}_{s_i}}{\|\boldsymbol{r}_r - \boldsymbol{r}_{s_i}\|_2}$).

First, both the OSS and OGS strategies will perform an exhaustive search to determine the two most informative observations, as specified by the A-optimality criteria.

Exhaustive Search,

$$
\begin{aligned}
&j_1^*, j_2^* = \underset{j_1, j_2}{\operatorname{argmin}} \quad \operatorname{tr}\left(\left[\mathbf{I}_0 \ + \ \sum_{\ell=1}^{2} \mathbf{I}_{\boldsymbol{r}_r, j_\ell}\right]^{-1}\right), \\
&\Rightarrow j_1^* \equiv 1,\ j_2^* \equiv 2 \\
&\quad \text{since, } \mathcal{J}\left[\mathbf{I}_0 + \mathbf{I}_{\boldsymbol{r}_r,1} + \mathbf{I}_{\boldsymbol{r}_r,2}\right] \leq \mathcal{J}\left[\mathbf{I}_0 + \mathbf{I}_{\boldsymbol{r}_r,j_1} + \mathbf{I}_{\boldsymbol{r}_r,j_2}\right], \quad \forall j_1,\ j_2 = 1, \ldots, M.
\end{aligned}
$$

Update the prior information content to $\mathbf{I}_0' \triangleq \mathbf{I}_0 + \mathbf{I}_1 + \mathbf{I}_2$ and transmitter selection subset $S = \{1, 2\}$. Now, compute the posterior FIM as

$$
\begin{aligned}
\mathbf{I}_{\text{posterior},i} &= \underbrace{\mathbf{I}_0 + \mathbf{I}_{\boldsymbol{r}_r,1} + \mathbf{I}_{\boldsymbol{r}_r,2}}_{\mathbf{I}_0'} + \mathbf{I}_{\boldsymbol{r}_r,i}, \quad \forall i = 1, \ldots, M \setminus \{S\} \\
&= \begin{bmatrix} \delta_{11} & \delta_{12} \\ \delta_{12} & \delta_{22} \end{bmatrix} + \sum_{j \in S} \frac{1}{\sigma_{s_j}^2} \begin{bmatrix} \alpha_j^2 & \alpha_j\beta_j \\ \alpha_j\beta_j & \beta_j^2 \end{bmatrix} + \frac{1}{\sigma_{s_i}^2} \begin{bmatrix} \alpha_i^2 & \alpha_i\beta_i \\ \alpha_i\beta_i & \beta_i^2 \end{bmatrix} \\
&\triangleq \underbrace{\begin{bmatrix} \gamma_{11} & \gamma_{12} \\ \gamma_{12} & \gamma_{22} \end{bmatrix}}_{\mathbf{I}_0' \succ 0} + \underbrace{\frac{1}{\sigma_{s_i}^2} \begin{bmatrix} \alpha_i^2 & \alpha_i\beta_i \\ \alpha_i\beta_i & \beta_i^2 \end{bmatrix}}_{\mathbf{I}_{\boldsymbol{r}_r,i} \succeq 0}
\end{aligned}
$$

OSS strategy

The OSS strategy attempts to select the $K - 2$ most informative observations in a single iteration (i.e., batch selection) after performing the exhaustive search step.

Single Iteration Selection,

Select the transmitters which minimize the cost functional defined as the average position uncertainty.

$$
\begin{aligned}
i_3^*, \ldots, i_K^* &= \underset{i_3,\ldots,i_K}{\text{argmin}} \quad \text{tr}\left[\mathbf{I}_{\text{posterior},i_\ell}^{-1}\right], \quad \forall i_\ell = 1, \ldots, M \setminus \{S\} \\
&= \underset{i_3,\ldots,i_K}{\text{argmin}} \quad \text{tr}\left(\begin{bmatrix} \gamma_{11} + \sum_{i_\ell \notin S} \frac{\alpha_{i_\ell}^2}{\sigma_{s_{i_\ell}}^2} & \gamma_{12} + \sum_{i_\ell \notin S} \frac{\alpha_{i_\ell}\beta_{i_\ell}}{\sigma_{s_{i_\ell}}^2} \\ \gamma_{12} + \sum_{i_\ell \notin S} \frac{\alpha_{i_\ell}\beta_{i_\ell}}{\sigma_{s_{i_\ell}}^2} & \gamma_{22} + \sum_{i_\ell \notin S} \frac{\beta_{i_\ell}^2}{\sigma_{s_{i_\ell}}^2} \end{bmatrix}^{-1}\right) \\
&= \underset{i_3,\ldots,i_K}{\text{argmin}} \quad \frac{\gamma_{11} + \gamma_{22} + \sum_{i_\ell \notin S}(\frac{\beta_{i_\ell}^2}{\sigma_{s_{i_\ell}}^2} + \frac{\alpha_{i_\ell}^2}{\sigma_{s_{i_\ell}}^2})}{(\gamma_{11} + \sum_{i_\ell \notin S} \frac{\alpha_{i_\ell}^2}{\sigma_{s_{i_\ell}}^2})(\gamma_{22} + \sum_{i_\ell \notin S} \frac{\beta_{i_\ell}^2}{\sigma_{s_{i_\ell}}^2}) - (\gamma_{12} + \sum_{i_\ell \notin S} \frac{\alpha_{i_\ell}\beta_{i_\ell}}{\sigma_{s_{i_\ell}}^2})^2}
\end{aligned}
$$

$$
\Rightarrow \quad \mathbf{I}_{i_3^*} = \mathbf{I}_{\boldsymbol{r}_r,3},\ \mathbf{I}_{i_4^*} = \mathbf{I}_{\boldsymbol{r}_r,4},\ \ldots,\ \mathbf{I}_{i_K^*} = \mathbf{I}_{\boldsymbol{r}_r,K}
$$

This optimization problem invokes the simplifying assumption that $\mathbf{I}_{\text{posterior},i}$ is ranked from smallest to largest (i.e., $\mathcal{J}(\mathbf{I}_0' + \mathbf{I}_{\boldsymbol{r}_r,3}) \leq \mathcal{J}(\mathbf{I}_0' + \mathbf{I}_{\boldsymbol{r}_r,4}) \leq \ \ldots \leq \mathcal{J}(\mathbf{I}_0' + \mathbf{I}_{\boldsymbol{r}_r,K})$). Therefore, the transmitter selection subset will be defined as $S = \{1, 2, \ldots, K\} = \{j \in \mathbb{N} \mid j = 1, 2, \ldots, K\}$. Furthermore, the information content associated with the selected transmitters is computed as $\mathbf{I} = \mathbf{I}_0 + \mathbf{I}_{\boldsymbol{r}_r,1} + \mathbf{I}_{\boldsymbol{r}_r,2} + \ldots + \mathbf{I}_{\boldsymbol{r}_r,K}$.

OGS strategy

The OGS strategy attempts to select the $K-2$ most informative observations in $K-2$ iterations (i.e., recursive selection) after performing the exhaustive search step.

Iteration 1,

Select one transmitter which minimizes the cost function defined as the average position

uncertainty.

$$
\begin{aligned}
i^* &= \underset{i}{\text{argmin}} \quad \text{tr}\left[\mathbf{I}_{\text{posterior},i}^{-1}\right], \quad \forall i = 1, \ldots, M \setminus \{S\} \\
&= \underset{i}{\text{argmin}} \quad \text{tr}\begin{bmatrix} \gamma_{11} + \frac{\alpha_i^2}{\sigma_{s_i}^2} & \gamma_{12} + \frac{\alpha_i \beta_i}{\sigma_{s_i}^2} \\ \gamma_{12} + \frac{\alpha_i \beta_i}{\sigma_{s_i}^2} & \gamma_{22} + \frac{\beta_i^2}{\sigma_{s_i}^2} \end{bmatrix}^{-1} \\
&= \underset{i}{\text{argmin}} \quad \frac{\gamma_{11} + \frac{\alpha_i^2}{\sigma_{s_i}^2} + \gamma_{22} + \frac{\beta_i^2}{\sigma_{s_i}^2}}{(\gamma_{11} + \frac{\alpha_i^2}{\sigma_{s_i}^2})(\gamma_{22} + \frac{\beta_i^2}{\sigma_{s_i}^2}) - (\gamma_{12} + \frac{\alpha_i \beta_i}{\sigma_{s_i}^2})^2} \\
\Rightarrow \mathbf{I}_{i^*} &= \mathbf{I}_{\boldsymbol{r}_r,3}
\end{aligned}
$$

By invoking the simplifying assumption, $\mathcal{J}(\mathbf{I}_0' + \mathbf{I}_{\boldsymbol{r}_r,3}) \leq \mathcal{J}(\mathbf{I}_0' + \mathbf{I}_{\boldsymbol{r}_r,i}))\ \forall i \setminus \{S\}$. Therefore, the prior information content can be updated to $\mathbf{I}_0' = \mathbf{I}_0 + \mathbf{I}_{\boldsymbol{r}_r,1} + \mathbf{I}_{\boldsymbol{r}_r,2} + \mathbf{I}_{\boldsymbol{r}_r,3}$ and the selection subset is updated accordingly $S = \{1,\ 2,\ 3\}$. Moreover, $\gamma_{11}' = \gamma_{11} + \frac{\alpha_3^2}{\sigma_{s_3}^2}$, $\gamma_{12}' = \gamma_{12} + \frac{\alpha_3 \beta_3}{\sigma_{s_3}^2}$, and $\gamma_{22}' = \gamma_{22} + \frac{\beta_3^2}{\sigma_{s_3}^2}$

Iterations $2 \rightarrow K - 2$,

Recursively select one transmitter which minimizes the cost function defined as the average position uncertainty.

$$
\begin{aligned}
i^* &= \underset{i}{\text{argmin}} \quad \text{tr}\left[\mathbf{I}_{\text{posterior},i}^{-1}\right], \quad \forall i = 1, \ldots, M \setminus \{S\} \\
&= \underset{i}{\text{argmin}} \quad \frac{\gamma_{11}' + \frac{\alpha_i^2}{\sigma_{s_i}^2} + \gamma_{22}' + \frac{\beta_i^2}{\sigma_{s_i}^2}}{(\gamma_{11}' + \frac{\alpha_i^2}{\sigma_{s_i}^2})(\gamma_{22}' + \frac{\beta_i^2}{\sigma_{s_i}^2}) - (\gamma_{12}' + \frac{\alpha_i \beta_i}{\sigma_{s_i}^2})^2}
\end{aligned}
$$

In iterations 2 through $K - 2$, the optimization problem's solution is heavily dependent on the cross-terms associated with the i$^{\text{th}}$ SOP's posterior FIM $\mathbf{I}_{\text{posterior},i}$. Specifically, from the addition of the updated prior FIM $\mathbf{I}_0'$ (i.e., γ_{11}', γ_{22}', and γ_{12}') plus the information content associated with the i$^{\text{th}}$ SOP's observation $\mathbf{I}_{\boldsymbol{r}_r,i}$, which are coupled in the 2×2 matrix inverse. In addition, the determinant incorporates the information shared between the x_r and y_r

position state estimates of the receiver. Therefore, the simplifying assumption will likely no longer be valid (i.e., $\mathcal{J}(\mathbf{I}'_0 + \mathbf{I}_{\boldsymbol{r}_r,3}) \not\preceq \mathcal{J}(\mathbf{I}'_0 + \mathbf{I}_{\boldsymbol{r}_r,i})) \ \forall i \setminus \{S\}$) and the transmitter selection at iteration 2 through $K-2$ (i.e., for $K > 3$) should yield a different selection subset than the OSS strategy.

Remark: If the information content is matrix valued (i.e., $\hat{\boldsymbol{x}} \in \mathbb{R}^2$) and $K > 3$, the SOP selection subset for OGS and OSS strategies are not likely to be equivalent. Moreover, these SOP selection subsets will be sub-optimal for the matrix case.

3.3.3 Upper Bound on the Fisher Information Matrix

This section derives an upper bound on the FIM for the selected range-only observations. Recall, the FIM is defined as the addition of the prior FIM and a summation of the information content associated with the selected range-only observations. It is assumed the associated initial estimation error covariance can be an arbitrary positive-definite, symmetric matrix (e.g., $\mathbf{P}_0 = \text{diag}\,[p_x,\ p_y]$). Furthermore, the information content associated with the range-only observations is given by $\mathbf{H}^\intercal \mathbf{R}^{-1} \mathbf{H}$, as shown in (B.2). In what follows, an upper bound on the FIM, given as the inverse of the estimation error covariance in (3.4), is developed.

The prior FIM (or, inverse of initial estimation error covariance matrix) and the information content associated with the range-only observations can be upper bounded by the following positive-valued scalars

$$\mathbf{I}_0 \triangleq \mathbf{P}_0^{-1} \ \preceq \bar{\eta} \mathbf{I}_{K \times K}, \tag{3.6}$$

$$\mathbf{H}^\intercal \mathbf{R}^{-1} \mathbf{H} \ \preceq \bar{\phi} \mathbf{I}_{K \times K}, \tag{3.7}$$

where, $\bar{\eta} \equiv \lambda_{\max}\left[\mathbf{P}_0^{-1}\right]$ and $\bar{\phi} \equiv \text{tr}[\mathbf{H}^\intercal \mathbf{R}^{-1} \mathbf{H}] = \sum_{j=1}^{K} \frac{1}{\sigma_{s_j}^2}$. The constants, $\bar{\eta}$ and $\bar{\phi}$, employ

an eigendecomposition of their, respective, positive definite, symmetric matrices to establish an upper bound via the maximum eigenvalue (i.e., $\lambda_{\max}$), or the trace (i.e., $\sum_{i=1}^{n_x} \lambda_i$ where n_x is the number of estimated states), of the matrix.

Now, the desired upper bound on the (posterior) FIM can be established by combining the results of (3.6) and (3.7) together. Recall, the FIM is defined as the sum of the prior FIM and the information associated with the selected range-only observations.

$$\mathbf{P}_0^{-1} + \mathbf{H}^{\mathsf{T}}\mathbf{R}^{-1}\mathbf{H} \preceq \left(\bar{\eta} + \bar{\phi}\right) \mathbf{I}_{K\times K}, \tag{3.8}$$

where $\bar{\eta} + \bar{\phi} = \sum_{j=1}^{K} \frac{1}{\sigma_{s_j}^2} + \lambda_{\max}\left[\mathbf{P}_0^{-1}\right]$.

Remark: The upper bound on FIM is directly a function of the initial uncertainty and the measurement noise. Therefore, this upper bound can vary depending on the magnitude of these quantities and the number of selected range-only observations.

3.4 Simulation Results

This section presents simulation results to analyze the transmitter selection performance, effect of timing on the optimal transmitter selection, and the computational cost of the OGS strategy versus the OSS strategy versus the optimal selection (obtained via an exhaustive search strategy).

3.4.1 Simulation Settings

The simulated environment assumes that the aerial vehicle had a known vertical position, which reduces the aerial vehicle's position state vector to 2–D (planar) rather than 3–D. Furthermore, the aerial vehicle is assumed to have had initial access to GNSS signals, leading

to knowledge of its initial states (position and clock bias), after which the aerial vehicle looses access to GNSS. During the GNSS availability period, the aerial vehicle is tasked to choose the "best" $K < M$ SOPs to use for navigation once GNSS signals are cut off. The simulation settings are summarized in Table 3.1.

Table 3.1: Transmitter Selection Environment Simulation Settings

Parameter	Value
$\boldsymbol{r}_r(0)$	$[0,\ 0]^\mathsf{T}$
$\mathbf{P}_{\boldsymbol{r}_r}(0\|0)$	$1^2 \cdot \mathbf{I}_{2\times 2}$
$\hat{\boldsymbol{r}}_r(0\|0)$	$\sim \mathcal{N}\left[\boldsymbol{r}_r(0),\ \mathbf{P}_{\boldsymbol{r}_r}(0\|0)\right]$
$\{R_i,\ \theta_i\}$	$\{\mathcal{U}[5,\ 80,000]$ m, $\mathcal{U}[-\pi,\ \pi]$ rad $\}$
$\boldsymbol{r}_{s_i}(0)$	$[R_i\cos(\theta_i),\ R_i\sin(\theta_i)]^\mathsf{T}$
$\boldsymbol{x}_{\text{clk},i}(0)$	$[10,\ 1]^\mathsf{T}$
$\{\boldsymbol{x}_{s_i}(0)\}_{i=1}^M$	$\left[\boldsymbol{r}_{s_i}(0)^\mathsf{T},\ \boldsymbol{x}_{\text{clk},i}(0)^\mathsf{T}\right]^\mathsf{T}$
$\{\mathbf{P}_{\text{clk},i}(0\|0)\}_{i=1}^M$	$\text{diag}[30^2,\ 0.3^2]$
$\{\hat{\boldsymbol{x}}_{\text{clk},i}(0\|0)\}_{i=1}^M$	$\sim \mathcal{N}\left[\boldsymbol{x}_{\text{clk},i}(0),\ \mathbf{P}_{x_{\text{clk},i}}(0\|0)\right]$
$\{h_{0,\text{r}},\ h_{-2,\text{r}}\}$	$\{8.0\times 10^{-20},\ 4.0\times 10^{-23}\}$
$\{h_{0,\text{s}_i},\ h_{-2,\text{s}_i}\}_{i=1}^M$	$\{2.6\times 10^{-22},\ 4.0\times 10^{-26}\}$
$\tilde{q}_x, \tilde{q}_y$	0.1 m^2/s^3
$\left\{\sigma_{s_i}^2\right\}_{i=1}^M$	10 m^2
T	0.01 s

Furthermore, three selection strategies were considered. The first strategy performs an exhaustive M choose K selection, i.e., $\binom{M}{K} = \frac{M!}{(M-K)!K!}$, to determine the global optimal transmitter selection (with respect to the specified cost function) for the transmitter selection optimization problem. Note, this strategy is an exhaustive search which makes it extremely computationally expensive. The second strategy is the OGS algorithm which determines the transmitter selection via a recursive selection. The third strategy is the OSS algorithm which determines the transmitter selection via a batch selection. The OGS and OSS strategies

provide a sub-optimal, yet computationally efficient, transmitter selection solution.

3.4.2 Generating the Terrestrial SOP Locations

The cellular SOP network was modeled as a binomial point process (BPP), where the horizontal positions of the M SOPs are independently and uniformly distributed over an annular region centered at the aerial vehicle's current position O, i.e., $\mathbb{B}_O\left(d_{\min}, d_{\max}\right) = \pi(d_{\max}^2 - d_{\min}^2)$ [144], where $d_{\max}$ is the maximum distance for which ranging signals can be detected by the receiver and $d_{\min}$ is the minimum distance required for the far-field assumption to hold (See Fig. 3.5(a) for $M = 30$). The location of the i$^{\text{th}}$ SOP is represented in terms of its range R_i and its aerial vehicle-to-SOP bearing angle θ_i by $(R_i\cos(\theta_i),\ R_i\sin(\theta_i))$, as shown in Fig. 3.5(b).

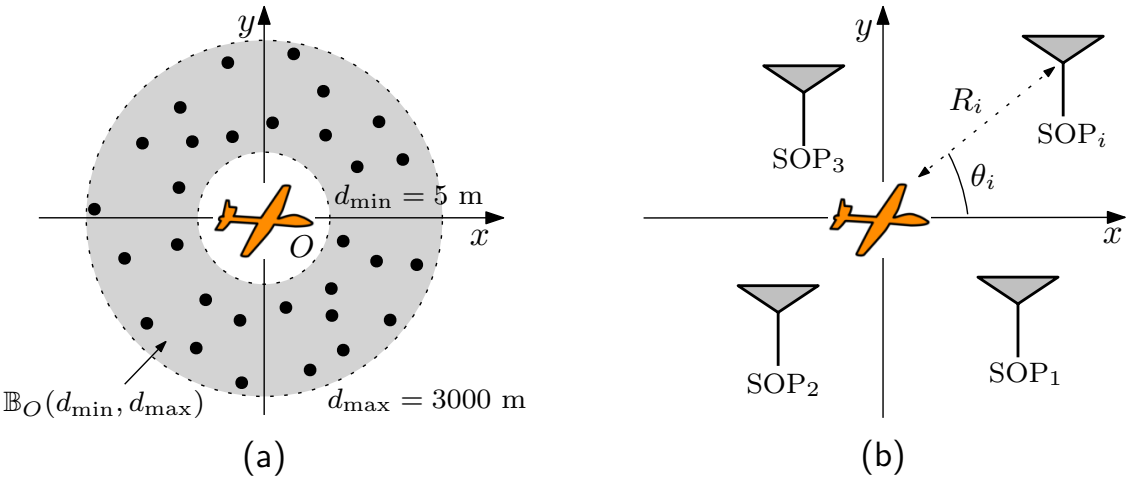

Figure 3.5: (a) BPP realization with $M = 30$ SOPs. (b) Parameterization of the i$^{\text{th}}$ SOP's position.

3.4.3 Optimal Selection, OGS, and OSS Strategy Comparison

The first simulation environment is assumed to be comprised of $M = 30$ terrestrial SOPs where the aerial vehicle is tasked with selecting $K = 15$ SOPs. These results are single

realization, rather than many MC realizations. The solutions resulting from the various selection strategies (M choose K, OGS, and, OSS) are displayed in Fig. 3.6. Note that the selection strategies yielded comparable performance, but the OGS strategy outperforms the OSS strategy slightly. Moreover, the OGS strategy produced a different selection subset than the OSS strategy, as expected since the FIM $\in \mathbb{R}^{2\times 2}$ (2–D case). The A-optimality, E-optimality, and horizontal dilution of precision (HDOP) performance metrics are utilized to quantify the estimation performance of the selected SOPs. The A-optimality measure corresponds to the average variance of the state estimates and the E-optimality measure corresponds to the length of the largest axis of the uncertainty covariance ellipsoid [127]. Table 3.2 presents the performance metrics attained for the two strategies.

The M choose K strategy yielded the best performance metric value for the A-optimality criterion. Moreover, it also yielded the best performance for the E-optimality and the the HDOP criteria. Nevertheless, the OGS strategy was not too far behind and actually was quite close to the optimal cost function evaluation. Specifically, the M choose K global minimum was found to be $\mathcal{J}[\mathbf{I}_{\boldsymbol{r}_r}(\boldsymbol{w}^*)] = 49.6915$ whereas the OGS local minimum was found to be $\mathcal{J}[\mathbf{I}_{\boldsymbol{r}_r}(\boldsymbol{w}_{\text{OGS}})] = 49.7022$ and the OSS local minimum was found to be $\mathcal{J}[\mathbf{I}_{\boldsymbol{r}_r}(\boldsymbol{w}_{\text{OSS}})] = 49.7798$. It is important to note that the optimal M choose K selection came at the price of computational cost (i.e., run-time). The M choose K strategy took 10 hours to run, whereas the OGS strategy took only 7.5 milliseconds to run and the OSS strategy took only 5.4 milliseconds to run.

Table 3.2: Performance Metric Comparison for Selection strategies

	$\text{tr}[\mathbf{I}_{\boldsymbol{r}_r}^{-1}(S)]$	$\lambda_{\max}[\mathbf{I}_{\boldsymbol{r}_r}^{-1}(S)]$	HDOP	Time to Run
M Choose K	49.6915	24.8462	0.516	10.03 hours
OGS	49.7022	24.8606	0.517	7.50 milliseconds
OSS	49.7798	24.9510	0.614	5.40 milliseconds

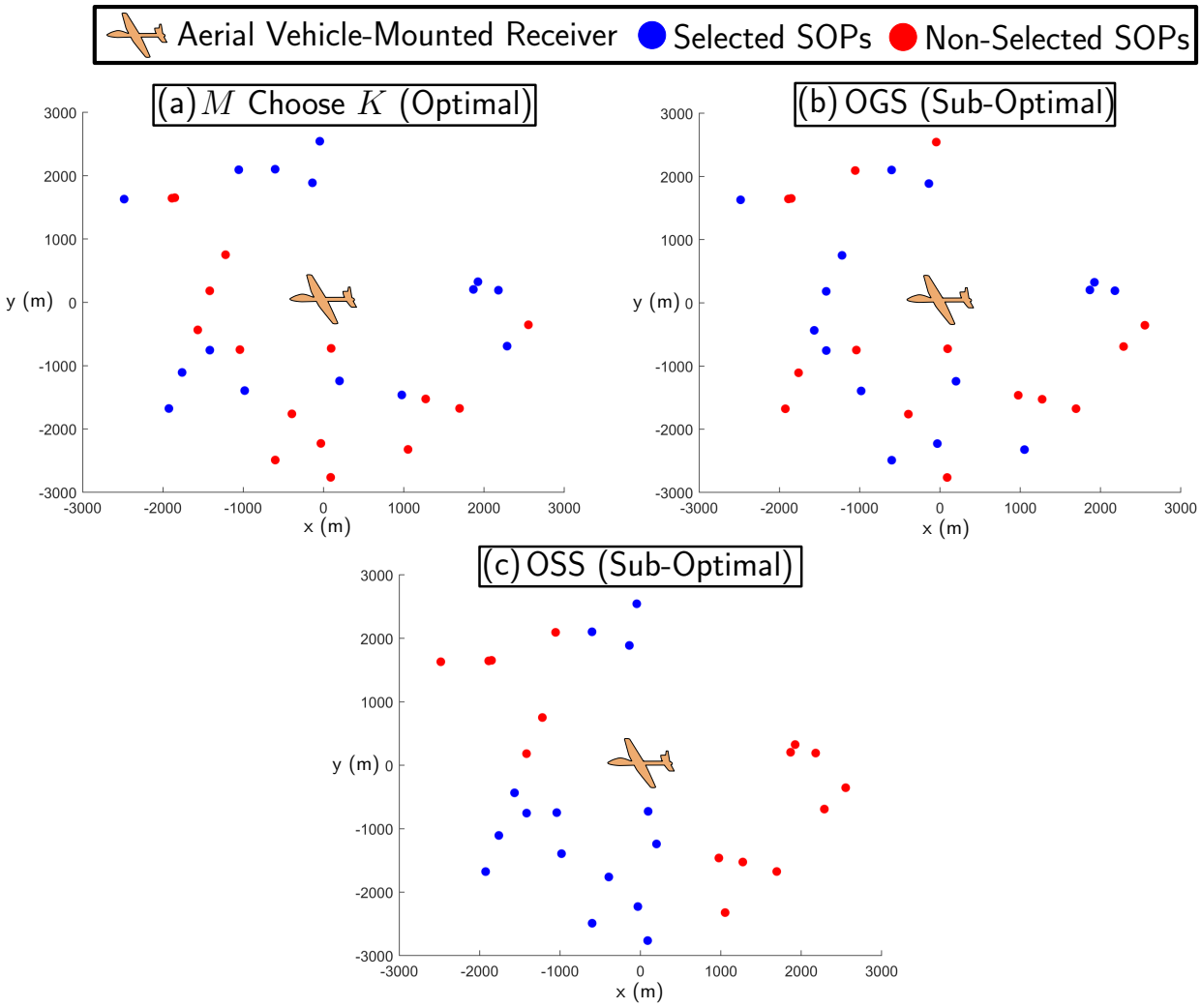

Figure 3.6: Selection strategy comparison. (a) M choose K. (b) Opportunistic greedy selection. (c) One shot selection.

The second simulation environment is assumed to be comprised of $M = 22$ terrestrial SOPs where the aerial vehicle is tasked with selecting K SOPs, as K is varied from 6 to 14. Furthermore, Monte Carlo (MC) simulations are run for each K value to compare the performance of three selection strategies (i.e., optimal selection, OGS, and OSS) with one another. The randomized MC parameters will be the process noise, measurement noise, and transmitter locations for each randomized realization.

Fig. 3.7 displays the performance results for the different transmitter selection strategies

with 10^3 MC simulations for each K value. The large green, blue and red dots represent the cost function values $\mathcal{J}(\boldsymbol{w})$ for the optimal selection, OGS, and OSS schemes, respectively, averaged over all random MC realizations whereas the small green, blue and red dots represent each MC realization. Notice for each K value, the distance between the optimal selection and OGS are very close on average, while the OGS and OSS are far apart (with respect to the distance between the optimal selection and OGS strategy) on average.

Moreover, Table 3.3 and Table 3.4 display the average cost function values $\bar{\mathcal{J}}(\boldsymbol{w})$ over all MC realizations with the corresponding $\pm 1\sigma$ for $K = 6 - 14$. Notice, the average cost function values over all K values for the OGS and optimal selection strategies are very close with a low standard deviation, whereas the OSS strategy is prone to worse selection performance with a higher standard deviation than OGS and the optimal selection.

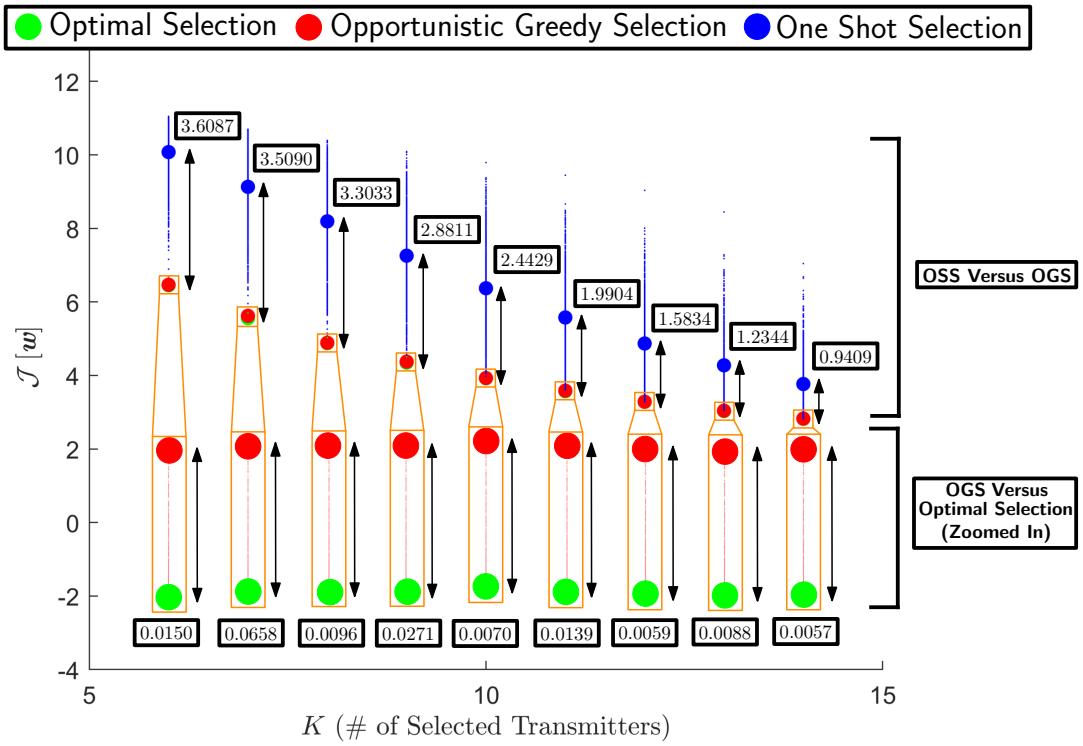

Figure 3.7: Cost function point cloud with 10^3 MC realizations for the optimal selection (green), opportunistic greedy selection (red), and one shot selection (blue) strategies. The averaged cost function value over all MC realizations is represented as a large dot, whereas each selection strategy's cost function value for each MC realization is represented as a small dot.

Table 3.3: Transmitter Selection Strategy's Average Cost Function Values for $K = 6 - 10$

K	6	7	8	9	10
$\bar{\mathcal{J}}(\boldsymbol{w}_*)$ $[\pm\sigma_*]$	6.45 $[\pm 10^{-3}]$	5.56 $[\pm 5 \cdot 10^{-3}]$	4.88 $[\pm 6 \cdot 10^{-3}]$	4.35 $[\pm 9 \cdot 10^{-3}]$	3.92 $[\pm 1 \cdot 10^{-2}]$
$\bar{\mathcal{J}}(\boldsymbol{w}_{\text{OGS}})$ $[\pm\sigma_{\text{OGS}}]$	6.47 $[\pm 2 \cdot 10^{-2}]$	5.62 $[\pm 2 \cdot 10^{-2}]$	4.89 $[\pm 1 \cdot 10^{-2}]$	4.38 $[\pm 1 \cdot 10^{-2}]$	3.93 $[\pm 1 \cdot 10^{-2}]$
$\bar{\mathcal{J}}(\boldsymbol{w}_{\text{OSS}})$ $[\pm\sigma_{\text{OSS}}]$	10.08 [±0.76]	9.13 [±0.99]	8.19 [±1.13]	7.26 [±1.19]	6.37[±1.16]

Table 3.4: Transmitter Selection Strategy's Average Cost Function Values for $K = 11 - 14$

K	11	12	13	14
$\bar{\mathcal{J}}(\boldsymbol{w}_*)$ $[\pm\sigma_*]$	3.57 $[\pm 1 \cdot 10^{-2}]$	3.28 $[\pm 1 \cdot 10^{-2}]$	3.03 $[\pm 2 \cdot 10^{-2}]$	2.82 $[\pm 2 \cdot 10^{-2}]$
$\bar{\mathcal{J}}(\boldsymbol{w}_{\text{OGS}})$ $[\pm\sigma_{\text{OGS}}]$	3.59 $[\pm 2 \cdot 10^{-2}]$	3.29 $[\pm 2 \cdot 10^{-2}]$	3.04 $[\pm 2 \cdot 10^{-2}]$	2.83 $[\pm 3 \cdot 10^{-2}]$
$\bar{\mathcal{J}}(\boldsymbol{w}_{\text{OSS}})$ $[\pm\sigma_{\text{OSS}}]$	5.58 [±1.08]	4.87 [±0.96]	4.28 [±0.84]	3.77 [±0.70]

3.4.4 Effect of Timing on the Optimal Transmitter Selection

This simulation environment is assumed to be comprised of $M = 22$ terrestrial SOPs where the aerial vehicle is tasked with selecting K SOPs, as K is varied from 6 to 14. Furthermore, Monte Carlo (MC) simulations are run for each K value using the optimal transmitter selection strategy. The randomized MC parameters will be the process noise, measurement noise, and transmitter locations for each randomized realization.

Fig. 3.8 highlights the performance of the optimal transmitter selection via the M choose K strategy while considering timing (pseudorange observations) and neglecting timing (range-only observations). Here, 250 MC simulations are performed for $K = 6 - 14$. The performance metric used is the, previously defined, A-optimality criterion corresponding to the uncertainty in the receiver's position error states $\text{tr}\left[\mathbf{P}_{\boldsymbol{r}_r}\right]$, averaged over all MC realizations. Not suprisingly, the optimal transmitter selection's uncertainty is reduced when timing is considered by using pseudorange observations (black) compared to when timing is neglected by using range-only observations (red) for each K value. This is because pseudorange ob-

servations contain more information content than range-only observations via the clock bias state.

It is important to notice, even with improved performance, the difference is almost negligible between the range-only and pseudorange observation. Specifically, the average reduction in position error uncertainty is 0.25 m^2 (variance) across all K values; specifically, for $K = 11$ the reduction in position error uncertainty is 0.22 m^2 (variance). These optimal transmitter selection results justify the need to use range-only observations, rather than the pseudorange observations. Moreover, considering range-only observations decreases computational efforts via a 2×2 matrix inversion, rather than a $n_x \times n_x$ matrix inversion.

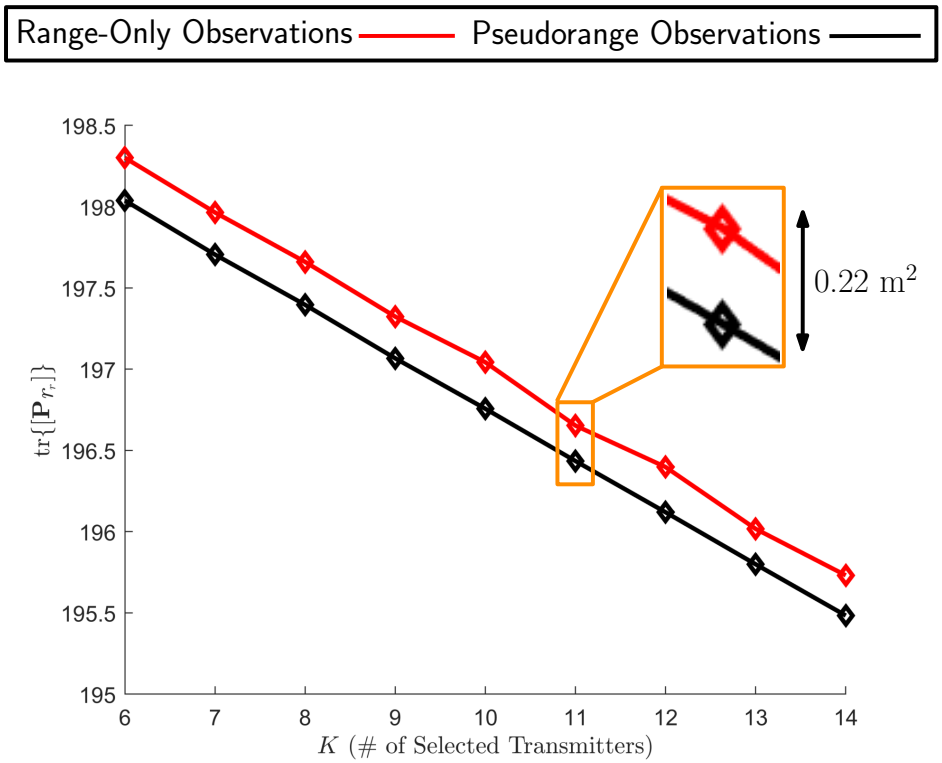

Figure 3.8: Optimal transmitter selection's performance using the A-optimality criterion averaged over 250 MC realizations. Comparison between psuedorange observations, i.e., considering timing, (black) and range-only observations, neglecting timing, (red).

3.4.5 Computational Cost

This simulation environment is assumed to be comprised of M terrestrial SOPs where the aerial vehicle is tasked with selecting K SOPs. The values of both M and K are varied, while a computer with a processor base frequency @ 3.00 GHz and a CPU with 8-cores, 8-threads is used. The computational cost of using the optimal selection (i.e., M choose K strategy) grows exponentially in time (hours) [145], while the computational cost of using the OGS and OSS strategies grows quadratic in time (milliseconds), respectively. Fig. 3.9 compares the time to run for each transmitter selection strategy.

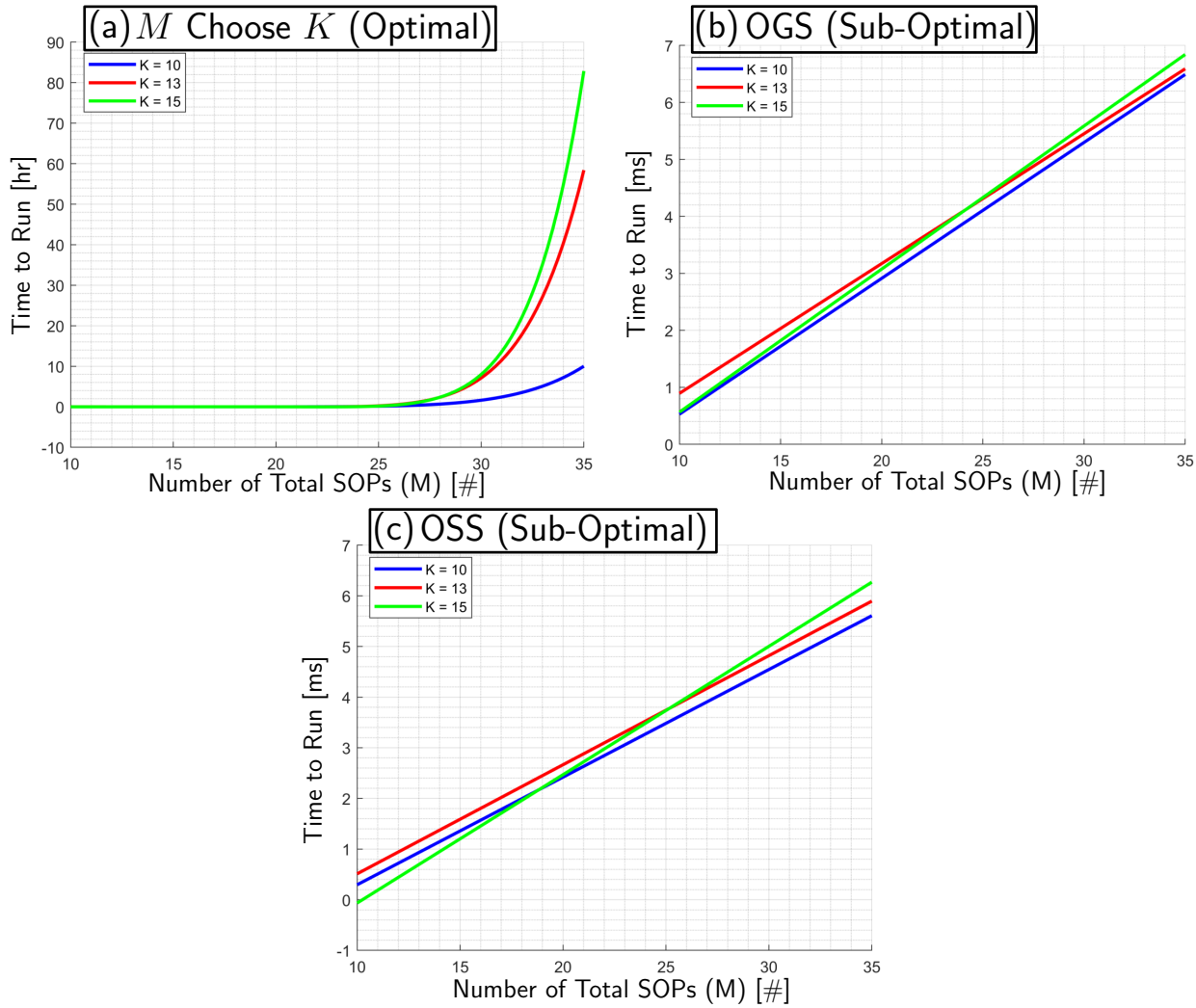

Figure 3.9: Each selection strategy's time to run. (a) M choose K. (b) OGS. (c) OSS.

3.5 Experimental Results

This section demonstrates the efficacy of the proposed OGS and OSS strategies to select a "manageable" subset of terrestrial SOP pseudorange observations to navigate an aircraft in a real-world environment.

3.5.1 Hardware and Software Setup

In March 2020, a joint effort between the Autonomous Systems Perception, Intelligence, and Navigation Laboratory (ASPIN) and Edwards Air Force Base (AFB), California, U.S.A. led to week-long flights in a mission called "SNIFFER: Signals of opportunity for Navigation In Frequency-Forbidden EnviRonments." The flights took place on a Beechcraft C12 Huron, a fixed-wing U.S. Air Force aircraft, flown by members of the USAF Test Pilot School (TPS) over two different regions: (i) a rural region located in Edwards, California, USA, and (ii) a semi-urban region located in Palmdale, California, USA.

The C-12 aircraft was equipped with a quad-channel universal software radio peripheral (USRP)-2955, three consumer-grade 800/1900 MHz Laird cellular antennas, GPS antenna, a solid-state drive for data storage, PCIe cable, and a laptop computer running ASPIN Laboratory's software-defined radio (SDR), called MATRIX: Multichannel Adaptive TRansceiver Information eXtractor, for real-time monitoring of the cellular signals [146, 128, 36]. Furthermore, the equipment necessary for the experiment was assembled at the ASPIN Laboratory on a special rack provided by the U.S. Air Force and was mounted on the C-12 aircraft. The MATRIX SDR produces the navigation observables, i.e., Doppler frequency, carrier phase, and pseudorange, along with the corresponding carrier-to-noise ratio (C/N_0). The experimental hardware setup is shown in Fig. 3.10.

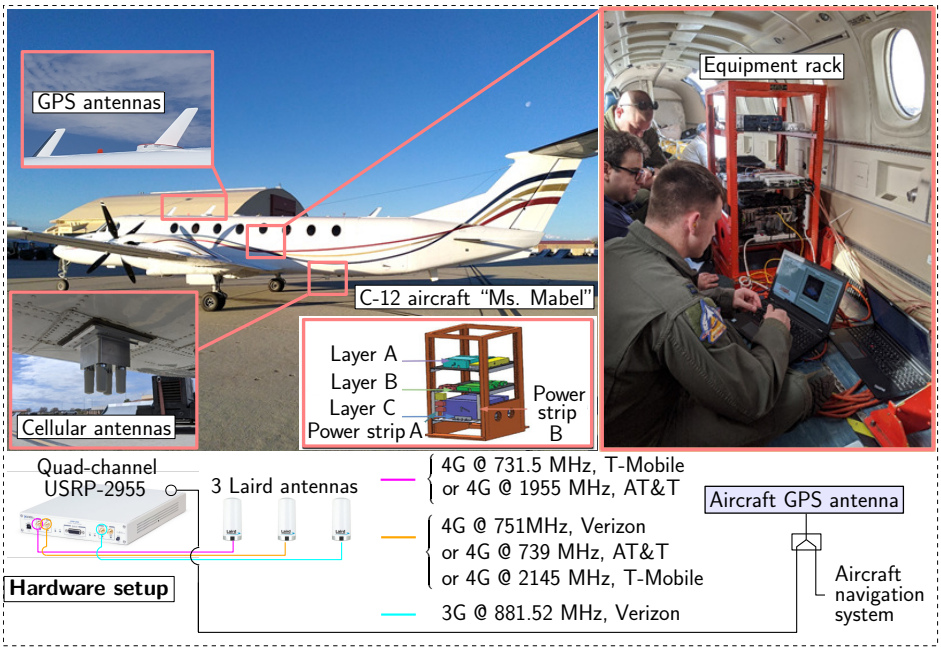

Figure 3.10: Hardware setup equipped to the C-12 aircraft.

The initial state vector was constructed as $\hat{\boldsymbol{x}}(0|0) = [\hat{\boldsymbol{r}}_r(0|0)^\mathsf{T},\ \dot{\hat{\boldsymbol{r}}}_r(0|0)^\mathsf{T},\ c\hat{\delta t}_1(0|0),\ c\dot{\hat{\delta t}}_1(0|0),\ \ldots,\ c\hat{\delta t}_K(0|0), c\dot{\hat{\delta t}}_K(0|0)]^\mathsf{T}$ with a corresponding initial estimation error covariance defined as $\mathbf{P}(0|0) = \text{diag}[10^2 \cdot \mathbf{I}_{3\times 3},\ 10 \cdot \mathbf{I}_{3\times 3},\ 10^8,\ 10, \ldots, 10^8,\ 10]$. It should be noted the modified clock error states of each SOP was initialized using the pseudorange observations from the initial two time epochs. Specifically, the clock bias was initialized as $c\delta t_i(0|0) = z_{s_i}(0) - \|\boldsymbol{r}_r(0) - \boldsymbol{r}_{s_i}\|_2$ and the clock drift was initialized as $c\dot{\delta t}_i(0|0) = \frac{1}{T}[z_{s_i}(1) - z_{s_i}(0) - \|\boldsymbol{r}_r(1) - \boldsymbol{r}_{s_i}\|_2 + \|\boldsymbol{r}_r(0) - \boldsymbol{r}_{s_i}\|_2]$, respectively.

Furthermore, the aircraft's dynamics were assumed to evolve according to the simple, yet effective, velocity random walk model [121], with power spectra given by $\tilde{q}_E = \tilde{q}_N = 5$ m^2/s^3 and $\tilde{q}_U = 10^{-3}$ m^2/s^3 the continuous-time acceleration noise in the East (E), North (N), and Up (U) directions, respectively, with a sampling time $T = 0.01$ s. The receiver's clock covariance $\mathbf{Q}_{\text{clk},r}$ was set to correspond to a worst TCXO with $h_{0,r} = 2.0 \times 10^{-19}$ s and $h_{-2,r} = 2.0 \times 10^{-20}$ s^{-1}. The SOPs' clock covariance $\mathbf{Q}_{\text{clk},s_i}$ was set to correspond to a typical OCXO with $h_{0,s_i} = 8.0 \times 10^{-20}$ s and $h_{-2,s_i} = 4.0 \times 10^{-23}$ s^{-1}, which is typical for

cellular towers [129, 130]. The time-varying measurement covariance $\mathbf{R}$ was assumed to be proportional to the inverse of the carrier-to-noise ratio at each time step.

3.5.2 Flight A: Transmitter Selection in Rural Region $\binom{57}{15}$

The rural region was comprised of $M = 57$ terrestrial cellular SOPs, where the aircraft was tasked with selecting $K = 15$ SOPs with which to navigate after GNSS signals became unavailable. The aircraft's position and velocity state vector was initialized with $[\hat{\boldsymbol{r}}_r(0|0)^\mathsf{T},\ \dot{\hat{\boldsymbol{r}}}_r(0|0)^\mathsf{T}]^\mathsf{T} = [2.51,\ 10.13,\ 1996.22,\ 83.58,\ -17.55,\ -5.37]^\mathsf{T}$.

The OGS and OSS strategies were implemented to choose a selection subset S consisting of $K = 15$ SOPs, after access to GNSS signals was cut off. The selected SOPs from the OGS strategy are denoted by the red pins, the selected SOPs from the OSS strategy are denoted by yellow pins, the selected SOPs from both the OSS and OGS strategies are denoted by orange pins, and the non-selected SOPs are denoted by white pins in Fig. 3.11.

In this scenario, the aircraft navigated along the green trajectory in Fig. 3.11 for 1.48 km utilizing the selected SOPs over a valid selection region. For the OGS strategy, the aircraft's position and velocity root mean square error (RMSE) was found to be 6.28 m and 1.44 m/s, respectively, and executed in approximately 19.3 ms. For the OSS strategy, the aircraft's position and velocity RMSE was found to be 7.13 m and 1.39 m/s, respectively, and executed in approximately 16.5 ms. It should be noted, the optimal solution (i.e., global minimizer) for terrestrial SOP selection is infeasible to compute using the M choose K selection strategy due to its formidable run time. In light of this, 10^5 Monte Carlo (MC) runs were performed in an attempt to capture a range of best-to-worst selections. The randomized parameter for the MC runs was the selection subset S, process noise, and measurement noise.

Fig. 3.12 plots the histogram probability density function (pdf) of the position and velocity

RMSEs over all MC runs. These figures provide insight into the error distribution of the aerial vehicle's navigation solution for the ensemble of randomized realizations. Notice, the OGS strategy's position RMSE value is placed in the left-most histogram bin, whereas the OSS strategy's position RMSE value is slightly worse, implying the OGS's navigation solution is close to the navigation solution obtained when using the best MC realization.

Table 3.5 and Table 3.6 summarizes the navigation performance for the OGS strategy, OSS strategy, and the range of obtained performance metrics (i.e., [minimum, maximum]) with the MC selection.

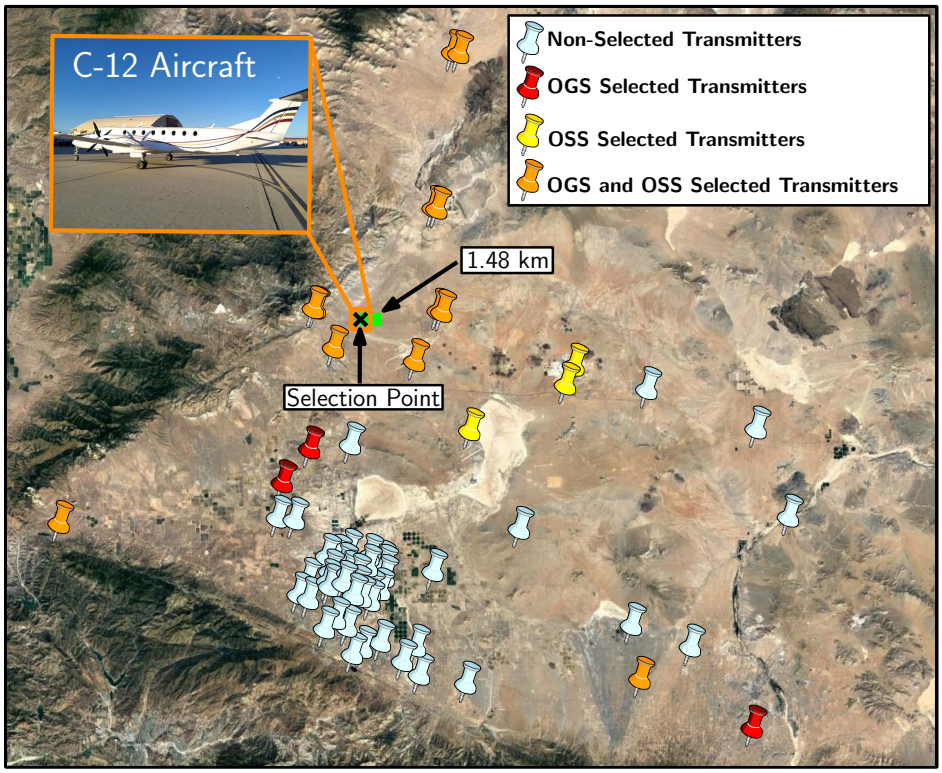

Figure 3.11: Experimental layout and results using the OGS and OSS strategies for transmitter selection during the aircraft's flight. Map data: Google Earth.

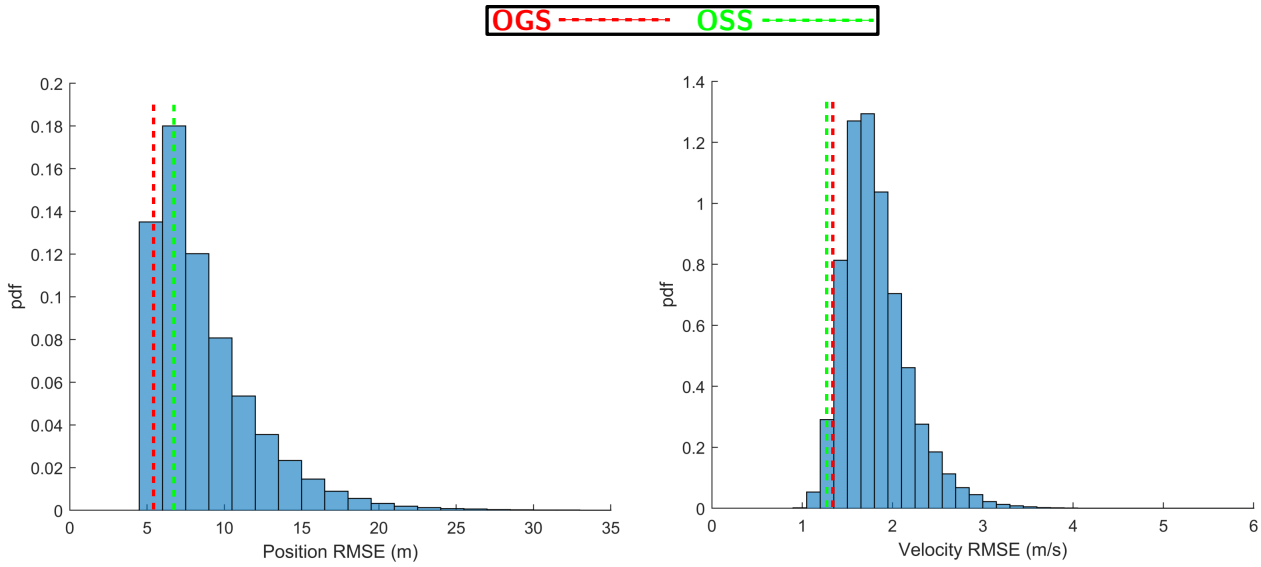

Figure 3.12: Histogram pdf of the position and velocity RMSEs for 10^5 different randomized transmitter selections versus the OGS strategy's RMSEs (red) versus the OSS strategy's RMSEs (green).

Table 3.5: Experiment 1: Navigation Solution Performance

Selection Type	**Pos. RMSE [m]**	**Vel. RMSE [m/s]**
10^5 Monte Carlo Runs	[4.5260, 71.5528]	[0.9751, 7.6061]
Opportunistic Greedy Selection	6.2752	1.4361
One Shot Selection	7.1305	1.3880

Table 3.6: Experiment 1: Navigation Solution Performance

Selection Type	**Max Pos. Error [m]**	**Max Vel. Error [m/s]**	**Run Time [ms]**
10^5 Monte Carlo Runs	[10.5017, 125.0583]	[5.9020, 11.4588]	-
Opportunistic Greedy Selection	10.5030	6.3813	19.3
One Shot Selection	10.5030	6.3821	16.5

3.5.3 Flight B: Transmitter Selection in Semi-Urban Region $\binom{18}{9}$

The semi-urban region was comprised of $M = 18$ terrestrial cellular SOPs, where the aircraft was tasked with selecting $K = 9$ SOPs with which to navigate after GNSS signals

became unavailable. The aircraft's position and velocity state vector was initialized with $[\hat{\boldsymbol{r}}_r(0|0)^\mathsf{T},\ \dot{\hat{\boldsymbol{r}}}_r(0|0)^\mathsf{T}]^\mathsf{T} = [2.51,\ 10.13,\ 536.78,\ 80.17,\ -14.48,\ -5.61]^\mathsf{T}$.

The M choose K (optimal selection), OGS, and OSS strategies were implemented to choose a selection subset S consisting of $K = 9$ SOPs after access to GNSS signals was cut off. It should be noted, the number of SOPs in this environment was small enough to compute the optimal solution via the M choose K selection strategy which perform as an exhaustive search over all possible selection permutations to determine the global minimizer for the transmitter selection optimization problem. Therefore, MC selection is not necessary to be conducted in this region.

The selected SOPs from the OSS strategy are denoted by yellow pins, the selected SOP from the optimal selection are denoted by a green pin, the selected SOPs from both the optimal selection and OGS strategy are denoted by violet pins, the selected SOPs from both the OGS and OSS strategies are denoted by orange pins, the selected SOPs from the optimal selection, OSS, and OGS strategies are denoted by blue pins, and the non-selected SOPs are denoted by white pins in Fig. 3.13.

In this scenario, the aircraft navigated along the green trajectory in Fig. 3.13 for 1.22 km, utilizing the selected SOPs over a valid selection region. For the optimal selection, the aircraft's position and velocity root mean square error (RMSE) was found to be 5.83 m and 1.45 m/s, respectively, and executed in 700.3 ms. For the OGS strategy, the aircraft's position and velocity root mean square error (RMSE) was found to be 6.07 m and 1.42 m/s, respectively, and executed in 5.3 ms. For the OSS strategy, the aircraft's position and velocity RMSE was found to be 6.70 m and 1.35 m/s, respectively, and executed in 3.9 ms. Notice, the OGS strategy is close to that of the optimal selection's navigation solution performance, whereas the OSS strategy performs slightly worse. Further implying, the computationally efficient OGS selection strategy will yield a similar performance to the computationally expensive optimal selection strategy over this valid selection region.

Table 3.7 and Table 3.8 summarizes the navigation performance for the optimal selection via the M choose K strategy, OGS strategy, and OSS strategy.

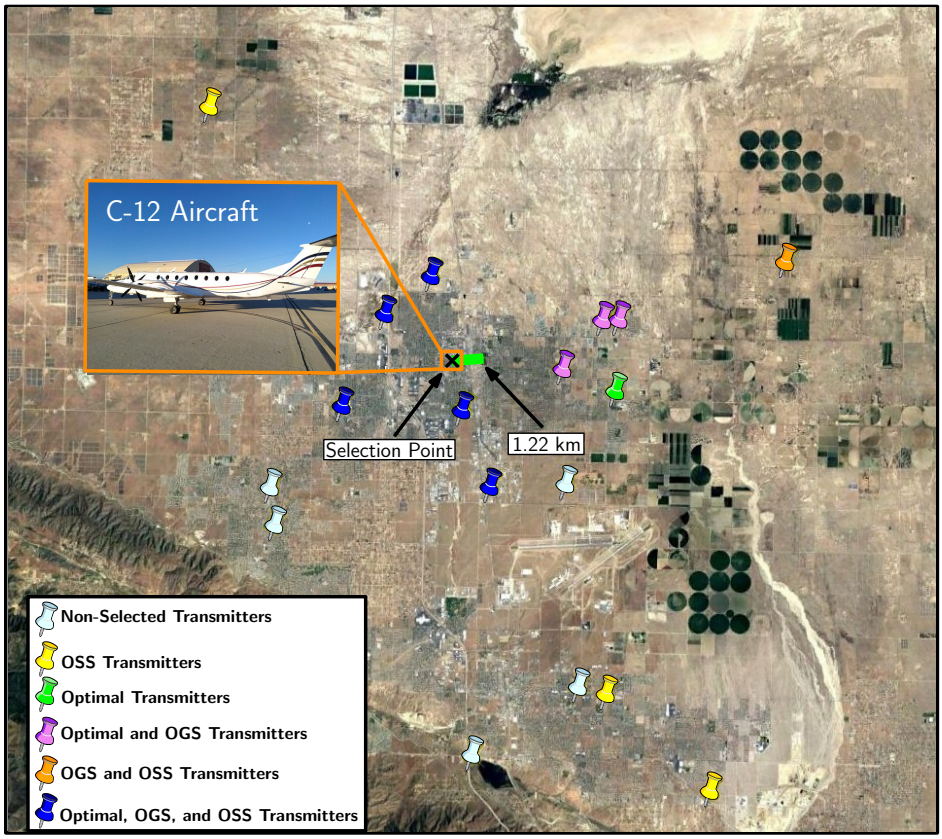

Figure 3.13: Experimental layout and results using the optimal selection, OGS, and OSS strategies for transmitter selection during the aircraft's flight. Map Data: Google Earth.

Table 3.7: Experiment 2: Navigation Solution Performance

Selection Type	**Pos. RMSE [m]**	**Vel. RMSE [m/s]**
Optimal Selection	5.8336	1.4530
Opportunistic Greedy Selection	6.0753	1.4176
One Shot Selection	6.6958	1.3454

Table 3.8: Experiment 2: Navigation Solution Performance

Selection Type	**Max Pos. Error [m]**	**Max Vel. Error [m/s]**	**Run Time [ms]**
Optimal Selection	10.7968	5.9025	700.3
Opportunistic Greedy Selection	10.7968	5.9025	5.3
One Shot Selection	10.7967	5.9025	3.9

Chapter 4

Conclusions

This thesis provided a performance analysis and efficient transmitter selection strategies for aerial vehicle navigation with terrestrial signal of opportunity. A lower bound for the error covariance of the radio SLAM framework is derived and an observability analysis of a UAV with imperfect knowledge of its initial state for two partially known and one unknown SOP towers in the environment (i.e., base case) was assessed and observability was found to be guaranteed for $l \geq 4$ time-steps. In addition, computationally efficient, yet sub-optimal, transmitter selection strategies to choose the most informative subset of terrestrial SOPs to use for navigation was presented. The simulation results demonstrated the lower bound on the error covariance numerically via MC runs, and demonstrated a performance analysis for the optimal selection, OGS, and OSS strategies (transmitter selection performance comparison and computational cost comparison) as well as showed the effect of timing on the optimal selection. The experimental results on the collected data from a UAV and a U.S. Air Force high altitude aircraft navigating without GNSS signals demonstrated the the efficacy of the developed theory and proposed algorithms. It was shown that a UAV navigating via radio SLAM with signals from two partially known cellular SOPs and one unknown cellular SOP can achieve bounded localization errors and bounded estimation error

variance over a bounded region. Furthermore, it was shown that an aircraft navigating with K out of M cellular SOPs in, (i) a rural region and (ii) a semi-urban region, using the OGS performs comparably well with the optimal selection (or best MC realization), whereas the OSS performs slightly worse, over a valid transmitter selection region.

Appendix A

Relationship Between the Weighted HDOP Matrix and Information Content

Dilution of precision (DOP) states how errors in the observation will affect the errors in the final estimates of the unknown quantities. In particular, this analysis will be considering the weighted horizontal dilution of precision (HDOP).

$$\mathbf{D}_{\mathrm{w}} = \begin{bmatrix} \sigma_x^2 & \sigma_{xy}^2 \\ \sigma_{xy}^2 & \sigma_y^2 \end{bmatrix}, \tag{A.1}$$

where $\mathbf{D}_{\mathrm{w}} \triangleq [\mathbf{H}^{\mathsf{T}}\mathbf{R}^{-1}\mathbf{H}]^{-1}$ represents the weighted HDOP matrix [147, 148] with the associated Jacobian matrix for the observation vector $\boldsymbol{z}' \triangleq [z'_{s_1},\ \ldots,\ z'_{s_M}]^{\mathsf{T}}$ defined as,

$$\mathbf{H} = \frac{\boldsymbol{r}_r^{\mathsf{T}} - \boldsymbol{r}_{s_i}^{\mathsf{T}}}{\|\boldsymbol{r}_r - \boldsymbol{r}_{s_i}\|_2}, \tag{A.2}$$

and HDOP $= \sqrt{\sigma_x^2 + \sigma_y^2}$.

Now, the weighted HDOP matrix can be related to information content by the inverse of the estimation error covariance matrix, as follows

$$\begin{aligned}\mathbf{D}_{\mathrm{w}}^{-1} &= \sum_{j=1}^{K} \frac{1}{\sigma_{s_j}^2} \begin{bmatrix} \frac{(x_r - x_{s_j})^2}{(x_r - x_{s_j})^2 + (yr - y_{s_j})^2} & \frac{(x_r - x_{s_j})(y_r - y_{s_j})}{(x_r - x_{s_j})^2 + (yr - y_{s_j})^2} \\ \frac{(x_r - x_{s_j})(y_r - y_{s_j})}{(x_r - x_{s_j})^2 + (yr - y_{s_j})^2} & \frac{(y_r - y_{s_j})^2}{(x_r - x_{s_j})^2 + (yr - y_{s_j})^2} \end{bmatrix} \\ &= \sum_{j=1}^{K} \frac{1}{\sigma_{s_j}^2} \begin{bmatrix} \alpha_j^2 & \alpha_j \beta_j \\ \alpha_j \beta_j & \beta_j^2 \end{bmatrix}\end{aligned}$$

where $\alpha_i = \frac{x_r - x_{s_i}}{\sqrt{(x_r - x_{s_i})^2 + (y_r - y_{s_i})^2}}$ and $\beta_i = \frac{y_r - y_{s_i}}{\sqrt{(x_r - x_{s_i})^2 + (y_r - y_{s_i})^2}}$ are variables which define the position unit vectors (i.e., $[\alpha_i,\ \beta_i]^{\mathsf{T}} = \frac{\boldsymbol{r}_r - \boldsymbol{r}_{s_i}}{\|\boldsymbol{r}_r - \boldsymbol{r}_{s_i}\|_2}$). Furthermore, the weighted HDOP matrix can be related to the information content in a closed form, defined by

$$\mathbf{D}_{\mathrm{w}} = \Lambda \sum_{j=1}^{K} \frac{1}{\sigma_{s_j}^2} \begin{bmatrix} \beta_j^2 & -\alpha_j \beta_j \\ -\alpha_j \beta_j & \alpha_j^2 \end{bmatrix}, \tag{A.3}$$

where

$$\Lambda = \left[\left\{ \sum_{j=1}^{K} \frac{\alpha_j^2}{\sigma_{s_j}^2} \right\} \left\{ \sum_{j=1}^{K} \frac{\beta_j^2}{\sigma_{s_j}^2} \right\} - \left\{ \sum_{j=1}^{K} \frac{\alpha_j \beta_j}{\sigma_{s_j}^2} \right\}^2 \right]^{-1}$$

is a constant value, corresponding to the information content of the position states, which is found in all HDOP terms. Finally, the HDOP constant can be defined as

$$\mathrm{HDOP} = \sqrt{\Lambda \left\{ \sum_{j=1}^{K} \frac{1}{\sigma_{s_j}^2} \left(\beta_j^2 + \alpha_j^2 \right) \right\}}$$

Remark: Typically, for navigation applications, the measurement noise is assumed to be proportional to the inverse of the carrier-to-noise ratio (C/N_0), i.e., $\mathbf{R} = \gamma [C/N_0]^{-1}$ where $\gamma > 0$ [80, 81].

Appendix B

Fisher Information Matrix Structure: Pseudorange and Range-Only Observations

The FIM structure of K selected SOPs is shown for both pseudorange and range-only observations. The FIM structure has an affine form, i.e., the information content is represented as the addition of the prior FIM and a summation of the information content associated with the K selected SOPs (out of M in total SOPs), as follows for

- Range-Only Observations

$$\begin{aligned}\mathbf{I}(\boldsymbol{x}) &= \mathbf{I}_0(\boldsymbol{x}) + \sum_{i=1}^{M} w_i \mathbf{I}_i(\boldsymbol{x}), \\ &= \mathbf{I}_0(\boldsymbol{x}) + \sum_{j=1}^{K} \frac{1}{\sigma_{s_j}^2} \begin{bmatrix} \alpha_j^2 & \alpha_j\beta_j \\ \alpha_j\beta_j & \beta_j^2 \end{bmatrix},\end{aligned} \tag{B.1}$$

- Pseudorange Observations

$$\mathbf{I}(\boldsymbol{x}) = \mathbf{I}_0(\boldsymbol{x}) + \sum_{i=1}^{M} w_i \mathbf{I}_i(\boldsymbol{x}),$$

$$= \mathbf{I}_0(\boldsymbol{x}) + \begin{bmatrix} \sum_{j=1}^{K} \frac{\alpha_j^2}{\sigma_{s_j}^2} & \sum_{j=1}^{K} \frac{\alpha_j \beta_j}{\sigma_{s_j}^2} & \frac{\alpha_1}{\sigma_{s_1}^2} & \frac{\alpha_2}{\sigma_{s_2}^2} & \cdots & \frac{\alpha_K}{\sigma_{s_K}^2} \\ \sum_{j=1}^{K} \frac{\alpha_j \beta_j}{\sigma_{s_j}^2} & \sum_{i=j}^{K} \frac{\beta_j^2}{\sigma_{s_j}^2} & \frac{\beta_1}{\sigma_{s_1}^2} & \frac{\beta_2}{\sigma_{s_2}^2} & \cdots & \frac{\beta_K}{\sigma_{s_K}^2} \\ \frac{\alpha_1}{\sigma_{s_1}^2} & \frac{\beta_1}{\sigma_{s_1}^2} & \frac{1}{\sigma_{s_1}^2} & 0 & 0 & 0 \\ \frac{\alpha_2}{\sigma_{s_2}^2} & \frac{\beta_2}{\sigma_{s_2}^2} & 0 & \frac{1}{\sigma_{s_2}^2} & 0 & 0 \\ \vdots & \vdots & \vdots & \vdots & \ddots & \vdots \\ \frac{\alpha_K}{\sigma_{s_K}^2} & \frac{\beta_K}{\sigma_{s_K}^2} & 0 & 0 & 0 & \frac{1}{\sigma_{s_K}^2} \end{bmatrix}, \tag{B.2}$$

where $\boldsymbol{x}$ is the state vector, w_i is the binary decision variable (determines whether to accept or reject the i-th observation), $j = 1, \ldots, K \in S$ correspond to indices of the transmitters contained in the selection subset, $\mathbf{I}_0(\boldsymbol{x}) \succ \mathbf{0}$ is the prior FIM, $\alpha_j = \frac{x_r - x_{s_j}}{\sqrt{(x_r - x_{s_j})^2 + (y_r - y_{s_j})^2}}$ and $\beta_j = \frac{y_r - y_{s_j}}{\sqrt{(x_r - x_{s_j})^2 + (y_r - y_{s_j})^2}}$ are variables which define the position unit vectors (i.e., $[\alpha_j,\ \beta_j]^{\mathsf{T}} = \frac{\boldsymbol{r}_r - \boldsymbol{r}_{s_j}}{\|\boldsymbol{r}_r - \boldsymbol{r}_{s_j}\|_2}$), and $\sigma_{s_j}^2$ is the measurement noise associated with the j-th observation.

Appendix C

Sandia National Laboratories Funding Statement

Sandia National Laboratories is a multi-mission laboratory managed and operated by National Technology & Engineering Solutions of Sandia, LLC, a wholly owned subsidiary of Honeywell International Inc., for the U.S. Department of Energy's National Nuclear Security Administration under contract DE-NA0003525.

This thesis describes objective technical results and analysis. Any subjective views or opinions that might be expressed in the thesis do not necessarily represent the views of the U.S. Department of Energy or the United States Government.

The Sandia document release number is: SAND2022-7329 T.

Bibliography

[1] R. Sabatini, A. Roy, E. Blasch, K. Kramer, , G. Fasano, I. Majid, O. Crespillo, D. Brown, and R. Ogan. Avionics systems panel research and innovation perspectives. *IEEE Aerospace and Electronic Systems Magazine*, 35(12):58–72, December 2020.

[2] M. Uijt de Haag, E. Dill, S. Young, and M. Joerger. Position, navigation, and timing technologies in the 21st century. volume 2, chapter 60: Commercial Unmanned Aircraft Systems (UAS), pages 1171–1223. Wiley-IEEE, 2021.

[3] R. Ioannides, T. Pany, and G. Gibbons. Known vulnerabilities of global navigation satellite systems, status, and potential mitigation techniques. *Proceedings of the IEEE*, 104(6):1174–1194, February 2016.

[4] EUROCONTROL, Aviation Intelligence Unit. Does radio frequency interference to satellite navigation pose an increasing threat to network efficiency, cost-effectiveness and ultimately safety? Technical report.

[5] International Civil Aviation Organization (ICAO). An urgent need to address harmful interferences to GNSS. Technical report, May 2019.

[6] D. Miralles, A. Bornot, P. Rouquette, N. Levigne, D. Akos, Y.-H.Chen, S. Lo, and T. Walter. An assessment of GPS spoofing detection via radio power and signal quality monitoring for aviation safety operations. *IEEE Intelligent Transportation Systems Magazine*, 12(3):136–146, June 2020.

[7] D. Borio, F. Dovis, H. Kuusniemi, and L. Presti. Impact and detection of GNSS jammers on consumer grade satellite navigation receivers. *Proceedings of the IEEE*, 104(6):1233–1245, February 2016.

[8] A. Soloviev. Tight coupling of GPS, INS, and laser for urban navigation. *IEEE Transactions on Aerospace and Electronic Systems*, 46(4):1731–1746, October 2010.

[9] M. Moussa, A. Moussa, and N. El-Sheimy. Multiple ultrasonic aiding system for car navigation in gnss denied environment. In *Proceedings of IEEE/ION Position, Location and Navigation Symposium*, pages 133–140, 2018.

[10] M. Li and A. Mourikis. High-precision, consistent EKF-based visual-inertial odometry. *International Journal of Robotics Research*, 32(6):690–711, May 2013.

[11] M. Shelley. Monocular visual inertial odometry. Master's thesis, Technical University of Munich, Germany, 2014.

[12] Z. Kassas. Collaborative opportunistic navigation. *IEEE Aerospace and Electronic Systems Magazine*, 28(6):38–41, 2013.

[13] J. Raquet *et al.* Position, navigation, and timing technologies in the 21st century. volume 2, Part D: Position, Navigation, and Timing Using Radio Signals-of-Opportunity, chapter 35–43, pages 1115–1412. Wiley-IEEE, 2021.

[14] N. Souli, P. Kolios, and G. Ellinas. Online relative positioning of autonomous vehicles using signals of opportunity. *IEEE Transactions on Intelligent Vehicles*, pages 1–1, 2021.

[15] Z. Kassas, J. Khalife, A. Abdallah, and C. Lee. I am not afraid of the GPS jammer: resilient navigation via signals of opportunity in GPS-denied environments. *IEEE Aerospace and Electronic Systems Magazine*, 2022. accepted.

[16] J. McEllroy. Navigation using signals of opportunity in the AM transmission band. Master's thesis, Air Force Institute of Technology, Wright-Patterson Air Force Base, Ohio, USA, 2006.

[17] X. Chen, Q. Wei, F. Wang, Z. Jun, S. Wu, and A. Men. Super-resolution time of arrival estimation for a symbiotic FM radio data system. *IEEE Transactions on Broadcasting*, 66(4):847–856, December 2020.

[18] Z. Kassas, J. Khalife, K. Shamaei, and J. Morales. I hear, therefore I know where I am: Compensating for GNSS limitations with cellular signals. *IEEE Signal Processing Magazine*, pages 111–124, September 2017.

[19] J. del Peral-Rosado, R. Raulefs, J. Lopez-Salcedo, and G. Seco-Granados. Survey of cellular mobile radio localization methods: from 1G to 5G. *IEEE Communications Surveys & Tutorials*, 20(2):1124–1148, 2018.

[20] K. Shamaei, J. Khalife, and Z. Kassas. Exploiting LTE signals for navigation: Theory to implementation. *IEEE Transactions on Wireless Communications*, 17(4):2173–2189, April 2018.

[21] P. Gadka, J. Sadowski, and J. Stefanski. Detection of the first component of the received LTE signal in the OTDoA method. *Wireless Communications and Mobile Computing*, pages 1–12, April 2019.

[22] S. Han, T. Kang, and J. Seo. Smartphone application to estimate distances from LTE base stations based on received signal strength measurements. In *International Technical Conference on Circuits/Systems, Computers and Communications*, pages 1–3, June 2019.

[23] T. Kang, H. Lee, and J. Seo. TOA-based ranging method using CRS in LTE signals. *Journal of Advanced Navigation Technology*, 23(5):437–443, October 2019.

[24] T. Kang, H. Lee, and J. Seo. Analysis of the maximum correlation peak value and RSRQ in LTE signals according to frequency bands and sampling frequencies. In *International Conference on Control, Automation and Systems*, pages 1182–1186, October 2019.

[25] K. Avval. Cellular-based localization for mobile devices with structured motion. Master's thesis, University of Toronto, Canada, 2020.

[26] Z. Kassas, J. Khalife, A. Abdallah, and C. Lee. I am not afraid of the jammer: navigating with signals of opportunity in GPS-denied environments. In *Proceedings of ION GNSS Conference*, pages 1566–1585, 2020.

[27] P. Wang and Y. Morton. Multipath estimating delay lock loop for LTE signal TOA estimation in indoor and urban environments. *IEEE Transactions on Wireless Communications*, 19(8):5518–5530, 2020.

[28] H. Dun, C. Tiberius, and G. Janssen. Positioning in a multipath channel using OFDM signals with carrier phase tracking. *IEEE Access*, 8:13011–13028, 2020.

[29] J. Gante, L. Sousa, and G. Falcao. Dethroning GPS: Low-power accurate 5G positioning systems using machine learning. *IEEE Journal on Emerging and Selected Topics in Circuits and Systems*, 10(2):240–252, June 2020.

[30] J. Khalife and Z. Kassas. Opportunistic UAV navigation with carrier phase measurements from asynchronous cellular signals. *IEEE Transactions on Aerospace and Electronic Systems*, 56(4):3285–3301, August 2020.

[31] P. Wang and Y. Morton. Performance comparison of time-of-arrival estimation techniques for LTE signals in realistic multipath propagation channels. *NAVIGATION, Journal of the Institute of Navigation*, 67(4):691–712, December 2020.

[32] K. Shamaei and Z. Kassas. Receiver design and time of arrival estimation for opportunistic localization with 5G signals. *IEEE Transactions on Wireless Communications*, 20(7):4716–4731, 2021.

[33] K. Shamaei and Z. Kassas. A joint TOA and DOA acquisition and tracking approach for positioning with LTE signals. *IEEE Transactions on Signal Processing*, pages 2689–2705, 2021.

[34] A. Abdallah and Z. Kassas. Multipath mitigation via synthetic aperture beamforming for indoor and deep urban navigation. *IEEE Transactions on Vehicular Technology*, 70(9):8838–8853, September 2021.

[35] T. Kazaz, G. Janssen, J. Romme, and A.-J. Van der Veen. Delay estimation for ranging and localization using multiband channel state information. *IEEE Transactions on Wireless Communications*, pages 1–16, September 2021.

[36] A. Abdallah and Z. Kassas. UAV navigation with 5G carrier phase measurements. In *Proceedings of ION GNSS Conference*, pages 3294–3306, September 2021.

[37] L. Chen, P. Thevenon, G. Seco-Granados, O. Julien, and H. Kuusniemi. Analysis on the TOA tracking with DVB-T signals for positioning. *IEEE Transactions on Broadcasting*, 62(4):957–961, December 2016.

[38] C. Yang and A. Soloviev. Mobile positioning with signals of opportunity in urban and urban canyon environments. In *Proceedings of IEEE/ION Position, Location, and Navigation Symposium*, pages 1043–1059, April 2020.

[39] T. Hong, J. Sun, T. Jin, Y. Yi, and J. Qu. Hybrid positioning with DTMB and LTE signals. In *Proceedings of International Wireless Communications and Mobile Computing*, pages 303–307, July 2021.

[40] Z. Kassas, J. Morales, and J. Khalife. New-age satellite-based navigation – STAN: simultaneous tracking and navigation with LEO satellite signals. *Inside GNSS Magazine*, 14(4):56–65, 2019.

[41] R. Landry, A. Nguyen, H. Rasaee, A. Amrhar, X. Fang, and H. Benzerrouk. Iridium Next LEO satellites as an alternative PNT in GNSS denied environments–part 1. *Inside GNSS Magazine*, 14(3):56–64., May 2019.

[42] Q. Wei, X. Chen, and Y. Zhan. Exploring implicit pilots for precise estimation of LEO satellite downlink Doppler frequency. *IEEE Communications Letters*, 24(10):2270–2274, 2020.

[43] S. Thompson, S. Martin, and D. Bevly. Single differenced Doppler positioning with low Earth orbit signals of opportunity and angle of arrival estimation. In *Proceedings of ION International Technical Meeting*, pages 497–509, 2020.

[44] T. Mortlock and Z. Kassas. Performance analysis of simultaneous tracking and navigation with LEO satellites. In *Proceedings of ION GNSS Conference*, pages 2416–2429, September 2020.

[45] F. Farhangian, H. Benzerrouk, and R. Landry. Opportunistic in-flight INS alignment using LEO satellites and a rotatory IMU platform. *Aerospace*, 8(10):280–281, 2021.

[46] Z. Kassas, M. Neinavaie, J. Khalife, N. Khairallah, J. Haidar-Ahmad, S. Kozhaya, and Z. Shadram. Enter LEO on the GNSS stage: Navigation with Starlink satellites. *Inside GNSS Magazine*, 16(6):42–51, 2021.

[47] S. Kozhaya, J. Haidar-Ahmad, A. Abdallah, Z. Kassas, and S. Saab. Comparison of neural network architectures for simultaneous tracking and navigation with LEO satellites. In *Proceedings of ION GNSS Conference*, pages 2507–2520, September 2021.

[48] R. Cassel, D. Scherer, D. Wilburne, J. Hirschauer, and J. Burke. Impact of improved oscillator stability on LEO-based satellite navigation. In *Proceedings of ION International Technical Meeting*, pages 893–905, January 2022.

[49] J. Khalife, M. Neinavaie, and Z. Kassas. The first carrier phase tracking and positioning results with Starlink LEO satellite signals. *IEEE Transactions on Aerospace and Electronic Systems*, 56(2):1487–1491, April 2022.

[50] N. Khairallah and Z. Kassas. An interacting multiple model estimator of LEO satellite clocks for improved positioning. In *Proceedings of IEEE Vehicular Technology Conference*, 2022. accepted.

[51] J. del Peral-Rosado, R. Estatuet-Castillo, J. Lopez-Salcedo, G. Seco-Granados, Z. Chaloupka, L. Ries, and J. Garcoa-Molina. Evaluation of hybrid positioning scenarios for autonomous vehicle applications. In *Proceedings of ION International Technical Meeting Conference*, pages 2541–2553, January 2017.

[52] M. Driusso, C. Marshall, M. Sabathy, F. Knutti, H. Mathis, and F. Babich. Vehicular position tracking using LTE signals. *IEEE Transactions on Vehicular Technology*, 66(4):3376–3391, April 2017.

[53] Z. Kassas, J. Morales, K. Shamaei, and J. Khalife. LTE steers UAV. *GPS World Magazine*, 28(4):18–25, April 2017.

[54] J. Khalife and Z. Kassas. Precise UAV navigation with cellular carrier phase measurements. In *Proceedings of IEEE/ION Position, Location, and Navigation Symposium*, pages 978–989, April 2018.

[55] J. Khalife and Z. Kassas. Navigation with cellular CDMA signals – part II: Performance analysis and experimental results. *IEEE Transactions on Signal Processing*, 66(8):2204–2218, April 2018.

[56] K. Shamaei, J. Khalife, and Z. Kassas. A joint TOA and DOA approach for positioning with LTE signals. In *Proceedings of IEEE/ION Position, Location, and Navigation Symposium*, pages 81–91, April 2018.

[57] K. Shamaei, J. Morales, and Z. Kassas. A framework for navigation with LTE time-correlated pseudorange errors in multipath environments. In *Proceedings of IEEE Vehicular Technology Conference*, pages 1–6, April 2019.

[58] K. Shamaei and Z. Kassas. Sub-meter accurate UAV navigation and cycle slip detection with LTE carrier phase. In *Proceedings of ION GNSS Conference*, pages 2469–2479, September 2019.

[59] J. del Peral-Rosado, O. Renaudin, C. Gentner, R. Raulefs, E. Dominguez-Tijero, A. Fernandez-Cabezas, F. Blazquez-Luengo, G. Cueto-Felgueroso, A. Chassaigne, D. Bartlett, F. Grec, L. Ries, R. Prieto-Cerdeira, J. Lopez-Salcedo, and G. Seco-Granados. Physical-layer abstraction for hybrid GNSS and 5G positioning evaluations. In *Proceedings of IEEE Vehicular Technology Conference*, pages 1–6, September 2019.

[60] Z. Kassas, M. Maaref, J. Morales, J. Khalife, and K. Shamaei. Robust vehicular localization and map matching in urban environments through IMU, GNSS, and cellular signals. *IEEE Intelligent Transportation Systems Magazine*, 12(3):36–52, June 2020.

[61] J. Mortier, G. Pages, and J. Vila-Valls. Robust TOA-based UAS navigation under model mismatch in GNSS-denied harsh environments. *Remote Sensing*, 12(18):2928–2947, September 2020.

[62] M. Maaref and Z. Kassas. Measurement characterization and autonomous outlier detection and exclusion for ground vehicle navigation with cellular signals. *IEEE Transactions on Intelligent Vehicles*, 5(4):670–683, December 2020.

[63] S. Ragothaman, M. Maaref, and Z. Kassas. Autonomous ground vehicle path planning in urban environments using GNSS and cellular signals reliability maps: Models and algorithms. *IEEE Transactions on Aerospace and Electronic Systems*, 57(2):1562–1580, 2021.

[64] S. Ragothaman, M. Maaref, and Z. Kassas. Autonomous ground vehicle path planning in urban environments using GNSS and cellular signals reliability maps: Simulation and experimental results. *IEEE Transactions on Aerospace and Electronic Systems*, 57(4):2575–2586, 2021.

[65] G. Afifi and Y. Gadallah. Autonomous 3-D UAV localization using cellular networks: Deep supervised learning versus reinforcement learning approaches. *IEEE Access*, 9:155234–155248, 2021.

[66] Z. Kassas, A. Abdallah, and M. Orabi. Carpe signum: seize the signal – opportunistic navigation with 5G. *Inside GNSS Magazine*, 16(1):52–57, 2021.

[67] Z. Kassas. *Analysis and Synthesis of Collaborative Opportunistic Navigation Systems*. PhD thesis, The University of Texas at Austin, USA, 2014.

[68] C. Cadena, L. Carlone, H. Carrillo, Y. Latif, D. Scaramuzza, J. Neira, I. Reid, and J. Leonard. Past, present, and future of simultaneous localization and mapping: Toward the robust-perception age. *IEEE Transactions on robotics*, 32(6):1309–1332, 2016.

[69] C. Yang and A. Soloviev. Simultaneous localization and mapping of emitting radio sources-SLAMERS. In *Proceedings of ION GNSS Conference*, pages 2343–2354, September 2015.

[70] J. Morales and Z. Kassas. Tightly-coupled inertial navigation system with signals of opportunity aiding. *IEEE Transactions on Aerospace and Electronic Systems*, 57(3):1930–1948, 2021.

[71] J. Morales and Z. Kassas. Optimal collaborative mapping of terrestrial transmitters: receiver placement and performance characterization. *IEEE Transactions on Aerospace and Electronic Systems*, 54(2):992–1007, April 2018.

[72] F. Ono, K. Takizawa, H. Tsuji, and R. Miura. S-band radio propagation characteristics in urban environment for unmanned aircraft systems. In *Proceedings of International Symposium on Antennas and Propagation*, pages 1–4, 2015.

[73] N. Schneckenburger, T. Jost, D. Shutin, M. Walter, T. Thiasiriphet, M. Schnell, and U.-C. Fiebig. Measurement of the L-band air-to-ground channel for positioning applications. *IEEE Transactions on Aerospace and Electronic Systems*, 52(5):2281–2297, October 2016.

[74] E. Teng, J. Diogo Falcao, and B. Iannucci. Holes-in-the-sky: A field study on cellular-connected UAS. In *Proceedings of International Conference on Unmanned Aircraft Systems*, pages 1165–1174, June 2017.

[75] W. Khawaja, I. Guvenc, D. Matolak, U. Fiebig, and N. Schneckenburger. A survey of air-to-ground propagation channel modeling for unmanned aerial vehicles. *IEEE Communications Surveys & Tutorials*, 21(3):2361–2391, 2019.

[76] E. Kim and Y. Shin. Feasibility analysis of LTE-based UAS navigation in deep urban areas and DSRC augmentation. *Sensors*, 19(9):4192–4207, April 2019.

[77] M. Nekrasov, V. Adarsh, U. Paul, E. Showalter, E. Zegura, M. Vigil-Hayes, and E. Belding. Evaluating LTE coverage and quality from an unmanned aircraft system. In *Proceedings of IEEE International Conference on Mobile Ad Hoc and Sensor Systems*, pages 171–179, 2019.

[78] Y. Zeng, Q. Wu, and R. Zhang. Accessing from the sky: A tutorial on UAV communications for 5G and beyond. *Proceedings of the IEEE*, 107(12):2327–2375, December 2019.

[79] B. Stevens and M. Younis. Detection algorithm for cellular synchronization signals in airborne applications. *IEEE Access*, 9:55555–55566, April 2021.

[80] Z. Kassas, J. Khalife, A. Abdallah, C. Lee, J. Jurado, S. Wachtel, J. Duede, Z. Hoeffner, T. Hulsey, R. Quirarte, and R. Tay. Assessment of cellular signals of opportunity for high altitude aircraft navigation. *IEEE Aerospace and Electronic Systems Magazine*, 2021. submitted.

[81] Z. Kassas, A. Abdallah, J. Khalife, C. Lee, J. Jurado, J. Duede, Z. Hoeffner, T. Hulsey, R. Quirarte, S. Wachtel, and R. Tay. Received power characterization of terrestrial cellular signals on high altitude aircraft. In *Proceedings of IEEE Aerospace Conference*, March 2022. accepted.

[82] Z. Kassas and T. Humphreys. Observability analysis of collaborative opportunistic navigation with pseudorange measurements. *IEEE Transactions on Intelligent Transportation Systems*, 15(1):260–273, February 2014.

[83] Z. Kassas and T. Humphreys. Receding horizon trajectory optimization in opportunistic navigation environments. *IEEE Transactions on Aerospace and Electronic Systems*, 51(2):866–877, April 2015.

[84] J. Morales and Z. Kassas. Stochastic observability and uncertainty characterization in simultaneous receiver and transmitter localization. *IEEE Transactions on Aerospace and Electronic Systems*, 55(2):1021–1031, April 2019.

[85] E. Leitinger, F. Meyer, F. Hlawatsch, K. Witrisal, F. Tufvesson, and M. Win. A scalable belief propagation algorithm for radio signal based SLAM. *IEEE Transactions on Wireless Communications*, 18(12):5613–5629, September 2019.

[86] Z. Kassas, A. Arapostathis, and T. Humphreys. Greedy motion planning for simultaneous signal landscape mapping and receiver localization. *IEEE Journal of Selected Topics in Signal Processing*, 9(2):247–258, March 2015.

[87] Y. Yang, J. Morales J. Khalife and, and Z. Kassas. UAV waypoint opportunistic navigation in GNSS-denied environments. *IEEE Transactions on Aerospace and Electronic Systems*, page accepted, 2021.

[88] Z. Kassas and T. Humphreys. The price of anarchy in active signal landscape map building. In *Proceedings of IEEE Global Conference on Signal and Information Processing*, pages 165–168, December 2013.

[89] J. Morales and Z. Kassas. Information fusion strategies for collaborative radio SLAM. In *Proceedings of IEEE/ION Position Location and Navigation Symposium*, pages 1445–1454, April 2018.

[90] J. Morales and Z. Kassas. Event-based communication strategy for collaborative navigation with signals of opportunity. In *Proceedings of Asilomar Conference on Signals, Systems and Computers*, pages 548–553, November 2018.

[91] J. Morales, J. Khalife, and Z. Kassas. Information fusion strategies for collaborative inertial radio SLAM. *IEEE Transactions on Intelligent Transportation Systems*, 2021. accepted.

[92] J. Deyst and C. Price. Conditions for asymptotic stability of the discrete minimum-variance linear estimator. *IEEE Transactions on Automatic Control*, 13(6):702–705, December 1968.

[93] G. Dissanayake, P. Newman, S. Clark, H. Durrant-Whyte, and M. Csorba. A solution to the simultaneous localization and map building (SLAM) problem. *IEEE Transactions on Robotics and Automation*, 17(3):229–241, June 2001.

[94] J. Fenwick, P. Newman, and J. Leonard. Cooperative concurrent mapping and localization. In *Proceedings of IEEE International Conference on Robotics and Automation*, pages 1810–1817, May 2002.

[95] A. Mourikis. and S. Roumeliotis. Analysis of positioning uncertainty in simultaneous localization and mapping (SLAM). In *Proceedings of IEEE/RSJ International Conference on Intelligent Robots and Systems*, volume 1, pages 13–20, 2004.

[96] Z. Jiang, S. Zhang, and L. Xie. Cramer-Rao lower bound analysis for mobile robot navigation. In *Proceedings of International Conference on Intelligent Sensors, Sensor Networks and Information Processing*, pages 229–234, 2005.

[97] S. Huang and G. Dissanayake. Convergence and consistency analysis for extended Kalman filter based SLAM. *IEEE Transactions on Robotics*, 23(5):1036–1049, October 2007.

[98] T. Karvonen, S. Bonnabel, E. Moulines, and S. Särkkä. Bounds on the covariance matrix of a class of Kalman-Bucy filters for systems with non-linear dynamics. In *Proceedings of IEEE Conference on Decision and Control*, pages 7176–718, 2018.

[99] S. Monica and G. Ferrari. UWB-based localization in large indoor scenarios: optimized placement of anchor nodes. *IEEE Transactions on Aerospace and Electronic Systems*, 51(2):987–999, April 2015.

[100] N. Cao, S. Choi, E. Masazade, and P. Varshney. Sensor selection for target tracking in wireless sensor networks with uncertainty. *IEEE Transactions on Signal Processing*, 64(20):5191–5204, 2016.

[101] A. Collin, A. Siddiqi, Y. Imanishi, Y. Matta, T. Tanimichi, and O. Weck. A multiobjective systems architecture model for sensor selection in autonomous vehicle navigation. In *Proceedings of International Conference on Complex Systems Design & Management*, pages 141–152, 2019.

[102] S. Joshi and S. Boyd. Sensor selection via convex optimization. *IEEE Transactions on Signal Processing*, 57(2):451–462, February 2009.

[103] V. Kekatos and G. Giannakis. Selecting reliable sensors via convex optimization. In *Proceedings of IEEE International Workshop on Signal Processing Advances in Wireless Communications*, pages 1–5, June 2010.

[104] S. Liu, S. Chepuri, M. Fardad, E. Masazade, G. Leus, and P. Varshney. Sensor selection for estimation with correlated measurement noise. *IEEE Transactions on Signal Processing*, 64(13):3509–3522, July 2016.

[105] V. Cerone, S. Fosson, and D. Regruto. A non-convex adaptive regularization approach to binary optimization. In *Proceedings of IEEE Conference on Decision and Control*, pages 3844–3849, February 2021.

[106] A. Hashemi, M. Ghasemi, H. Vikalo, and U. Topcu. A randomized greedy algorithm for near-optimal sensor scheduling in large-scale sensor networks. In *Proceedings of American Control Conference*, pages 1027–1032, 2018.

[107] C. Zhan, Y. Zeng, and R. Zhang. Trajectory design for distributed estimation in UAV-enabled wireless sensor network. *IEEE Transactions on Vehicular Technology*, 67(10):10155–10159, 2018.

[108] Z. Dai G. Wang X. Jin and X. Lou. Nearly optimal sensor selection for TDOA-based source localization in wireless sensor networks. *IEEE Transactions on Vehicular Technology*, 69(10):12031–12042, July 2020.

[109] E. Clark, T. Askham, S. Brunton, and N. Kutz. Greedy sensor placement with cost constraints. *IEEE Sensors Journal*, 19(7):2642–2656, 2019.

[110] Y. Saito, T. Nonomura, K. Yamada, K. Nakai, T. Nagata, K. Asai, Y. Sasaki, and D. Tsubakino. Determinant-based fast greedy sensor selection algorithm. *IEEE Access*, 9:68535–68551, 2021.

[111] A. Hashemi, M. Ghasemi, H. Vikalo, and U. Topcu. Randomized greedy sensor selection: Leveraging weak submodularity. *IEEE Transactions on Automatic Control*, 66(1):199–212, January 2021.

[112] L. Zuo, R. Niu, and P. Varshney. A sensor selection approach for target tracking in sensor networks with quantized measurements. In *Proceedings of IEEE International Conference on Acoustics, Speech, and Signal Processing*, pages 2521–2524, April 2008.

[113] X. Shen and P. Varshney. Sensor selection based on generalized information gain for target tracking in large sensor networks. *IEEE Transactions on Signal Processing*, 62(2):363–375, January 2014.

[114] F. Wang, X. Bai, B. Guo, and C. Liu. Dynamic clustering in wireless sensor network for target tracking based on the fisher information of modified kalman filter. In *Proceedings of IEEE International Conference of Systems and Informatics*, pages 696–700, November 2016.

[115] L. Wang, Q. He, and H. Li. Transmitter selection and receiver placement for target parameter estimation in cooperative radar-communications system. *IET Signal Processing*, 2022.

[116] M. Zhang and J. Zhang. A fast satellite selection algorithm: Beyond four satellites. *IEEE Journal of Selected Topics in Signal Processing*, 3(5):740–747, October 2009.

[117] N. Blanco-Delgado and F. Nunes. Satellite selection method for multi-constellation GNSS using convex geometry. *IEEE Transactions on Vehicular Technology*, 59(9):4289–4297, November 2010.

[118] T. Soininen, P. Syrjärinne, S. Ali-Löytty, and C. Schmid. Data-driven approach to satellite selection in multi-constellation GNSS receivers. In *Proceedings of International Conference on Localization and GNSS*, pages 1–6, 2018.

[119] P. Huang, C. Rizos, and C. Roberts. Satellite selection with an end-to-end deep learning network. *GPS Solutions*, 22(4):1–12, 2018.

[120] N. Xia, Q. Zhi, M. He, Y. Hong, and H. Du. A navigation satellite selection algorithm for optimized positioning based on gibbs sampler. *International Journal of Distributed Sensor Networks*, 16(6):15501477–20929620, 2022.

[121] X. Li and V. Jilkov. Survey of maneuvering target tracking. Part I: Dynamic models. *IEEE Transactions on Aerospace and Electronic Systems*, 39(4):1333–1364, 2003.

[122] A. Thompson, J. Moran, and G. Swenson. *Interferometry and Synthesis in Radio Astronomy*. John Wiley & Sons, second edition, 2001.

[123] W.J. Rugh. *Linear System Theory*. Prentice Hall, Upper Saddle River, NJ, second edition, 1996.

[124] R. Hermann and A. Krener. Nonlinear controllability and observability. *IEEE Transactions on Automatic Control*, 22(5):728–740, October 1977.

[125] K. Reif, S. Gunther, E. Yaz, and R. Unbehauen. Stochastic stability of the discrete-time extended Kalman filter. *IEEE Transactions on Automatic Control*, 44(4):714–728, April 1999.

[126] V. Solo. Stability of the Kalman filter with stochastic time-varying parameters. In *Proceedings of IEEE Conference on Decision and Control*, volume 1, pages 57–61, December 1996.

[127] D. Uciński. *Optimal Measurement Methods for Distributed Parameter System Identification*. CRC Press, 2005.

[128] K. Shamaei and Z. Kassas. LTE receiver design and multipath analysis for navigation in urban environments. *NAVIGATION, Journal of the Institute of Navigation*, 65(4):655–675, December 2018.

[129] K. Pesyna, Z. Kassas, J. Bhatti, and T. Humphreys. Tightly-coupled opportunistic navigation for deep urban and indoor positioning. In *Proceedings of ION GNSS Conference*, pages 3605–3617, September 2011.

[130] Z. Kassas, V. Ghadiok, and T. Humphreys. Adaptive estimation of signals of opportunity. In *Proceedings of ION GNSS Conference*, pages 1679–1689, September 2014.

[131] J. Morales, J. Khalife, and Z. Kassas. GNSS vertical dilution of precision reduction using terrestrial signals of opportunity. In *Proceedings of ION International Technical Meeting Conference*, pages 664–669, January 2016.

[132] J. Morales, J. Khalife, and Z. Kassas. Opportunity for accuracy. *GPS World Magazine*, 27(3):22–29, March 2016.

[133] M. Maaref, J. Khalife, and Z. Kassas. Aerial vehicle protection level reduction by fusing GNSS and terrestrial signals of opportunity. *IEEE Transactions on Intelligent Transportation Systems*, 22(9):5976–5993, September 2021.

[134] S. Kay. *Fundamentals of Statistical Signal Processing: Estimation Theory*, volume I. Prentice-Hall, Upper Saddle River, NJ, 1993.

[135] S. Chepuri and G. Leus. Sparsity-promoting sensor selection for non-linear measurement models. *IEEE Transactions on Signal Processing*, 63(3):684–698, February 2015.

[136] L. Perera and E. Nettleton. On the nonlinear observability and the information form of the SLAM problem. In *Proceedings of IEEE Internartional Conference on Intelligent Robots and Systems*, volume 1, pages 2061–2068, October 2009.

[137] L. Perera and E. Nettleton. On stochastically observable directions of the estimation theoretic SLAM state space. In *Proceedings of IEEE/RSJ International Conference on Intelligent Robots and Systems*, pages 4324–4331, October 2010.

[138] G.O. Mutambara. *Decentralized Estimation and Control for Multisensor Systems*. CRC Press, 1998.

[139] N. Blanco-Delgado, F. Nunes, and G. Seco-Granados. Relation between GDOP and the geometry of the satellite constellation. In *International Conference on Localization and GNSS*, pages 175–180, June 2011.

[140] Y. Shen and M. Win. Fundamental limits of wideband localization–Part I: A general framework. *IEEE Transactions on Information Theory*, 56(10):4956–4980, October 2010.

[141] Y. Wang, Y. Wu, and Y. Shen. Performance limits of cooperative localization using signals of opporunity in aray networks. In *Proceedings of IEEE International Conference on Communications*, pages 1–6, May 2019.

[142] A. Nguyen and Z. Kassas. Transmitter selection for improved information gathering in aerial vehicle navigation with terrestrial signals of opportunity. In *Proceedings of ION International Technical Meeting*, pages 723–734, January 2022.

[143] A. Nguyen, Z. Shadram, and Z. Kassas. A lower bound for the error covariance of radio SLAM with terrestrial signals of opportunity. In *Proceedings of ION GNSS Conference*, pages 2294–2306, September 2021.

[144] S. Aditya, H. Dhillon, A. Molisch, R. Buehrer, and H. Behairy. Characterizing the impact of SNR heterogeneity on time-of-arrival-based localization outage probability. *IEEE Transactions on Wireless Communications*, 18(1):637–649, January 2019.

[145] S. Joshi and S. Boyd. Sensor selection via convex optimization. *IEEE Transactions on Signal Processing*, 57(2):451–462, October 2009.

[146] J. Khalife, K. Shamaei, and Z. Kassas. Navigation with cellular CDMA signals – part I: Signal modeling and software-defined receiver design. *IEEE Transactions on Signal Processing*, 66(8):2191–2203, April 2018.

[147] J. Li and M. Wu. The improvement of positioning accuracy with weighted least square based on SNR. In *Proceedings of IEEE International Conference on Wireless Communications, Networking and Mobile Computing*, pages 1–4, September 2009.

[148] D. Won, J. Ahn, S. Lee, J. Lee, S. Sung, H. Park, J. Park, and Y. Lee. Weighted DOP with consideration on elevation-dependent range errors of GNSS satellites. *IEEE Transactions on Instrumentation and Measurement*, 61(12):3241–3250, December 2012.